UNIVERSITY OF CALIFORNIA, SAN DIEGO

Implications of Three-Dimensional Urban Heating on Fluid Flow and Dispersion

A Dissertation submitted in partial satisfaction of the
requirements for the degree
Doctor of Philosophy

in

Engineering Sciences (Mechanical Engineering)

by

Negin Nazarian

Committee in charge:

Professor Jan P. Kleissl, Chair
Professor Daniel Tartakovsky, Co-Chair
Professor Joel Norris
Professor Kyaw Tha Paw U
Professor Sutanu Sarkar

2015

The Dissertation of Negin Nazarian is approved, and it is acceptable in quality and form for publication on microfilm and electronically:

_____

_____

_____

_____
Co-Chair

_____
Chair

University of California, San Diego

2015

TABLE OF CONTENTS

LIST OF FIGURES

LIST OF TABLES

ACKNOWLEDGEMENTS

First and foremost, I would like to acknowledge Professor Jan Kleissl for his support throughout this long process as my adviser and chair of my committee. Thank you for having taught me how to work independently and self-sufficiently, while at the same time patiently walking me through the challenges of scientific research whenever I needed guidance. Additionally, thank you for your patience with my non-native English. My academic writing skills have improved significantly because of your corrections and comments on my multiple drafts.

I am also deeply grateful to Dr. Alberto Martilli from the Center for Energy and Environment (CIEMAT) in Spain, who has always been generous with his time and energy. Thank you for your encouragement, mentorship and patience, and thank you for believing in me and my ideas. My outlook on science, and more importantly life, has changed significantly because of our collaboration, and I consider myself fortunate to have known and worked with you during the last two years.

I would also like to acknowledge and thank Professors Daniel Tartakovsky, the co-chair of my dissertation committee, who treated me like one of his own students and helped me in the most critical time of my graduate studies: defense preparation. I deeply appreciate his kindness and support, and learned a lot from his positive attitude towards any obstacle.

I would like to thank the rest of my thesis committee: Professor Sutanu Sarkar for his challenging questions which incented me to widen my research from various perspectives, Professor Kyaw Tha Paw U who completely breaks the stereotype of the uninterested outside committee member, and Professor Joel Noris for his insightful comments. Their suggestions and comments both within and outside the scope of my

research were invaluable.

Friendship to me is the most mysterious and beautiful of all human phenomena, and I am utterly fortunate to have discovered it many times in the past four years. I infinitely thank everyone I met at UCSD, but there are individuals, of course, who I want to name directly. Masoud, ever since I dragged you to apply for UCSD, you have been my constant company (and follower!), and I could not imagine doing this process without you. Tu vas me manquer trop. Negin (the other one), thank you for your soft, strong shoulders. Negins Rock! Alireza and Payam, you should be in the Guinness Book of Records, for pure kindness. And as you all know, *Zendegi Garmie Delhaye beham peyvastast.*

And then there were my big brother and sister. Steve-ster (these days, Professor Meyers)! Life felt much more clear after our hours-long conversations (and now I have some sophisticated vocabulary added to all the number crunching!). Milda, you showed up to my door one night, and you have been an unforgettable friend, and a role model, ever since. I look forward to more international adventures with both of you.

I would also like to thank and acknowledge all my friends that have kept me sane (or at least kept me company in my insanity) throughout this long process: Diletta, thank you for all the days and nights that I spent in your company (mostly in that safe corner on the floor), eating your food that is made with love, and using your wisdom for my existential crisis; my little brother, Handa, our coffee/counseling times were absolutely crucial in keeping me sound; Mohamed, you were the sounding board for my initial ideas; Viktoria, thank you for being the constant jovial and caring companion; Bella Margherita, you were the most amazing company during the long

thesis-writing nights (and also during all the cooking adventures); and Mein Lieber Benedikt, thank you for all those panicking nights when I adamantly insisted that "I am perfectly calm".

Last but not least, I would like to thank my family, without whom I would not be standing where I am today, and to whom this dissertation is dedicated to. Baman, vous etiez la principale source constante de l'amour, le soutien et la force de toutes ces annes. Noushin, abji, thank you for the life-long love and encouragement, and Navid, for your constant support and wisdom. I would like to express my heart-felt gratitude to you all.

The text and data in chapter 3, in full, is a reprint of the material as it appears in "CFD simulation of an idealized urban environment: Thermal effects of geometrical characteristics and surface materials", Nazarian, Negin; Kleissl, Jan, *Urban Climate*, 12 (2015), 141-159. The dissertation author is the primary investigator and author of this article.

The text and data in chapter 4, in full, is a reprint of the material as it appears in "Realistic solar heating in urban areas: Air exchange and street-canyon ventilation", Nazarian, Negin; Kleissl, Jan, *Building and Environment*, 95 (2016), 75-93. The dissertation author is the primary investigator and author of this article.

Chapter 5, in part is currently being prepared for submission for publication of the material. Nazarian, Negin; Martilli, Alberto; Kleissl, Jan. The dissertation author was the primary investigator and author of this material.

VITA

2011	Bachelor of Science in Mechanical Engineering, University of Tehran, Tehran, Iran
2012	Master of Science in Mechanical Engineering, University of California, San Diego, California, San Diego
2015	Doctor of Philosophy in Mechanical Engineering, University of California, San Diego, California, San Diego

PUBLICATIONS

Nazarian, Negin; Martilli, Alberto; Kleissl, Jan, "Realistic Urban Heating and Pollutant Concentration: Part I, Flow and Turbulent Characteristics", *Boundary Layer Meteorology*, in preparation, 2016.

Nazarian, Negin; Martilli, Alberto; Kleissl, Jan, "Realistic Urban Heating and Pollutant Concentration: Part 2, Air Quality and City Breathability", *Boundary Layer Meteorology*, in preparation, 2016.

Fan, Jipeng; Nazarian, Negin; Kleissl, Jan, "A New Numerical Simulation Model for Standard Effective Temperature", *Urban Climate*, in preparation, 2016.

Nazarian, Negin; Kleissl, Jan, "Realistic solar heating in urban areas: Air exchange and street-canyon ventilation", *Building and Environment*, 95, 75-93, 2016.

Nazarian, Negin; Kleissl, Jan,"CFD simulation of an idealized urban environment: Thermal effects of geometrical characteristics and surface materials", *Urban Climate*, 12, 141-159, 2015.

Gunathilak, Gandherva; Prasannakumar, Aiswarya; Nazarian, Negin; Naeimi, Homa, "A generalized event driven framework for building occupancy (WIP)", *In Proceedings of the Symposium on Simulation for Architecture and Urban Design*, p. 26, 2013.

ABSTRACT OF THE DISSERTATION

Implications of Three-Dimensional Urban Heating on Fluid Flow and Dispersion

by

Negin Nazarian

Doctor of Philosophy in Engineering Sciences (Mechanical Engineering)

University of California, San Diego, 2015

Professor Jan P. Kleissl, Chair
Professor Daniel Tartakovsky, Co-Chair

As urbanization progresses, microclimate modifications are also aggravated, and more comprehensive and advanced methods are required to analyze the increasing environmental concerns. Among various factors that alter urban environments from undisturbed climates, street level air pollution due to vehicular exhausts is of major concern and is significantly affected by atmospheric motion and stability. Thermal forcing is shown to play an important role in determining flow patterns and pollutant dispersion in built environments, yet numerical studies of dispersion at microscale in

urban areas are limited to simplified and uniform thermal conditions and the analyses on the effect of realistic surface heating are scarce.

To address this shortcoming, a detailed indoor-outdoor building energy model is employed to compute heat fluxes from street and building surfaces, which are then used as boundary condition for a Large-Eddy Simulation model. In comparison with previous studies, our model considers the transient non-uniform surface heating caused by solar insolation and inter-building shadowing, while coupling the indoor-outdoor heat transfer, flow field and passive pollution dispersion. Series of fluid flow and thermal field simulations are then performed for an idealized, compact mid-rise urban environment, and the pollution dispersion as well as turbulent exchange behavior in and above buildings are investigated. Additionally, a potentially universal characterization method of the flow field under realistic surface heating is evaluated, which aims of expand the results into a wider range of scenarios and investigate the potential correlations for various parameters of interest.

Chapter 1

Introduction and Motivation

In modern societies, cities are the hubs for technology, culture, economy and politics, and urbanization is seen as the solution for resource efficiency and financial growth. As a result, the global trend in urbanization is experiencing the largest boom in history. According to the 2014 World Urbanization Prospects [1], more than 78% of the population in developed countries already lives in urban areas. The rest of the world is catching up, and by 2050, over two-thirds of the world population is expected to live in cities. The projected distribution of urban population for year 2030 in contrast with year 1990 (Figure 1.1) also indicates that the urbanization trend is seen for both developed and developing countries.

The global trend in urbanization significantly impacts climate in various ways [2–4]. The most important anthropogenic factors are attributed to land-use modification, emissions of greenhouse gasses, alternation of radiation balance, and wind sheltering within the street canyons [5]. Additionally, the contrast between the urban and undisturbed climates is enhanced by the input of anthropogenic heat, moisture, and noise into the atmosphere by human activities [6].

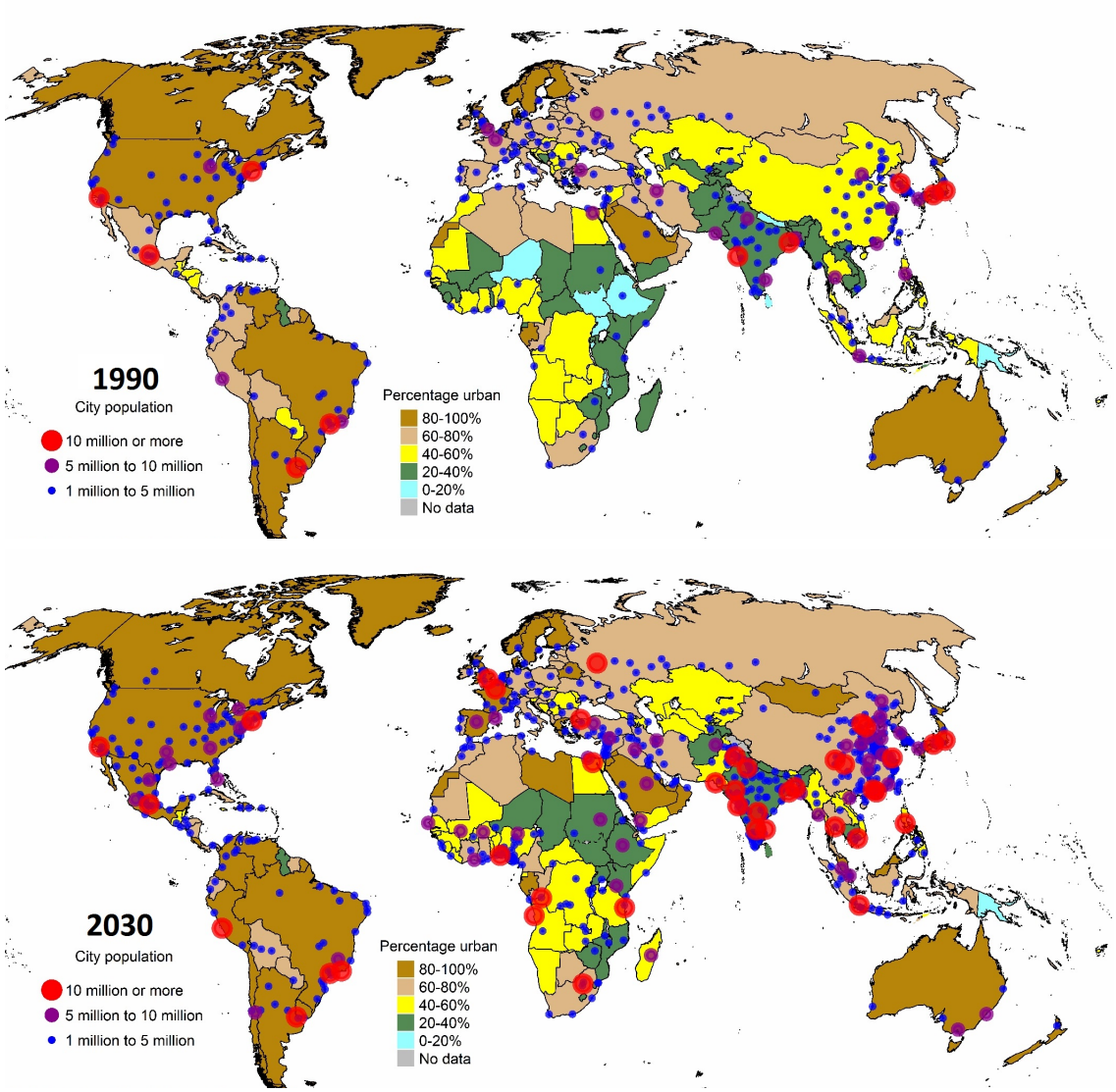

Figure 1.1: Percentage of urban area and city population at year 1990 and the projected distributions for year 2030. Maps are adopted from the World Urbanization Prospect, the 2014 revision [1].

Major Environmental Challenges - Climate modifications cause a wide scope of environmental challenges occurring over a wide range of spatial scales [8]. Urban heat island (UHI) [5], which develops when urban cooling rates are slower than rural ones, is one phenomenon that becomes prevalent with urbanization and affects climate in multiple scales. In the pedestrian level (microscale), the increase in UHI

intensity exposes the city dwellers to discomfort and human health issues and leads to higher energy demand for cooling of individual buildings. Additionally, the population increase combined with wind sheltering in street canyons gives rise to urban air quality concerns in the street scale. At larger scales (neighbourhood and city scales), UHI and the modified topography affect the flow field and alter precipitation patterns, increasing the possibility of extreme weather events and ultimately generating the global effects on climate and climate change.

Why Urban Microclimatology? The key importance of urban microclimatology lies in understanding the pedestrian-/street-scale phenomena and processes. In case of major city expansion, urban redevelopment, or new town design, the science of urban climate can be used as the guideline for planners and architects to achieve the design that is in harmony with the environment. In already existing cities, on the other hand, the microclimate analysis can propose mitigation strategies for human comfort and air quality concerns. Furthermore, the significance of microclimate analysis does not end at the microscale. In larger scales of interest, such as meso-scale modeling of urban environments, detailed and accurate understanding of microscale is required for parametrization of street-scale processes.

It is important to expand the scientific knowledge of urban climate change, but one should not forget the purpose and public concern to which they respond. After addressing this question "how does urban design interact with microclimate, human health, and ultimately global climate change?", another comes to mind: "how, and to what extent, can the urban analysis be applied to decision-making on urban design policies?" Answering these questions is what eventually leads to a holistic urban climate analysis, achieving a science-based foundation for urban design policies (such

as zoning, emission level, and air-conditioning regulations) and remaining focused on what ultimately matters: people.

1.1 Objectives, Novelty of the Research and Outline

With the rise in urbanization and ensuing environmental concerns, it is evident that more sophisticated and comprehensive methods of urban analysis are needed. Thus in this thesis, we aim to expand the understanding of urban microclimatology by addressing the following topics:

- *Thermal Effects of Urban Characteristics and Surface Materials*: Evaluating the relative importance of various design parameters, such as urban density, surface materials, and local weather conditions on the temperature and energy balance of urban facets,

- *Flow Field and Building Canyon Ventilation*: Investigating the mean flow and turbulence statistics under realistic surface heating, as well as distribution of local convective heat transfer coefficients and 3-dimensional air exchange rate from urban streets,

- *Pollutant Dispersion*: Examining the effect of surface heating on pollutant distribution in the street canyon, and investigating the rate of pollution removal from street canyons that further quantifies the city breathability,

- *Turbulent transfer*: Understanding the modification of turbulent structures due to the realistic surface heating, and mechanisms involved in turbulence exchange

of momentum, heat, and pollutants.

In addition to these objectives, a potentially universal characterization method of the flow field under realistic surface heating is evaluated. The aim of this analysis is to expand the results into a wider range of scenarios and investigate the potential correlations for various parameters of interest.

The novelty of this research lies in three aspects. 1) Comprehensiveness: the following study constitutes an example of comprehensive methodology that considers the impact of surface heating on pedestrian wind flow, thermal stresses, air quality, and building energy consumption. Accordingly, the boundary conditions of the numerical model are chosen carefully to incorporate the heat transfer due to indoor/outdoor energy balance, realistic wind and temperature profiles, and heat transfer from the soil layers. 2) Realistic representation: the effect of 3-D non-uniform and transient heating of urban surfaces is evaluated. Additionally, the results are done for a 3-D configuration of urban environment, which is a closer representation of American cities, or residential/industrial zones as opposed to 2-D street canyons. The configuration used is in the range of open low-rise to compact mid-rise classification zone with low vegetation. 3) Advanced numerical modeling: Large Eddy Simulation (LES) is employed and demonstrated as a superior method compared to the Unsteady Reynolds-Averaged Navier Stokes (URANS) and Detached Eddy Simulation (DES) models when validated against experimental data. LES modeling allows a detailed evaluation of turbulent exchange in the building roughness sublayer and inertial layer that is not possible using URANS and DES methods.

The following report is outlined as follows. The relevant theory of urban microclimatology and research methods are described in section 2. The research

objectives are addressed through a series of numerical fluid flow, heat transfer, and pollutant dispersion simulations of idealized urban environments. In all simulations unsteady simulations are forced with the realistic thermal forcing that is caused by solar insolation and inter-building shadowing. Chapter 3 investigates the diurnal cycle of urban thermal environment and the relative importance of urban design parameters, such as urban density, wind direction and speed, and surface albedo. For the flow analysis, simulations at different times of day are performed using Large Eddy Simulation (LES) and mean flow and turbulence statistics are investigated as determinants for urban canyon ventilation in Chapter 4. Additionally, the differential surface heating of the building canyon is parameterized using sets of horizontal and vertical Richardson numbers, indicating atmospheric instability and solar tilt with respect to the wind direction, respectively. The validity of this characterization method is further investigated and the results are extended to the pollutant dispersion in the street canyon in Chapter 5. Additionally, the modification of coherent structures under realistic surface heating is analyzed, and the correlation with the proposed characterizaztion method is evaluated. Concluding remarks are are made in Chapter 6.

Bibliography

[1] United Nations, Department of Economic and Social Affairs, Population Division. World Urbanization Prospects: The 2014 Revision. CD-ROM Edition Data in digital form, 2015.

[2] Helmut E Landsberg. *The urban climate*, volume 28. Academic press, 1981.

[3] Timothy R Oke. Review of urban climatology, 1968-1973. 1974.

[4] Timothy R Oke. Review of urban climatology, 1973-1976. 1979.

[5] Timothy R Oke. *Boundary layer climates. 2nd*. 1987.

[6] Haider Taha. Urban climates and heat islands: albedo, evapotranspiration, and anthropogenic heat. *Energy and buildings*, 25(2):99–103, 1997.

[7] Timothy R Oke. *City size and the urban heat island Atmospheric Environment*, 7(8):769-779. 1967.

[8] Moonen, P., Defraeye, T., Dorer, V., Blocken, B., and Carmeliet, J. *Urban Physics: Effect of the micro-climate on comfort, health and energy demand. Frontiers of Architectural Research*, 1(3), 197-228. 2012.

[9] Howard, L., *The climate of London deduced from meteorological observations*, Harvey and Darton, London, Volume 1, 1833.

[10] T. R. Oke, *The energetic basis of the urban heat island*, Q J ROY METEOR SOC, $108 : 1 - 24$, 1982.

[11] T. R. Oke, G. Johnson, D. Steyn, and I. Watson, *Simulation of surface urban heat islands under ideal conditions at night. Part 2: Diagnosis of causation*, BOUND-LAY METEOROL, $56 : 339 - 358$, 1991.

Chapter 2

Background and Theory

2.1 Atmospheric Boundary Layer: Characteristics and Structure

The atmospheric boundary layer (ABL) is the layer of troposphere closest to the earth surface that directly responds to surface forcings (such as friction and heat fluxes) within the time scale of an hour [1]. ABL depth ranges from 100 meters to several kilometers, and is characterized by the diurnal components (diurnal and nocturnal variation of surface heat fluxes), complex terrain morphology (surface elements such as hills, forests and built environment), and larger weather events (prevailing winds; clouds and precipitation). Turbulence governs the ABL dynamics and microphysics, and is mostly driven by wind shear. Additionally, the temperature gradients due to the surface heat flux can either enhance or suppress the ABL turbulence.

The vertical structure of the ABL is briefly outlined here. Figure 2.1 illustrates a typical diurnal evolution of the atmospheric boundary layer over land under clear skies.

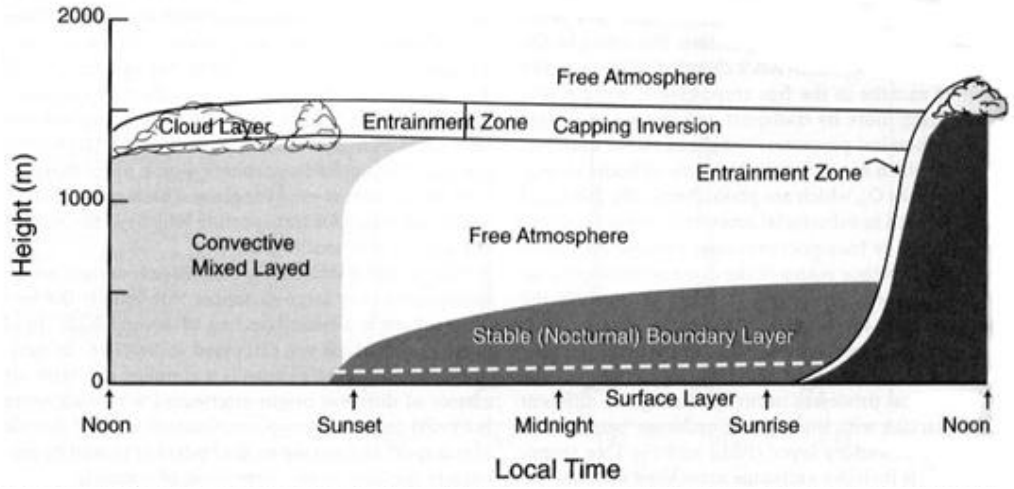

Figure 2.1: Typical diurnal evolution of the atmospheric boundary layer under a high pressure system. Adopted from Stull 1988 [1]

Analogous to the wall boundary layer, ABL can be divided into the *surface (inner) layer*, and the outer region in which the turbulence is assumed to be independent of surface roughness. The outer layer is then divided into *convective mixed layer (CBL)* formed due to the solar heating during daytime, and the *stable (nocturnal) boundary layer (SBL)* mainly due to the radiative cooling (Figure 2.1). It is worth mentioning that nocturnal boundary layer may also be convective when cold air advects over a warm surface.

The surface layer above a rough surface usually covers the lowest 10% of the ABL and can be further divided into an *inertial sublayer* and a *roughness sublayer*[2]. The inertial sublayer is the region where the flow is not influenced by single roughness elements and fluxes are nearly constant with height, hence, it is also called the *constant flux layer*. On the contrary, within the roughness sublayer, time averaged turbulence statistics and flux densities are vertically and horizontally inhomogeneous, and local horizontal transports are not negligible. In the present work, we focus on processes in the surface layer (urban boundary layer) and specifically on its roughness sublayer

that is the focus of urban microclimatology.

2.2 Urban Physics

Urban microclimatology is a well-established field of study and incorporates branches of physics, aerodynamics, meteorology, chemistry, and statistics. To aid discussion, the present chapter outlines the fundamental concepts of Urban Physics, as well as research methods and literature that are relevant to the scope of this work.

2.2.1 Scale of Interest

An appreciation of spatial scale is key to the understanding of meteorology and urban climate. Meteorological phenomena occur over a wide range of space and time scales, commonly classified into three categories of micro, meso and macro scales, summarized in Table 2.1. The phenomena occurring in these scales are interrelated and each scale incorporates several sub-scales depending on the physical processes of interest.

Table 2.1: Time and space scales of atmospheric motion.

Scale	Space	Time
Micro	Meters	Seconds - Minutes
Meso	Kilometers	Seconds - Hours
Macro (Synoptic)	100 - 1000 km	Days
Macro (Planetary)	>1000 km (global)	Days - Weeks

Phenomena, such as turbulence, with time and space scales smaller than about 3km and 1hr are classified as *microscale*. Additionally, in the context of urban microclimatology, Britter and Hanna [3] further defined horizontal scales as follows.

- *Street scale* with phenomena in order of 10-100 m: detailed dispersion, flow and turbulence exchange within street canyons are analyzed to address the horizontal and vertical inhomogeneities in the building roughness sublayer.

- *Neighbourhood scale* with spatial order of 100-1000 m: repetitive horizontal inhomogeneities at the street scale are filtered out which allows many simplifications, but requires parameterizations of underlying urban roughness and canopy sublayer.

- *City and regional scale* in order of 1-20 km: the modification of the entire boundary layer (mixed layer) due to the presence of urban area is analyzed, and detailed processes in the urban roughness sublayer are not of central importance anymore.

Analysis done in each scale responds to different concerns in urban climatology. Accordingly, depending on the scale of interest, certain processes may be neglected, parametrized, or directly solved in a model. In the present study, we focus on the street scale, which can be particularly of interest for urban dwellers, architects, urban planners and advocates for improving air quality in urban areas.

2.2.2 Research Methods

Studies of the urban climate have been conducted for over 150 years, dating back to the first observations of temperature elevation in big cities such as London and Paris [4]. Since then, much research are done in Urban climatology using three main research methods: field measurements, wind tunnel experiments and numerical simulations based on Computational Fluid Dynamics (CFD). The importance and

challenges of each method are described here, and few examples of significant works in the street-scale climate are mentioned.

Field measurements

The real complexity of the urban climate can only be represented with field experiments. Therefore, if conducted accurately and for a sufficiently long period, field measurements are invaluable to the understanding of atmospheric flow and are used to validate the wind tunnel measurements and numerical models. Major flow observations and measurement campaigns that analyzed the distribution of air temperature and wind velocity in the building roughness sublayer are Nakamura and Oke [5], Voogt and Grimmond [6], Kanda et al. [7], Niachou et al. [8], and Shahrestani et al. [9]. These studies are repeatedly used for evaluations of CFD models for pedestrian wind field. In the pollutant dispersion studies, major field campaign studies include full-scale measurements by DePaul and Sheih [10], Nakamura and Oke [5], Qin and Kot [11], Berkowicz et al. [12], and xie et al [13]. Additionally, number of large field campaigns have been conducted, such as the Joint Urban 2003 field study that gathered data over the course of 34 days [14], and the "Dispersion of Air Pollution and its Penetration into the Local Environment" (DAPPLE) project conducted in Westminster, London, executing five field campaigns over the course of 2003-2008 [15].

The biggest challenges concerning field measurements are as follow. First, the spatial and temporal extent and resolution are limited in field measurements. Second, point measurements are mostly performed under largely uncontrolled conditions (from both meteorological and anthropogenic aspects), and falls short in representing the wide range of possible scenarios. Third, the complexity of real-world settings restricts

general conclusions from the data, since "repeatability" does not often happens due to sudden weather events and human activities. These challenges motivate the employment of wind tunnel experiments and CFD models, in which the boundary conditions are controllable and certain parameters of interest can be varied more easily.

Wind tunnel measurements

In the field of Urban Physics, wind tunnel experiment is a valuable tools for evaluating the wind flow, temperature field and pollutant dispersion in the street-scale. Additionally, the obtained data can be used for assessing the degree of uncertainty in field campaign measurements. The most common techniques for wind-tunnel experiments are based on Thermal Anemometry (TA), Laser Doppler Velocimetry (LDV), and Particle Imaging Velocimetry(PIV) for measuring velocities and temperature, and the Flame Ionisation Detector(FID) for concentration measurements. Few wind tunnel experiments have been conducted to analyze the turbulent flow, and the coupled behavior of thermal stratification with flow field in urban-like roughness, such as Meinders and Hanjalic [16], Uehara et al. [17], Richards et al. [18], and Allegrini et al. [19]. Additionally, pollutant dispersion studies include Meroney and Pavageau [20], Kastner-Klein and Plate [21], Baker and Hargreaves [22], Kastner-Klein and Fedorovich [23], and Kastner-Klein and Rotach [24].

Similar to field measurements, wind tunnel experiments are limited in scale, and can only represent a scale model of a real geometry of urban areas. Additionally, experimental setups impose a variety of limitations (such as ensuring the similarity criteria [25]) and can be very time-consuming and costly. Accordingly, in order to

capture the scale and complexity of urban environments, numerical experiments have been conducted for a more holistical examination of urban microclimate.

Numerical simulations

Computational Fluid Dynamics has been widely used in various research fields, such as aeronautics, oceanic flows, and atmospheric flows, and has several advantages compared to the other methods. First, a very high spatial and temporal resolution can be achieved in the region of interest, and there is no restrictions on the geometry of the computational model as opposed to wind-tunnel experiments. Accordingly, building geometries and scalars can be modeled in their actual scale. Second, the detailed three dimensional flow and scalar field can be obtained using numerical models, and surface-averaged (or volume-averaged) quantities are easily obtainable.

There is a multitude of CFD simulation of street-scale environment and giving a comprehensive overview is beyond the scope of this chapter. The reader is referred to Li et al. [26] and Moonen et al. [25] for the review and summary of the progresses in CFD modeling of wind field and pollutant transport in street canyons. Here, we summarize the most important CFD simulations of urban street canyons that form the critical background of the following thesis: CFD modeling is widely used in the investigation of a) flow structures and numerical methods for turbulence modeling of urban sublayer, including Cheng et al.[27], Kanda et al. [28], Xie and Castro [29], Coceal et al. [30, 31], Santiago et al. [32], and Letzel et al. [33]; b) dynamic thermal and flow field behavior in unstable conditions such as Kim et al. [34], Li et al. [35], Park et al. [36], Yaghoobian et al. [37], and Santiago et al. [38]; and c) passive scalar dispersion, e.g. Li et al. [39], Cheng and Liu [40], Park et al. [36], and Tan et al. [41].

The limitation of the CFD modeling lies in the selection of the most-appropriate turbulence model, as well as specification of modelling parameters. For instance, when wall functions are used, it is very important that the wall function roughness parameters are determined accurately based on their aerodynamic roughness length in the inlet velocity profiles (Blocken et al.,2007a). It is also crucial that the turbulence models are chosen according to the scale, needed level of accuracy, and parameters of interest. Lastly, CFD simulations require massive computational resources. Therefore, in spite of the current advancement in supercomputing, the limit in computational resource is often a decisive factor in the choice of modelling approach, or geometries of interest.

2.2.3 Atmospheric Flow and Turbulence

Turbulence is an intrinsic part of the atmospheric boundary layer, and the correct representation of the turbulence is critical in providing good climate analysis. Several key features of turbulence in the atmospheric flow is as follows:

1) Instantaneous and single motions in a turbulent flow are chaotic and unpredictable. This characteristic is often referred to as "quasi-randomness".

2) Turbulent flow can be presented as a superposition of a spectrum of flow velocity fluctuations and eddies upon a mean flow. The ability to find a statistically-stable mean value indicates that turbulence is not entirely random [1], explaining the term "quasi-randomness" used for instantaneous turbulent flow.

3) There is a measurable and definable intensity to the turbulence, and parameters vary in a limited range. Therefore, variances and standard deviations can be defined to characterize the intensity of turbulent flow, and the integral effects of turbulence indicates the dispersion and exchange processes.

Governing Equations of Turbulent flow

The equations of fluid mechanics that describe the dynamics and thermodynamics of gasses are used to quantify the atmospheric boundary layer. In this section, we start with basic governing equations, and further describe the statistical tools and concepts that are used for a meaningful representation of the turbulent flow.

The Reynolds decomposition provides the basics for statistical description of turbulent flow, and splits any instantaneous variable a at a given location and time into a resolved mean value (denoted by an overbar) and an unresolved fluctuating part (denoted by a prime),

$$a = \overline{a} + a' \,. \tag{2.1}$$

$\overline{a}$ is the temporal average over an averaging time Ti, such that the following assumptions are fulfilled: a) quasi-stationarity condition, and b) Ti lies in the region of the spectral gap [1] which results from an energetic separation of the energy input at the synoptic scale and the energy produced at the turbulent scale (Stull [1]):

$$\overline{a} = \int_0^{Ti} a \, dt \,. \tag{2.2}$$

With the Reynolds decomposition (Eq. 2.1) applied to the conservation equations of mass, momentum and heat, we get the Boussinesq equations for the mean motions in the turbulent atmosphere (derivations are skipped for brevity. See Panofsky and Dutton [42], and Stull [1] for details). In the inner region, Coriolis forces are neglected, and the Reynolds decomposed conservation of continuity and momentum is rewritten as

$$\frac{\partial \overline{u_i}}{\partial x_i} = 0 \ , \tag{2.3}$$

$$\frac{\partial \overline{u_i}}{\partial t} + \overline{u_j}\frac{\partial \overline{u_i}}{\partial x_j} = -\delta_{i3} g - \frac{1}{\overline{\rho}}\frac{\partial \overline{p}}{\partial x_i} + \frac{\nu \partial^2 \overline{u_i}}{\partial x_j^2} - \frac{\partial \overline{u_i' u_j'}}{\partial x_j} \ . \tag{2.4}$$

Note that i and j indicate summation according to Einsteins convention for the three Cartesian axis i, j = [1, 2, 3]. The terms from left to right are: storage of mean momentum, advection of mean momentum, gravity acceleration in the vertical direction, pressure gradient forces, viscous stress on the mean motions and Reynolds stress.

Additionally, the conservation equation for any scalar quantity such as (virtual) temperature, passive pollutant and moisture is as follow

$$\frac{\partial \overline{s}}{\partial t} + \overline{u_j}\frac{\partial \overline{s}}{\partial x_j} = \frac{\nu \partial^2 \overline{s}}{\partial x_j^2} + S_s - \frac{\partial \overline{s' u_j'}}{\partial x_j} \ . \tag{2.5}$$

The terms from left to right are: storage, advection, mean molecular diffusion, net source or sink term, and the divergence of turbulent flux densities. S_s then varies depending on the scalar parameter.

The last term in previous equations (Eq. 2.4 and 2.5) contains a covariance (second order moment). In order to solve the equations, additional prognostic equations are derived to predict the variances and covariances, that describe the turbulence intensity and kinematic turbulent fluxes, respectively [1]. However, by introducing the prognostic equations for the previously unknown second moments (such as $\overline{u_i' u_j'}$), new third-order terms appear that is not predictable. This is called closure problem: with each higher order set of equations, more unknown terms appear, therefore,

approximation of missing higher order moments are required at certain level of accuracy. The most common closure scheme is the *Gradient Transport Theory* or *K-theory*, which approximates turbulent transports with a transfer coefficient K, proportional to the local gradient of mean quantities. A comprehensive description of turbulence closure techniques can be found in Stull [1].

Turbulence Modeling

Computational Fluid Dynamic refers to using numerical analysis and algorithms to solve and model governing equations of fluid flows. Although equations of motion can be directly applied to turbulent flows, rarely we have sufficient initial and boundary condition information, and/or resources available to resolve all turbulent scales, specifically for resolving the smallest energy containing eddies. Additionally, depending on the scale or application of interest, it might not even be relevant to resolve all eddy motions. Therefore, some degree of turbulence modelling is often performed, especially when the complexity of the problem is increased for three-dimensional, transient, high-Reynolds number turbulent flows in complex geometries.

According, turbulent models are developed to include the statistical effects of turbulence with reasonable accuracy in the scale of interest. Turbulence models are classified by the turbulent scale threshold they choose to resolve explicitly, or model. The most commonly used models in urban climatology are: a) Reynolds-averaged Navier-Stokes (RANS), where the mean flow field is explicitly resolved and a time averaging process is used to remove the necessity of simulating all of the scales of the turbulence spectrum; b) Large Eddy Simulation (LES), where the large, energy-containing eddies are resolved, while the small-scale eddies are modeled with

a subgrid-scale model, such as (Dynamic) Smagorinsky model [43] and Algebraic Wall Subgrid-Scale Model [44]; c) hybrid RANS-LES models such as Detached Eddy Simulation, where RANS is used in the inner-wall region, and LES is used in the core region of the flow [45]; and d) Direct Numerical Simulation where all turbulence scales are resolved numerically [46]. Detailed description of the turbulence models that are used in the scope of this thesis are explained in each corresponding chapter.

2.2.4 Statistical Description of Turbulence

Integral Statistics

Following equation 2.2, the higher order statistical moments can be defined as:

$$\overline{a'^i} = \frac{1}{T_i} \int_{t=0}^{Ti} a'^i(t) dt \,, \tag{2.6}$$

where i defines the order of the moment. Accordingly, the second order moment with $i = 2$ is the variance, the measure of the deviation of data about the mean, and its square root σ_a is defined as the standard deviation:

$$\sigma_a = \sqrt{\overline{a'^i}} \,. \tag{2.7}$$

The higher order moments can further be defined. For instance, the third order moment normalized with variance is called skewness, and is defined as

$$Sk_a = \frac{\overline{a'^3}}{{\sigma_a}^3} \,. \tag{2.8}$$

Additionally, the general form of two-variable moments of any variable a and b is

$$\overline{a'^i b'^j} = \frac{1}{T_i} \int_{t=0}^{Ti} a'^i(t) b'^j(t) dt \,. \tag{2.9}$$

When $i = 1$, the integral indicates the covariance that is the degree of common relationship between the two variable, a and b. The nonlinear turbulence products that were discussed in the context of *closure problem* in Section 2.2.3 have the same meaning as covariance. The normalized covariance is then defined as the linear correlation coefficient, r_{ab},

$$r_{ab} = \frac{\overline{a'b'}}{\sigma_a \sigma_b} \,. \tag{2.10}$$

It is common to partition the kinetic energy (KE) of the flow into mean kinetic energy (MKE) and turbulent kinetic energy (TKE), and compute the contribution of turbulence to the energy of the flow:

$$\frac{1}{2}{u_i}^2 = \frac{1}{2}\overline{u_i}^2 + \frac{1}{2}{u_i'}^2 \tag{2.11}$$

Therefore, TKE can be written as the sum of the diagonal components of the velocity covariance tensor $M_{ij} = \overline{u_i' u_j'}$. The off-diagonal components are Reynolds Stresses that accounts for the momentum exchange due to the turbulent fluctuations.

Characteristic Time and Length Scale

Turbulent motions occur over a wide range of time and length scales. For any two parameters a and b, we can define a general form of an Eulerian covariance tensor

that relates the value of a' at any point $\mathbf{x}$ and any time t to the value of b' at location x^1 in a distance $\mathbf{r}$=x^1-$\mathbf{x}$ and a time t^1 that has a time-lag $\tau = t^1 - t$ (Rotta, 1972):

$$\mathrm{C}_{ab}(\mathbf{x}, t, \mathbf{r}, \tau) = \overline{a'(\mathbf{x}, t) b'(\mathbf{x}+\mathbf{r}, t+\tau)}\,. \tag{2.12}$$

Variance and covariance defined before (Eq. 2.7 and 2.9) are the special cases of this equation with $\tau = 0$ and $\mathbf{r} = 0$. Additionally, the normalized correlation tensor is given by

$$\mathrm{R}_{ab}(\mathbf{x}, t, \mathbf{r}, \tau) = \frac{\overline{a'(\mathbf{x}, t) b'(\mathbf{x}+\mathbf{r}, t+\tau)}}{\overline{a'(\mathbf{x}, t)^2}\;\overline{b'(\mathbf{x}+\mathbf{r}, t+\tau)^2}}\,. \tag{2.13}$$

When $|\mathrm{r}| \to \infty$ or $\tau \to \infty$, a' and b' become statistically independent and $\mathbf{R}_{\mathrm{ab}} = 0$.

Probability Density Functions

A complete description of a turbulent variable a at a given position and time is given by the probability density function (PDF), $P(a)$, where $P(a)da$ is the probability of the variable a taking a value between a and $a + da$, and

$$\int_{-\infty}^{\infty} P(a)da = 1\,. \tag{2.14}$$

Accordingly, if a and b are two parameters of the flow (such as velocity and temperature), the joint probability density function (JPDF), $P(a, b)$, can be defined as the probability of the variable a taking a value between a and $a + da$ while b has a value between b and $b + db$, which again satisfies

$$\int \int_{-\infty}^{\infty} P(a,b) da db = 1 \,. \tag{2.15}$$

Quadrant Analysis and Measures

The theory of quadrant analysis is described here. The quadrant analysis was first introduced by Lu and Willmarth (1973), where the joint probability of u' and w' is decomposed into four quadrant events according to the sign of the fluctuating components: The events in quadrant 2 and 4 ($u'w' < 0$) called ejections and sweeps, respectively, indicate the coherent structures that contribute positively to the downward momentum flux, and events in quadrant 1 and 3 ($u'w' > 0$) called outward and inward interaction, respectively, that represent the intermittency of turbulence. Figure 2.2 shows the joint probability of $u'w'$ at the roof level for an unstable condition measured by Christen et al. [47] and the schematic of quadrant analysis are shown. The numbers indicated in each box represent the frequency of occurrence for each event.

Furthermore, the contribution of each event to the total flux density can be computed as the flux (or stress) fraction, S_i, introduced by Raupach (1981)

$$S_i = \frac{1}{r_{ab}} \int_{l_a}^{u_a} \int_{l_b}^{u_b} ab P(a,b) da db \,. \tag{2.16}$$

From equations 2.15 and 2.16, it is seen that

$$\Sigma_{i=1}^{4} S_i = 1 \,. \tag{2.17}$$

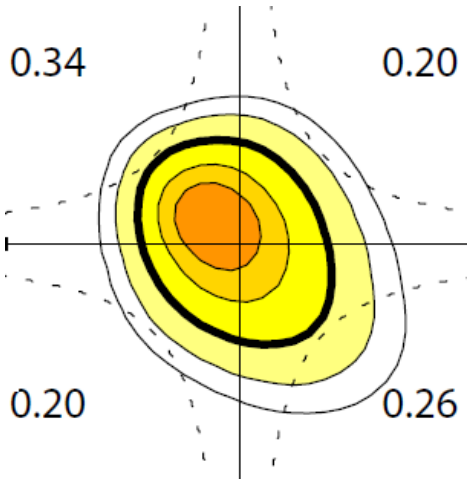

Figure 2.2: Normalized JPDFs of $u'w'$ at the roof level for an unstable condition measured by Christen et al. [47] and the schematic of quadrant analysis.

From the stress fraction S_i, two measures of the relative importance of sweeps and ejections can be obtained: The difference between ejections (low momentum eddies moving up) and sweeps (high momentum eddies moving down)

$$\Delta S_0 = S_4 - S_2 \,. \tag{2.18}$$

and their ratio

$$\gamma = S_2/S4 \,, \tag{2.19}$$

Furthermore, Shaw et al. (1983) introduced Exuberance, Exu, as the the ratio of unorganized to coherent events that indicates the efficiency of turbulence exchange

$$sExu = \frac{S_1 + S_3}{S_2 + S_4} \,. \tag{2.20}$$

Bibliography

[1] Roland B Stull. *An introduction to boundary layer meteorology*, volume 13. Springer Science & Business Media, 1988.

[2] MR Raupach, RA Antonia, and S Rajagopalan. Rough-wall turbulent boundary layers. *Applied Mechanics Reviews*, 44(1):1–25, 1991.

[3] RE Britter and SR Hanna. Flow and dispersion in urban areas. *Annual Review of Fluid Mechanics*, 35(1):469–496, 2003.

[4] L Howard. The climate of london, vols. i–iii. *London: Harvey and Dorton*, 1883.

[5] Y Nakamura and TR Oke. Wind, temperature and stability conditions in an east-west oriented urban canyon. *Atmospheric Environment (1967)*, 22(12):2691–2700, 1988.

[6] James A Voogt and CSB Grimmond. Modeling surface sensible heat flux using surface radiative temperatures in a simple urban area. *Journal of Applied Meteorology*, 39(10):1679–1699, 2000.

[7] M Kanda, M Kanega, T Kawai, R Moriwaki, and H Sugawara. Roughness lengths for momentum and heat derived from outdoor urban scale models. *Journal of Applied Meteorology and Climatology*, 46(7):1067–1079, 2007.

[8] K Niachou, I Livada, and M Santamouris. Experimental study of temperature and airflow distribution inside an urban street canyon during hot summer weather conditions. part ii: Airflow analysis. *Building and Environment*, 43(8):1393–1403, 2008.

[9] Mehdi Shahrestani, Runming Yao, Zhiwen Luo, Erdal Turkbeyler, and Hywel Davies. A field study of urban microclimates in london. *Renewable Energy*, 73:3–9, 2015.

[10] FT DePaul and CM Sheih. Measurements of wind velocities in a street canyon. *Atmospheric Environment (1967)*, 20(3):455–459, 1986.

[11] Y Qin and SC Kot. Dispersion of vehicular emission in street canyons, guangzhou

city, south china (prc). *Atmospheric Environment. Part B. Urban Atmosphere*, 27(3):283–291, 1993.

[12] Ruwim Berkowicz, Finn Palmgren, Ole Hertel, and Elisabetta Vignati. Using measurements of air pollution in streets for evaluation of urban air qualitymeterological analysis and model calculations. *Science of the total environment*, 189:259–265, 1996.

[13] Shaodong Xie, Yuanhang Zhang, Li Qi, and Xiaoyan Tang. Spatial distribution of traffic-related pollutant concentrations in street canyons. *Atmospheric Environment*, 37(23):3213–3224, 2003.

[14] K Jerry Allwine, MJ Leach, LW Stockham, JS Shinn, RP Hosker, JF Bowers, and JC Pace. Overview of joint urban 2003an atmospheric dispersion study in oklahoma city. In *Preprints, Symp. on Planning, Nowcasting and Forecasting in the Urban Zone, Seattle, WA, Amer. Meteor. Soc., CD-ROM J*, volume 7, 2004.

[15] SJ Arnold, H ApSimon, J Barlow, S Belcher, M Bell, JW Boddy, R Britter, H Cheng, R Clark, RN Colvile, et al. Introduction to the dapple air pollution project. *Science of the Total Environment*, 332(1):139–153, 2004.

[16] ER Meinders and K Hanjalić. Vortex structure and heat transfer in turbulent flow over a wall-mounted matrix of cubes. *International Journal of Heat and Fluid Flow*, 20(3):255–267, 1999.

[17] Kiyoshi Uehara, Shuzo Murakami, Susumu Oikawa, and Shinji Wakamatsu. Wind tunnel experiments on how thermal stratification affects flow in and above urban street canyons. *Atmospheric Environment*, 34(10):1553–1562, 2000.

[18] K Richards, M Schatzmann, and B Leitl. Wind tunnel experiments modelling the thermal effects within the vicinity of a single block building with leeward wall heating. *Journal of wind engineering and industrial aerodynamics*, 94(8):621–636, 2006.

[19] Jonas Allegrini, Viktor Dorer, and Jan Carmeliet. Wind tunnel measurements of buoyant flows in street canyons. *Building and Environment*, 59:315–326, 2013.

[20] Robert N Meroney, Michel Pavageau, Stilianos Rafailidis, and Michael Schatzmann. Study of line source characteristics for 2-d physical modelling of pollutant dispersion in street canyons. *Journal of Wind Engineering and Industrial Aerodynamics*, 62(1):37–56, 1996.

[21] P Kastner-Klein and EJ Plate. Wind-tunnel study of concentration fields in street canyons. *Atmospheric Environment*, 33(24):3973–3979, 1999.

[22] CJ Baker and DM Hargreaves. Wind tunnel evaluation of a vehicle pollution dispersion model. *Journal of Wind Engineering and Industrial Aerodynamics*, 89(2):187–200, 2001.

[23] P Kastner-Klein, E Fedorovich, and MW Rotach. A wind tunnel study of organised and turbulent air motions in urban street canyons. *Journal of Wind Engineering and Industrial Aerodynamics*, 89(9):849–861, 2001.

[24] Petra Kastner-Klein and Mathias W Rotach. Mean flow and turbulence characteristics in an urban roughness sublayer. *Boundary-Layer Meteorology*, 111(1):55–84, 2004.

[25] Peter Moonen, Thijs Defraeye, Viktor Dorer, Bert Blocken, and Jan Carmeliet. Urban physics: Effect of the micro-climate on comfort, health and energy demand. *Frontiers of Architectural Research*, 1(3):197–228, 2012.

[26] Xian-Xiang Li, Chun-Ho Liu, Dennis YC Leung, and KM Lam. Recent progress in cfd modelling of wind field and pollutant transport in street canyons. *Atmospheric Environment*, 40(29):5640–5658, 2006.

[27] Y Cheng, FS Lien, E Yee, and R Sinclair. A comparison of large eddy simulations with a standard k–ε reynolds-averaged navier–stokes model for the prediction of a fully developed turbulent flow over a matrix of cubes. *Journal of Wind Engineering and Industrial Aerodynamics*, 91(11):1301–1328, 2003.

[28] Manabu Kanda, Ryo Moriwaki, and Fumi Kasamatsu. Large-eddy simulation of turbulent organized structures within and above explicitly resolved cube arrays. *Boundary-Layer Meteorology*, 112(2):343–368, 2004.

[29] Zhengtong Xie and Ian P Castro. Les and rans for turbulent flow over arrays of wall-mounted obstacles. *Flow, Turbulence and Combustion*, 76(3):291–312, 2006.

[30] O Coceal, TG Thomas, IP Castro, and SE Belcher. Mean flow and turbulence statistics over groups of urban-like cubical obstacles. *Boundary-Layer Meteorology*, 121(3):491–519, 2006.

[31] Omduth Coceal, Adrian Dobre, and T Glyn Thomas. Unsteady dynamics and organized structures from dns over an idealized building canopy. *International Journal of Climatology*, 27(14):1943–1953, 2007.

[32] Jose Luis Santiago, Alberto Martilli, and Fernando Martín. Cfd simulation of airflow over a regular array of cubes. part i: Three-dimensional simulation of the flow and validation with wind-tunnel measurements. *Boundary-layer meteorology*, 122(3):609–634, 2007.

[33] Marcus Oliver Letzel, Martina Krane, and Siegfried Raasch. High resolution urban large-eddy simulation studies from street canyon to neighbourhood scale. *Atmospheric Environment*, 42(38):8770–8784, 2008.

[34] Jae-Jin Kim and Jong-Jin Baik. Urban street-canyon flows with bottom heating. *Atmospheric Environment*, 35(20):3395–3404, 2001.

[35] Xian-Xiang Li, Rex E Britter, Leslie K Norford, Tieh-Yong Koh, and Dara Entekhabi. Flow and pollutant transport in urban street canyons of different aspect ratios with ground heating: large-eddy simulation. *Boundary-layer meteorology*, 142(2):289–304, 2012.

[36] Seung-Bu Park, Jong-Jin Baik, Siegfried Raasch, and Marcus Oliver Letzel. A large-eddy simulation study of thermal effects on turbulent flow and dispersion in and above a street canyon. *Journal of Applied Meteorology and Climatology*, 51(5):829–841, 2012.

[37] Neda Yaghoobian, Jan Kleissl, and E. Scott Krayenhoff. An improved three-dimensional simulation of the diurnally varying street-canyon flow. *Boundary-Layer Meteorology*, 153(2):251–276, 2014.

[38] JL Santiago, ES Krayenhoff, and A Martilli. Flow simulations for simplified urban configurations with microscale distributions of surface thermal forcing. *Urban Climate*, 9:115–133, 2014.

[39] Xian-Xiang Li, Rex E Britter, Tieh Yong Koh, Leslie K Norford, Chun-Ho Liu, Dara Entekhabi, and Dennis YC Leung. Large-eddy simulation of flow and pollutant transport in urban street canyons with ground heating. *Boundary-layer meteorology*, 137(2):187–204, 2010.

[40] WC Cheng and Chun-Ho Liu. Large-eddy simulation of turbulent transports in urban street canyons in different thermal stabilities. *Journal of Wind Engineering and Industrial Aerodynamics*, 99(4):434–442, 2011.

[41] Zijing Tan, Jingliang Dong, Yimin Xiao, and Jiyuan Tu. A numerical study of diurnally varying surface temperature on flow patterns and pollutant dispersion in street canyons. *Atmospheric Environment*, 104:217–227, 2015.

[42] Hans A Panofsky and John A Dutton. Atmospheric turbulence: models and methods for engineering aplications. In *Atmospheric turbulence: models and methods for engineering aplications*. John Wiley & Sons, 1984.

[43] Massimo Germano, Ugo Piomelli, Parviz Moin, and William H Cabot. A dynamic subgrid-scale eddy viscosity model. *Physics of Fluids A: Fluid Dynamics (1989-1993)*, 3(7):1760–1765, 1991.

[44] Mikhail L Shur, Philippe R Spalart, Mikhail Kh Strelets, and Andrey K Travin. A hybrid RANS-LES approach with delayed-des and wall-modelled LES capabilities. *International Journal of Heat and Fluid Flow*, 29(6):1638–1649, 2008.

[45] Philippe R Spalart, S Deck, ML Shur, KD Squires, M Kh Strelets, and A Travin. A new version of detached-eddy simulation, resistant to ambiguous grid densities. *Theoretical and Computational Fluid Dynamics*, 20(3):181–195, 2006.

[46] Parviz Moin and Krishnan Mahesh. Direct numerical simulation: a tool in turbulence research. *Annual review of fluid mechanics*, 30(1):539–578, 1998.

[47] Andreas Christen, Eva van Gorsel, and Roland Vogt. Coherent structures in urban roughness sublayer turbulence. *International journal of Climatology*, 27(14):1955–1968, 2007.

Chapter 3

Thermal Effects of Urban Design

3.1 Introduction

Understanding of urban climate requires consideration of complex relationships between various factors. Urban morphology, natural land cover, moisture availability, anthropogenic heats and built materials alter air flow and heat transfer in the urban environment, and therefore determine urban microclimates, strength of the Urban Heat Island (UHI) and the ensuing environmental effects [1–3]. Thus, with the rapid growth in population and urbanization, it is paramount that more sophisticated, realistic and comprehensive urban models are developed and applied.

The surface temperature and air flow are of prime importance to the field of urban climatology, motivating many studies over the past several decades. Flow observations and measurement campaigns in street canyons have been conducted to analyze the distribution of air temperature and wind velocity in and above the canopy, e.g. [4–8]. Additionally, wind tunnel experiments have been used to analyze the turbulent flow and the coupled behavior of thermal stratification and flow field

in regular arrays of wall-mounted cubes representing buildings [9–12]. Although these studies are invaluable in improving our understanding of the urban physics and appreciating real-world complexities, experimental setups impose a variety of limitations. Since the scale and complexity of urban environments limit the resolution of flow patterns through sensors, numerical experiments have been conducted to more wholistically examine the urban environment.

Computational Fluid Dynamics (CFD) has frequently been applied to study the flow field in street-scale environments. In specific, turbulent flow structures (e.g. [13–15]), passive scalar dispersion (e.g. [16–18]) as well as numerical methods for turbulence modeling (e.g [19–21]) have been widely investigated, and Li et al [22] reviewed and summarized the progress in CFD modeling of wind field and pollutant transport in street canyons. While these studies elucidated a variety of phenomena of turbulent urban fluid flow, they mostly did not consider the contribution of realistic three-dimensional thermal forcing to flow characteristic in the street canyon.

Alternatively, urban energy balance models are used for studying surface temperatures and thermal environments, residential cooling and heating loads, and Urban Heat Island mitigation measures [23–26], but most of these models over-simplify fluid flow and convective heat transfer. While the size and variability of roughness elements in urban areas generally cause stability conditions above the canopy to be closer to neutral than over dry natural areas, flow structures in the urban canyon are sensitive to other forcings. A few numerical simulations of dynamically-coupled thermal effects and turbulent flow in urban-like geometry have also been reported in the literature [12, 27–29] and the significance of wall and ground heating on flow characteristic have been investigated. Niceno et al [27] performed LES simulations to

analyze turbulent heat transfer from a multi-layered wall-mounted cube matrix that is heated internally and uniformly. Similarly, Li et al [28] and Park et al [29] used LES simulations to study thermal effects on turbulent flow and dispersion in and above urban-like geometries, while each building wall or canyon ground surface was heated. Furthermore, the effect of various degrees of local thermal stratification on turbulence structure and local heat transfer is investigated and compared in a recent study by Boppana et al [30]. However, to date the dynamic non-uniform heating that is caused by direct shortwave radiation received on urban surfaces and shading effects between buildings have not been addressed. Additionally, previous studies mostly examined abstractions of thermal heterogeneity rather than real diurnal cycles of urban surface temperatures and energy balance components. It is also important to consider and compare the relative importance of various urban design parameters in conjunction with local weather condition.

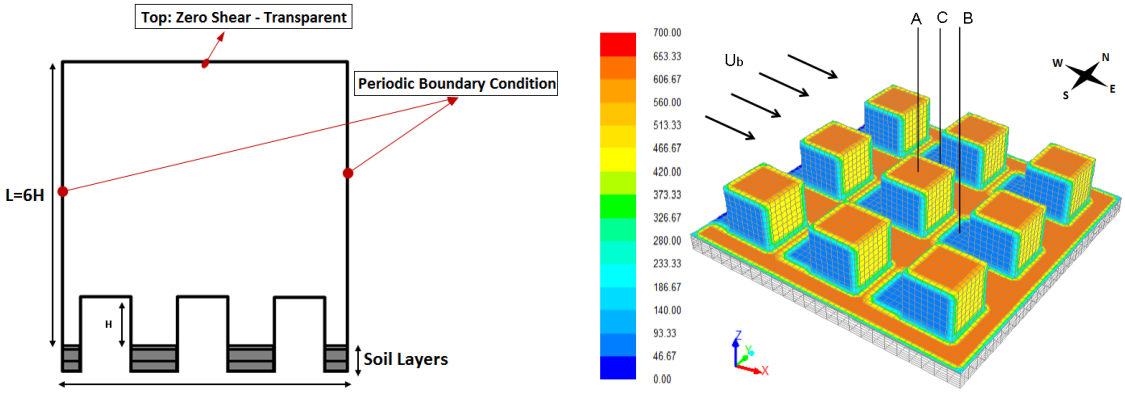

Figure 3.1: left: Cross section of the computational domain and boundary conditions. Right:Absorbed solar heat flux (S_{abs}) in W m^{-2} in the computational domain for canopy aspect ratio of 1 and ground surface albedo of 0.18 at 1500 LST on June 21st. Wind direction is aligned to the east-west canyon and A, B and C mark locations where the velocity profile is analyzed (described further in Figure 3.3-a).

In the present paper, CFD simulations of the urban environment are performed in an idealized 3D configuration. In order to accurately assess the effect of thermal

forcing on flow structure, dynamic coupling of the surface energy balance with the flow field inside the canyon is conducted (Section 4.2.1). Results are validated against field measurements at the Vancouver Light Industrial (LI) site [5] and compared with Town Energy Balance (TEB) and energy balance model of Krayenhoff et al [24] as shown in section 3.3. The magnitude and time of urban facet peak temperature is critical in the studies of Urban Heat Islands, building energy use and dwellers health and comfort. Therefore, diurnal variation of surface temperatures is analyzed as influenced by various factors. In order to have a realistic representation of thermal forcing in urban environments, solar radiation as well as inter-building longwave radiative exchange are considered as the main causes of non-uniform surface heating (section 3.4.1). Material properties constitute an important option for surface controls in urban environments. Urbanization introduces materials that differ significantly in their thermal and radiative properties when compared to natural land cover [31]. Therefore, flow over ground materials with different albedos is simulated (3.4.2). Since urban temperatures and fluid flow correlate strongly with the urban morphology and canyon geometry, the canyon Aspect Ratio (AR) is studied as a physical design parameter that exerts control over radiation access and convection from urban surfaces (3.4.3). Additionally, the effect of local weather condition is considered by analyzing the effect of wind speed and direction on temperature distributions as discussed in section 3.4.4. Conclusions are presented in section 3.5.

3.2 Model Description

Turbulence modeling and heat transfer calculations are performed by means of the unstructured finite volume solver ANSYS FLUENT 14.5. The flow passes

over a matrix of 3x3 equally spaced cubes placed on a flat wall boundary situated above multi-layer solid zones representing ground surface and soil layers (Figure 3.1). The height of the computational domain is 6H and a zero shear velocity condition is applied at the domain top. In order to achieve a fully-developed flow field, periodic boundary conditions are used in both stream and span-wise directions, creating infinite columns and rows of buildings. In the stream-wise direction, the mass flow rate is specified. The mass flow rate is determined assuming that the Typical Meteorological Year (TMY3) wind speed is valid at 2H and the velocity profile in [32] is used for vertical extrapolation. The TMY3 data is obtained from a representative coastal urban weather station in southern California (San Diego Miramar NAS, 32°867′ N, 117°133′ W). The Reynolds Averaged Navier Stokes (RANS) equations are solved and for turbulence modeling, k-epsilon Realizable model [33] is used with Standard Wall Function for near wall treatments [34].

The surface energy balance consisting of longwave (L) and shortwave (S) radiation, conduction (Q_c) and convection (Q_h) heat flux is as Eq 3.1 and latent heat flux is neglected. Equation 3.2 and 3.3 are used to calculate radiation flux components on urban surfaces.

$$(1-\alpha)S\downarrow - L = Q_c + Q_h \tag{3.1}$$

$$L_{gr} = \epsilon[\sigma T_{gr}^4 - L_{inc,gr}] \tag{3.2}$$

$$L_{inc,gr} = (F_{sky-gr})\sigma T_{sky}^4 + L_{w-gr} \tag{3.3}$$

Reynolds analogy between momentum and heat transport and the wall function

Table 3.1: Thermal and radiative properties of building walls, roof and different ground materials. For wall and rood surfaces, effective thermal conductivity and heat capacity are calculated based on multi-layered material properties as in [25].

	Thickness (m)	Effective thermal conductivity (W m^{-1} K^{-1})	Emissivity -	Albedo -	Effective heat capacity (MJ m^{-3} K^{-1})
Roof	0.234	0.043	0.92	0.15	0.182
Wall	0.113	0.045	0.88	0.30	0.187
Asphalt	1.370	0.740	0.95	0.18	1.940
Concrete	1.370	0.930	0.90	0.35	2.280

by Launder and Spalding [34] (see Appendix A for details) is used to calculate sensible heat flux from the surfaces and consequently Convective Heat Transfer Coefficients (CHTCs).[1] Buoyancy effects are considered and the Boussinesq approximation is used for density.

Asphalt and concrete ground surface material were simulated, since they are two of the most frequently used surfaces with similar thermal properties but significantly different albedo (see results in section 3.4.2). The soil layer depth is chosen to be several diurnal thermal damping depths and material properties of ground and wall surfaces are as in [25]. Thermal and radiative properties of all surfaces are shown in Table 3.1. The temperature boundary conditions inside the buildings and at the base of the deepest soil sublayer (exterior surfaces of computational domain) are set to be constant (295 K). Since wall and roof thermal thicknesses are small relative to the ground, they are not resolved by the grid; instead the 1D steady heat conduction equation is used to calculate the external surface temperature.

The inflow air temperature is set to the hourly average June air temperature from the TMY3 weather forcing data. Large convective heat transfer, the recirculating

[1]Since FLUENT does not output the convective fluxes explicitly, they were obtained from Eq 3.1 and net shortwave, longwave, and conduction heat flux as output by FLUENT.

flow, and the small domain height would lead to an unphysical air temperature increase. Therefore, to maintain a realistic air temperature the inflow boundary condition is a homogeneous air temperature that follow the TMY3 diurnal cycle, i.e. $T(x = 1, y, z, t) = T_{TMY}(t)$. An effort was made to set a more realistic temperature profile at the inlet with an average vertical temperature profile of $T_a(z)$, however with periodic boundary conditions FLUENT only permits homogeneous temperatures at the inlet.

The coupling of convection, conduction, and radiation is taken into account by simultaneously solving the energy equation and Discrete Ordinate non-gray radiation model [35] in the fluid domain. The top of the domain is set to radiate downwards at a sky temperature of 255 K to simulate longwave radiative interactions expected for clear sky conditions. Solar radiation was not taken from TMY3 but rather calculated using the ANSYS Solar Load Model for June 21st and solar noon was approximately at 1150 LST. The solar ray tracing algorithm (SRTA) takes a beam of direct radiation in the direction of the sun position vector, applies it to opaque surfaces and performs a face-by-face shading analysis to determine shadows. The total reflected solar irradiation is distributed among all surfaces weighted by area depending on the scattering fraction (set to 1 in this study). The Solar Load Model also accounts for isotropic diffuse radiation [36] based on the approach suggested in the 2001 ASHRAE Fundamentals Handbook [37] (Chapter 20, Fenestration). Appendix B details the solar load model used in ANSYS FLUENT 14.5.

Table 3.2 summarizes the cases investigated in the present paper. All computations are performed with the pressure-based solver, first order implicit transient formulation, PRESTO! for pressure discretization and the SIMPLE scheme for pressure-

velocity coupling (see [36] and the reference cited, therein, for more details on these schemes). The 3D structured grids are built with ANSYS 14.5. The size of the domain is $6H \times 6H \times 6H$ on top of the solid soil layers of depth 1.4 meters. 8 nodes per cube root of building dimensions are used and the grid resolution is stretched away from the building walls. The expansion ratio between two consecutive cells is kept below 1.2 as recommended by Franke et al [38]. Additionally, the mesh configuration is in compliance with the recommendation of a structured, hexahedral mesh with high quality of the grid. The specification of the appropriate grid depends heavily on the choice of the turbulence model and the corresponding wall function. With the Standard wall function approach used in this practice [34], for the logarithmic profile to be valid, the first computational node should be placed at a non-dimensional wall distance of z^+ between 30 and 500 for smooth walls ([36, 38]). The maximum local z^+ number in our simulation is approximately 350, which is in agreement with the criteria. Grid sensitivity is investigated by repeating the base case simulation with coarser grids (28000 instead of 110300 cells) which resulted in less than 1% difference in surface temperatures. Therefore the presented grid configuration is used. The time step size is 0.1s as dictated by stability and accuracy criteria. Simulations are initialized at 0001 LST and solar, temperature, and wind boundary conditions are updated every 5 minutes. FLUENT applies the energy equation to determine the initial surface (ground, roof and wall) temperatures resulting in lower initial temperature than the inlet air temperature. Surface temperatures and energy balance components are output every 5 mins and averaged over the computational nodes weighted by the area in each surface.

Table 3.2: List of simulations performed and their specifications. Case #1 represents the base case of this study and the difference of each case is shown in bold.

Case Name	Ground surface $-$	AR=H/W $(-)$	Wind Speed (ms^{-1})	Wind Direction degree
Base	Asphalt	1	2	0
Gr-C	**Concrete**	1	2	0
AR-L1	Asphalt	**1/3**	2	0
AR-L2	Asphalt	**2/3**	2	0
AR-H	Asphalt	**3/2**	2	0
θ-45	Asphalt	1	2	**45**
θ-90	Asphalt	1	2	**90**
U_b-3	Asphalt	1	**3**	0

3.3 Validation

The diurnal variation of surface temperatures is validated against field measurements at the Vancouver Light Industrial (LI) site, and compared with Town Energy Balance (TEB) and 3D energy balance (TUF3D) model as presented in Krayenhoff et al [24]. The site mainly consist of one to three story buildings representing a high density configuration with distinct lack of vegetation (vegetated fraction $< 5\%$). Experimental data are gathered with helicopter and truck mounted thermal remote sensors on a clear day. The diurnal variation of wind speed and direction are shown in figure 3.2 and further details are available in Voogt and Grimmond [5]. Validation case is simulated over an idealized matrix of $3\times$ 3 buildings with periodic boundary conditions and the input parameters from Table 2 in Krayenhoff et al [24].

The calculated temperature at ground and roof surfaces are within the range of reported experimental data by Voogt and Grimmond [5] as shown in Figure 3.2. In comparison with TUF3D and TEB models, there is a lag observed in the increase of ground temperature in the morning hours. This can be explained in two ways. One restriction that is imposed for periodic boundary conditions in FLUENT is the

requirement to use the same temperature boundary condition (here 295 K) at all exterior surfaces of the computational domain, which applies to deep soil (ground) and internal (roofs and walls) surface temperature. This difference in specifications compared to [24] resulted in larger conduction heat flux to the soil layers throughout the day (see Figure 3.5-a in section 3.4.1) and consequently a delay in ground surface temperature cooling in the evening compared to TEB and TUF3D models. On the other hand FLUENT is expected to be superior in its representation of fluid flow and convection. Therefore, it is expected that the convective heat transfer estimated in TEB and TUF3D using empirical heat transfer coefficient correlations results in biased higher surface temperature. For the roof, the calculated temperature in our model is in better agreement with the experiment while exhibiting more sensitivity to wind speed variation and solar radiation compared to TEB and TUF3D. [24] discrectized the roof thickness before applying a finite difference scheme; therefore the associated thermal inertia of roofs explains the smaller sensitivity of roof temperature to solar radiation compared to our simplified assumption.

3.4 Results

3.4.1 Diurnal Variation of Urban Temperature and Energy Balance Components

In order to analyze the effect of the flow field on temperature and surface energy balance components, vertical profiles of stream-wise velocity are shown in Figure 3.3-b. The velocity profile at the center line downwind of the center building demonstrates the canyon vortex formation in this region. The stream-wise velocity is

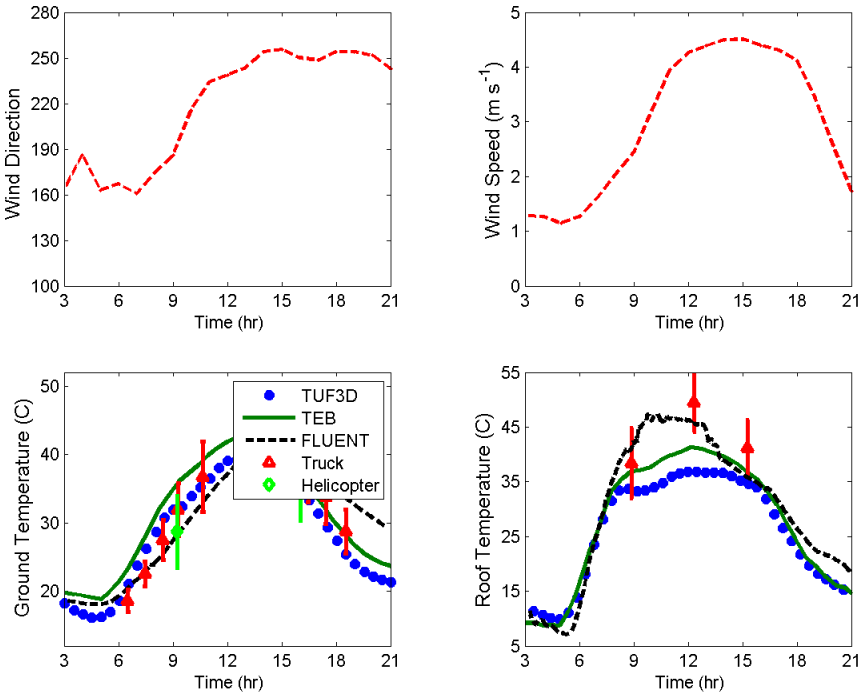

Figure 3.2: Validation of diurnal evolution of ground and roof temperatures (abbreviated as NK2014) against remotely sensed surface temperature measurements at the Vancouver Light Industrial (LI) site on August 15, 1992. Town Energy Balance and Temperature of Urban Facets are extracted from [24] and abbreviated as TEB and TUF3D, respectively. Wind speed and direction of the observation period is also included. For more details refer to Voogt and Grimmond [5].

negative inside the canyon and strong shear is evident near the roof level. The profile converges to the upstream wind velocity above the buildings.

Figure 3.4-a presents the diurnal cycle of temperatures of walls, roof, and ground as area-weighted averages over the computational nodes in each surface. The air temperature that is prescribed at the inlet (T_a) is also shown. T_w is the average temperature of all four walls of a building, each of which undergoes a very different diurnal cycle according to their orientation relative to the sun position and inter-building longwave interactions. These diurnal cycles are shown in Figure 3.4-b. The largest temperaturse of the urban surfaces on this day are 335 K for the roof (1200 LST), 328 K for the ground (asphalt) (1430 LST), and 311 K for the building wall

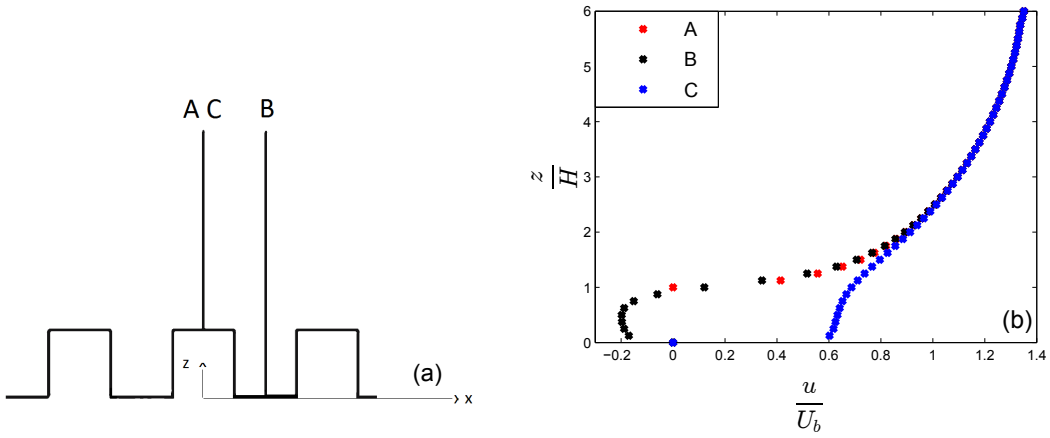

Figure 3.3: a) Geometrical configuration: X-Z view at plane Y/H=0 with locations where vertical profiles are studied. A: Above center building X/H=0, Y/H=0, B: Downwind halfway between buildings X/H=1, Y/H=0, C: Center-line street canyon X/H=0, Y/H=1, b) vertical profiles of stream-wise velocity at different locations at 1200 LST with asphalt as ground surface material and aspect ratio of 1. See Figure 3.1 for a 3D visualization of locations A, B and C in the computational domain.

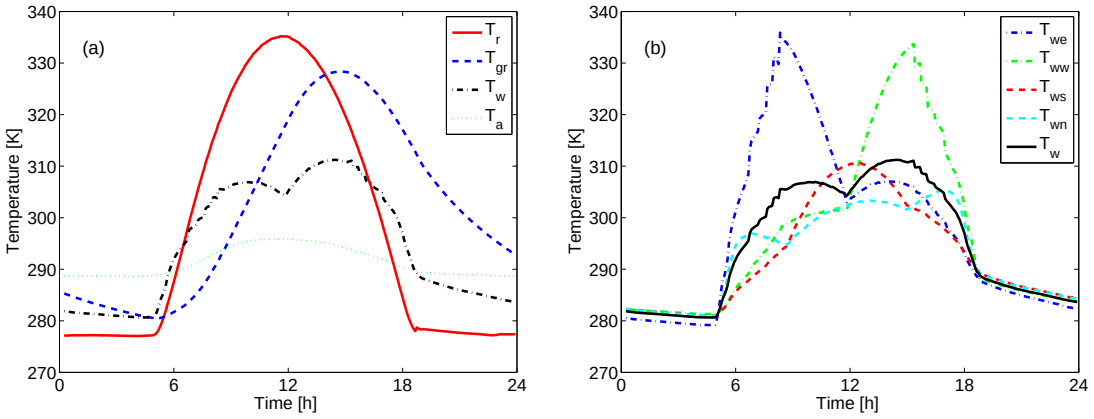

Figure 3.4: Diurnal temperature variations of a) urban surfaces and air and b) walls for different aspects for asphalt as ground surface material and AR=1.

(1400 LST). The large heat capacity in the thermally massive soil layers caused the delay in maximum ground surface temperature from solar noon, when the maximum of solar irradiation occurs.

Because of the high density of buildings for AR=1, shadowing caused the average ground temperature to be smaller than the roof temperature. For building walls, in addition to shadowing that always affects at least two wall orientations, due to the vertical orientation of wall surfaces compared to large solar altitude angles during midday, the solar radiation fluxes are reduced and building wall surfaces are cooler. Even though the solar insolation is symmetric about 1150 LST, the average wall temperature is larger in the afternoon compared to the morning due to increasing ground surface temperature (thus increasing ground-building longwave radiation as shown in Figure 3.5-b). Likewise the increasing longwave radiative exchange causes the walls opposite the most directly insolated walls to be warmer than other shaded walls (e.g. west-facing wall in the morning warmer than north- and south-facing wall).

Figure 3.5-a shows the different heat flux components at the ground surface for asphalt. As a result of the cool ground surface, stable atmospheric stratification exists until about 0800 LST and due to the high urban density (AR=1), the flow velocity in between buildings is small. Therefore, the sensible heat flux is small and negative. Instead the net radiation surplus decrease the ground temperature.

The large thermal heat capacity and associated inertia of the soil layers, in addition to the restriction on deep soil surface temperature as described in section 3.3, causes the conduction heat flux to be the dominant mean of heat removal in the morning and early afternoon and the dominant mean of heat generation in the evening. However, at 1430 LST (when the maximum ground temperature occurs) the longwave

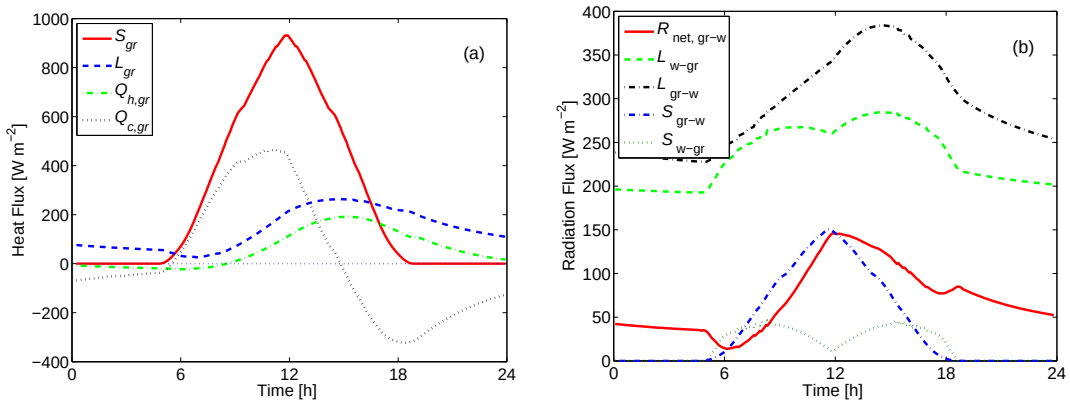

Figure 3.5: For asphalt as ground surface material and AR = 1: a) ground surface energy balance components, where S_{gr} and L_{gr} are net shortwave and longwave and b) Longwave and shortwave radiation exchange between ground and wall surfaces. Incident longwave to the ground consists of incident radiation from the sky (radiating at the sky temperature) and longwave radiation from building walls (L_{w-gr}) according to Equations 3.2- 3.3. $S_{\mathrm{gr-w}}$ is the upward shortwave radiation from the ground surface which is the product of view factor, incident shortwave radiation on the surface (S), and its albedo (α_{gr}). Similarly $S_{\mathrm{w-gr}}$ and $L_{\mathrm{w-gr}}$ are the shortwave and net longwave radiation from wall to ground. $R_{\mathrm{net,gr-w}}$ is the net all-wavelength radiation between wall and ground.

radiation flux is the largest loss component. As expected, the maximum sensible heat flux and radiation heat flux coincide with the maximum ground temperature.

Figure 3.5-b shows the longwave and shortwave radiation exchange between ground and wall surfaces. Due to asphalt's small albedo, $S_{\mathrm{up,gr}}$ is significantly smaller than longwave radiation components between ground and wall surfaces, demonstrating the effect of surface radiative properties on urban facade temperatures.

Since longwave radiation variability is solely due to surface temperature, $L_{\mathrm{gr-w}}$ and $L_{\mathrm{w-gr}}$ in Figure 3.5-b have similar patterns as ground and wall temperature, respectively. $L_{\mathrm{w-gr}}$ has a local minimum around noon, when the sun is close to zenith and the shortwave radiation intensity is reduced, and two local maxima at 0900 LST and 1430 LST due to the large insolation received by the east and west wall at these times, respectively.

The decrease in $R_{\mathrm{net,w-gr}}$ from 0530-0800 LST can be explained by the increase

in shortwave radiation incident on building walls in the morning and the resulting increase in $S_{\mathrm{w-gr}}$, wall temperature, and consequently $L_{\mathrm{w-gr}}$. Similarly, the increase in $R_{\mathrm{net,w-gr}}$ from 1730-1900 LST is due to the larger rate of change in solar radiation on walls compared to ground near sunset. This also leads to a decrease in $L_{\mathrm{w-gr}}$ after sunset.

3.4.2 Effect of Ground Surface Albedo

The effects of radiative properties of the ground surface on heat fluxes and urban surface temperature is studied by comparing the results for asphalt and concrete as ground surface material. Since the impact of canyon aspect ratio (H/W= 1.0 in our simulation) is less significant around midday when sun is close to zenith, the sensitivity of peak surface temperatures to the ground albedo is also compared with the $H/W = 0.36$ simulation in [25].

During the daytime the average ground temperature of concrete is significantly lower than that of asphalt as a result of the larger albedo. The maximum ground temperature decreases 8 K relative to asphalt, which is a 2.5% decrease for a 0.17 increase in albedo (Figure 3.6-a). This is in agreement with the results reported by [25], where the peak temperature difference was approximately 2.0%. The effect of ground radiative properties can also be observed in the wall temperatures presented in Figure 3.6-b. While the diurnal pattern is similar, the larger upward shortwave radiation from ground to wall surfaces caused the wall temperature over concrete surfaces to be 3.5 K (1.1%) larger than that of asphalt. The wall temperature in [25] shows lower sensitivity to ground albedo due to the difference in wall conduction modeling since we do not resolve wall thickness.

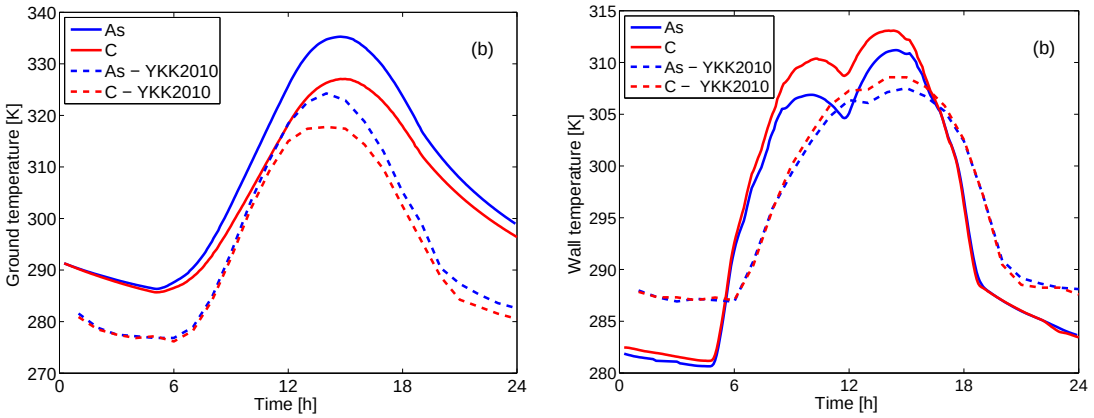

Figure 3.6: Comparison of urban surface temperatures for a) ground and b) wall (averaged) with different ground surfaces (Table 3.1) and AR=1. For reference, simulation results from Yaghoobian et al. (2010) are shown where H/W=0.36.

As described in section 3.4.1 (Figure 3.5-b), $R_{\text{net,w}-\text{gr}}$ is correlated to $S_{\text{up,gr}}$ and therefore ground surface albedo. The simulation results for different ground surface material demonstrates the strong interaction between ground surface materials and urban facade temperature, consistent with Yaghoobian and Kleissl (2012) [26]. In [26] impacts on building energy use were also demonstrated.

3.4.3 Effect of Canyon Aspect Ratio

In order to study the effect of urban built-up density on the urban energy balance and surface temperatures, we conducted a sensitivity analysis on canyon aspect ratio (AR). We focused on 4 cases of AR (=H/W) from 1/3 to 3/2 and the ground-wall view factors for each case are shown in Table 3.3. Canyon aspect ratio is modified by keeping building height (H) constant and changing building spacing (W).

Aspect ratio (AR) determine the penetration of direct solar radiation to the street canyon. Figure 3.7-a compares total shortwave radiation incident on the ground

Table 3.3: Ground-wall view factor with different canyon aspect ratios. The ground-sky view factor is 1 minus the value in the table.

AR=H/W	1/3	2/3	1	3/2
F_{gr-w}	0.20	0.34	0.45	0.56

surface at different ARs. S decreases with increasing AR, but the diurnal variation between ARs is dynamic. Differences in incident shortwave radiation are small before 0730 LST when the sun elevation is low, and solar beams are being mostly blocked by the buildings even in low density cases (tan solar altitude $\approx 2/3$ at 0730 LST). Between 0730 until 0900 LST the fraction of unshaded area increases more rapidly for smaller AR($=H/W$) and the absolute insolation differences increases rapidly in this period. However, after 0900 LST the shading difference decreases and reaches a local minimum at solar noon.

A similar, but more pronounced difference is observed for wall surfaces as shown in Figure 3.8-a and is expected since the clearing of building shadows from sun-facing wall surfaces precedes the widespread direct insolation of ground surfaces. Without surrounding buildings and atmosphere, the peak S would occur for perpendicular incidence at sunrise. For small canyon aspect ratio (AR) negligible wall shadowing occurs and maximum wall S happens early in the morning and later in the afternoon (time of maximum temperature at east and west walls in Figure 3.4-b). With increasing AR, shadowing of wall and ground surfaces increases. Consequently, direct shortwave radiation that is received by all walls and diffuse radiation reflected from the ground decrease causing maximum shortwave radiation to move closer to solar noon.

Canyon aspect ratio alters the flow structure and wind sheltering inside the canyon, therefore affecting convective heat transfer. Comparison of ground sensible heat flux at different AR ($=H/W$) is shown in Figure 3.7-b. For larger ARs, wind

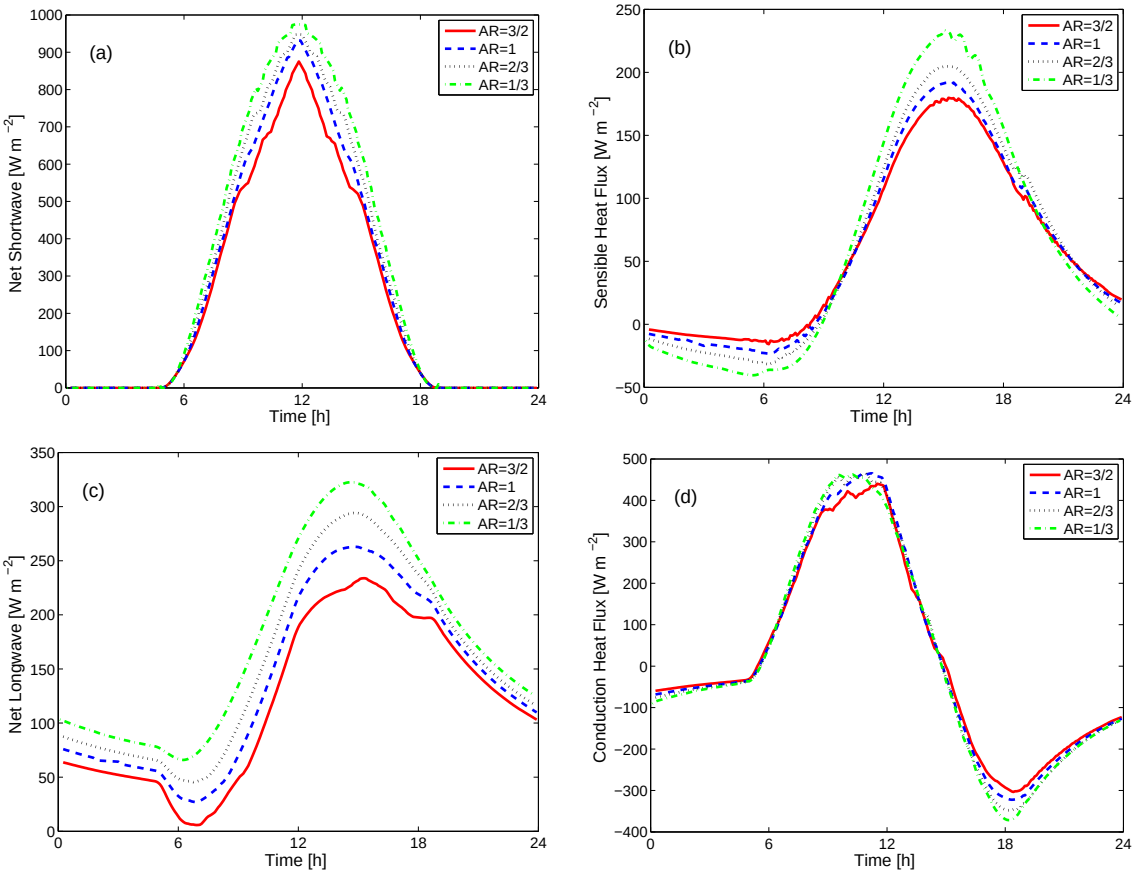

Figure 3.7: a) Net shortwave radiation, b) sensible, c) net longwave radiation and d) conduction heat flux in W m^{-2} of ground surface area for different aspect ratios and asphalt as ground material.

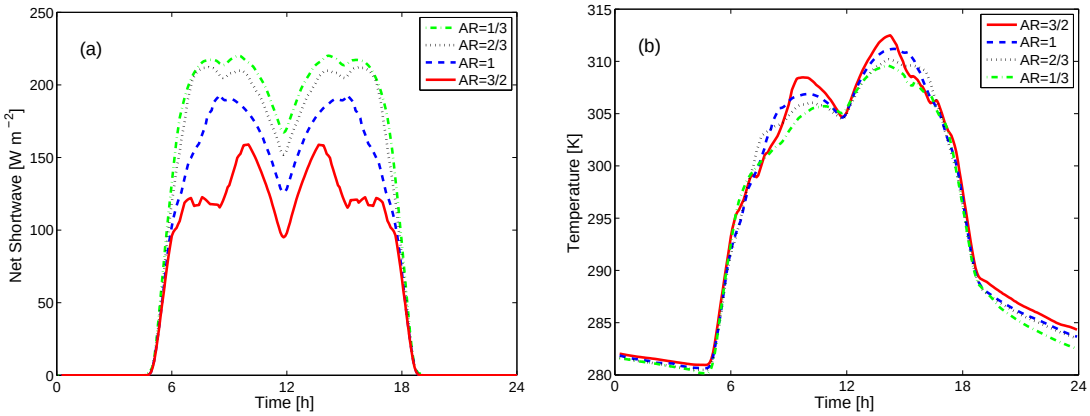

Figure 3.8: a) Net shortwave radiation flux at wall surfaces, b) Average wall temperature for different aspect ratios and asphalt as ground material.

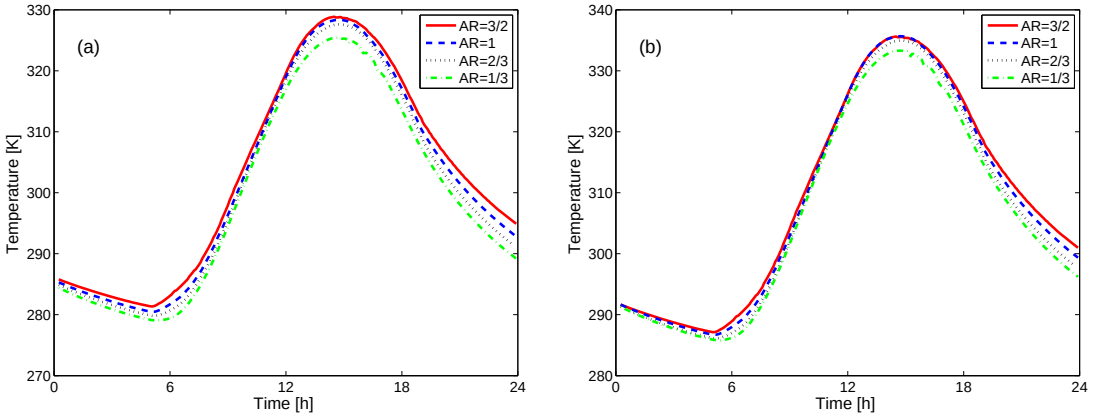

Figure 3.9: a) Ground temperature at different aspect ratios and asphalt as ground material b) Ground temperature normalized by ground surface initial temperature and multiplied by daily average air temperature at the inlet.

sheltering and vortex formation between buildings causes smaller velocities in the building canyon, decreasing the magnitude of CHTCs. As a result, the magnitude of ground sensible heat flux decreases with an increase in H/W (approximately 22% decrease in maximum Q_h from AR=1/3 to AR=3/2); causing less surface heating from air-to-ground at night and less surface cooling during the day. Aspect ratio (AR) variation affects sensible heat flux at wall surfaces similarly as at ground surfaces (not shown).

Longwave radiation is also affected by AR (Figure 3.7-c). The decrease in net longwave radiation from 0530-0800 (Figure 3.7-c) is due to shortwave radiation normally incident on building walls in the morning, increasing wall temperature and longwave radiation from wall to ground. This behavior is more expressed for AR=3/2 since the ground-wall view factor increases such that the larger wall temperature have more impact on ground temperature. Increasing H/W causes an increase in average ground-wall view factor (Table 3.3), increasing daytime incident longwave and decreasing net longwave radiation, L, on wall surfaces (given the sign convention in Equation 3.2). However, convection from wall surfaces is the largest term balancing

net radiation (shortwave plus longwave). Therefore, after the complete wall surface starts to receive direct solar irradiation, the average wall temperature increases with H/W as shown in Figure 3.8-b. This resulted in larger longwave radiation from wall to ground with increasing AR.

For ground surfaces, Figure 3.9-a demonstrates that for larger AR($=H/W$) despite the reduction in net shortwave radiation, the daytime temperature increased. The temperature difference between AR=1/3 and AR=3/2 is larger at night than during the day. To quantify the difference we should consider that due to the numerical method different initial ground temperatures were observed (see last paragraph of section 3.2). While this initial difference cannot strictly be normalized out due to non-linear interactions during the day, for a more representative comparison, the ground temperature throughout the day is normalized with the initial ground temperature and then multiplied by the daily average air temperature at the inlet. The resulting Figure 3.9-b better characterized the effect of aspect ratio. The difference between ground temperature at H/W of 3/2 and 1/3 is approximately 4 K at midnight (2359 LST).

3.4.4 Effect of Wind Direction and Speed

Most studies on flow field and heat transfer of street-like environments are conducted for cases in which the incoming wind is aligned with the street direction, that is just one realization of variable wind directions observed in urban areas. Velocity profiles and surface drag generated by the wind at different angles differs from the case with wind aligned to the street direction. To further address the effect of geometrical characteristics of urban areas on surface temperatures and energy balance components,

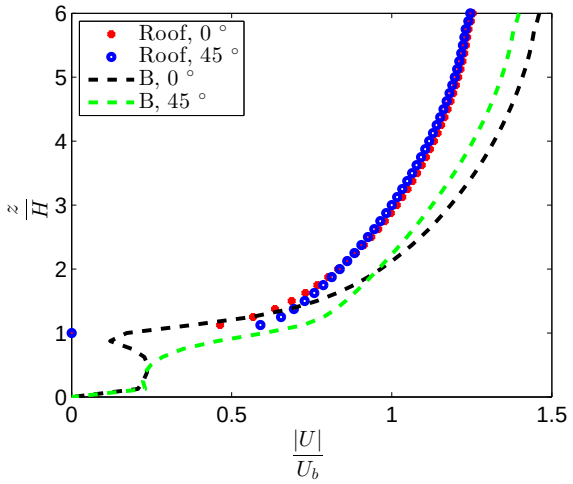

Figure 3.10: [Vertical profile of velocity magnitude at different locations and wind direction at 1200 LST for flow over asphalt and aspect ratio of 1. See Figure 3.3 for the location B in the domain.

cases with wind parallel to the building diagonal and north-south street direction (45 and 90 degree wind angle from east-west, respectively, shown in Figure 3.1) are simulated with H/W=1 and asphalt as ground material.

Figure 3.10 shows vertical profiles of wind speed above the center building averaged over the roof surface and at the centerline between the buildings (B in Figure 3.3) for $\theta = 0°$ and 45° (the wind speed profile of $\theta = 90°$ is essentially identical to $\theta = 0°$). Note that the simulations were setup to have the same bulk velocity of 2 m s^{-1}, consistent with the other simulations presented so far. The magnitude of the velocity at $\theta = 45°$ is larger at roof level and in the upper half of the canyon, but becomes smaller than for $\theta = 0°$ as z increases. The reduction in velocity just below roof height for $\theta = 0°$ is a result of stronger flow separation in the building lee manifested in canyon vortices and associated shear. The increase in the effective building spacing in the flow direction for $\theta = 45°$ likely also decreases surface drag as the flow type transitions from skimming flow to wake interface [39].

Figure 3.11 shows the diurnal variation of ground, roof and wall temperatures in comparison with the reference case (AR=1, asphalt, $\theta = 0°$). It can be seen that the effect of wind angle on roof and wall surfaces is more pronounced than on ground surfaces (all data are normalized to remove the difference in initial condition as in Figure 3.9-b). The roof temperature for the building under 45 degree wind angle decreased approximately 2.5 K ($\approx 1\%$) at solar noon which is due to the increase in velocity and consequently sensible heat flux at roof level. However, as observed in 3D vector plots (not shown), at the same time the velocity magnitude adjacent to wall surfaces decreased and caused the averaged wall temperature to be larger for $\theta = 45°$.

At the ground surface, the magnitude of sensible heat flux decreased at night for $\theta = 45°$ by about 10% (not shown). The sensible heat flux difference decreases in daytime, but is generally negligible since the velocity magnitude is small for both cases due to the high urban density (AR=1). Consequently the ground temperature was not influenced by wind angle.

At $\theta = 90°$ ground and roof temperatures are not affected, as expected from the symmetry in geometry. For wall temperature, the east wall experiences the largest decrease in temperature from 0600 LST to 1100 LST in comparison with $\theta = 0°$. For $\theta = 0°$, in the morning thermal forcing is in opposite direction from the mechanically induced canyon vortex which further decreases the already small velocity in the east-west (streamwise) canyon. At $\theta = 90°$, however, the wind direction is aligned with the east wall which causes the velocity adjacent to these surfaces and consequently the sensible heat flux to increase (see B versus C in Figure 3.3-b). After 1200 LST wall temperatures are more homogeneous with aspect and are more strongly influenced by the ground-wall longwave flux (Figure 3.5-b) which results in the difference in local

wind speed and convection being less important. Consequently, the afternoonf average wall temperature is similar in all three cases.

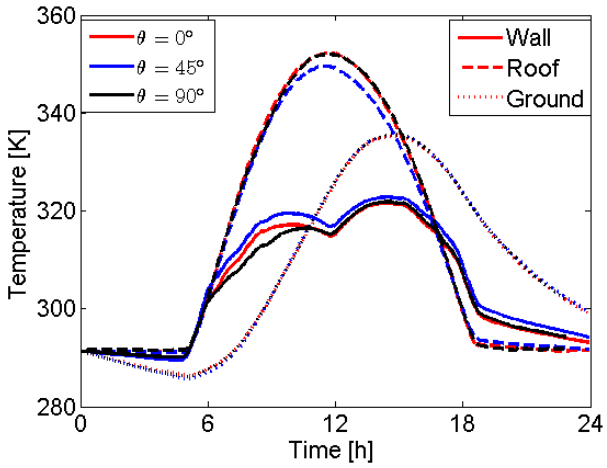

Figure 3.11: Comparison of diurnal urban surface temperatures for different wind direction for flow over asphalt and AR=1. Similarly as in Fig. 3.9-b, surface temperatures are normalized by the initial temperature and multiplied by daily average air temperature at the inlet. Line styles indicate the surface and colors show the wind direction relative to the east-west direction..

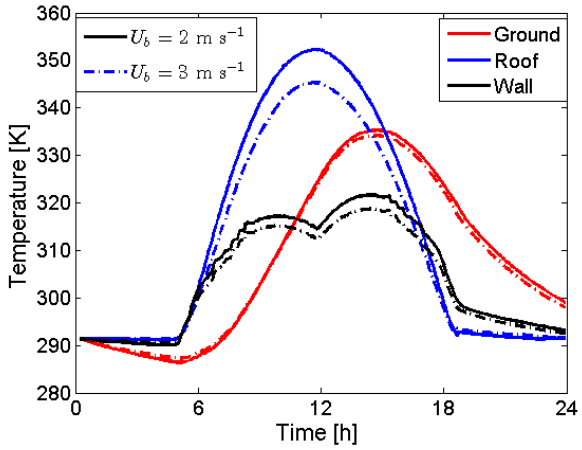

Figure 3.12: Comparison of diurnal urban surface temperatures for different wind speeds for flow over asphalt and AR=1. Surface temperatures are normalized by the initial temperature and multiplied by daily averaged air temperature at the inlet. Line styles indicate the wind speed and colors show the studied surface.

To study the effect of free-stream wind speed, we repeated the calculation with bulk inlet wind velocity of 3 m s^{-1} (Figure 3.12). Wind speed only influence the

ground temperature mostly at night (up to 1 K at 2359 LST). A larger wind speed results in more convective heat transfer from the air to the ground, heating the ground from 0000 to 0700 LST. However, due to the high aspect ratio, the wind speed near the ground is less dependent on bulk wind speed and during daytime, with the increase in the magnitude of S, net radiation dominates over convection, resulting in ground temperature not being sensitive to wind speed. The amplitude of roof temperature is significantly influenced by the bulk velocity (2% decrease) due to the increase in convective flux from the roof.

3.4.5 Summary

Table 3.4 summarizes and compares the effect of the studied parameters on different urban surface temperatures. The choice of parameter values was somewhat subjective and the observed non-linearities make it difficult to assign sensitivities to each parameter. However, the parameters present commonly observed variations in urban and meteorological conditions and provide some insight into the relative importance of each design variable. The ground surface material (albedo) is shown to have the most significant effect on surface temperature. While from a UHI mitigation standpoint the decrease in ground surface temperature is desirable, it also results in higher wall temperature, subsequently increasing the heat transfer through the building envelope. As discussed in section 3.4.3, despite the reduction of solar penetration to street canyons, the increase in canyon aspect ratio increases urban surface temperature collectively, due to the reduction of convective heat transfer and wall-to-ground view factor. As expected, the effect of urban built-up density and ground surface albedo on roof temperature are insignificant since the only mechanism is indirectly through

Table 3.4: Summary of (daytime) peak temperature results at different urban surfaces. Case names are defined in Table 3.2 and the maximum temperature difference of each surface is compared to the Base Case. (-) represent temperature difference less than 0.5 K.

Case Name	$\Delta T_{\mathrm{w,max}}$ (K)	$\Delta T_{\mathrm{gr,max}}$ (K)	$\Delta T_{\mathrm{r,max}}$ (K)
Base	-	-	-
Gr-C	+ 2.0	- 8.0	-
AR-L1	- 1.4	-3.6	-
AR-L2	- 0.6	- 1.8	-
AR-H	+ 2.6	+ 0.6	-
θ-45	+ 2.4	-	- 2.6
θ-90	- 3.0	-	-
U_b-3	- 1.2	- 2.9	- 6.9

air at roof level. Local wind speed and direction, on the other hand, strongly affect convective heat transfer from the roof. More interestingly, the alignment of heated street canyon with respect to the wind direction affects the wall temperature (more pronouncedly in the morning hours), and therefore the air conditioning energy use by the building (case #7). Additionally, in a high canyon built-up density the effects of wind speed and direction on the ground temperature are less significant.

3.5 Conclusions

CFD simulations of the urban environment are performed to investigate the relative importance of various design parameters including geometrical characteristic and surface albedo, as well as local weather conditions, on urban facet temperature and energy balance. Simulations are performed for a clear summer day which exhibits the strongest solar forcing and therefore present the most expressed differences in surface temperature variability and sensitivity at the coastal site at a latitude of 33 °. An idealized configuration of buildings is considered. The range of built-up density analyzed falls between open low-rise to compact mid-rise urban zones as classified by

Stewart and Oke [40]. A realistic representation of three-dimensional thermal forcing is achieved by considering the inter-building and ground shadowing. The diurnal variation of urban surface temperatures and heat fluxes are analyzed.

As also highlighted by Yaghoobian and Kleissl (2012) [26], our results demonstrate a strong interaction between urban surface temperatures and ground surface materials as well as canopy height-to-width ratio. As the main cause of the urban heat island is the modification of the land surface by urban development [41], it is of great importance to analyze impacts of urban materials that are engineered to reverse urban heat island effects. Sensitivity of the results to ground surface albedo (represented by asphalt and concrete) is investigated and found to have the most influence among studied parameters. The substantial reduction in shortwave radiation reflected from ground results in significantly lower ground temperature and higher wall temperatures. The increase in wall temperature directly affects air temperature, UHI intensity and therefore the energy use since typically, electricity demand in cities increases by 2 to 4% for each 1°C increase in air temperature. Sensitivity analyses of aspect ratio shows that the ground and wall temperatures increase with increasing canopy height-to-width ratio. The ground and wall temperature difference for small versus large H/W is larger at night than during the day and is more apparent when the bulk wind speed is smaller. The effect of aspect ratio on the thermal environment and convection from urban surfaces is also tangible. In summary, land cover modification, larger aspect ratio, and smaller reflectance from ground surface, all are downfalls of urbanization and promote Urban Surface Temperature Heat Islands.

To further investigate the effect of geometrical characteristics of urban areas, different wind directions and speeds are simulated. For large canopy height-to-width

ratio wind speed near the ground is less dependent on bulk wind direction and speed, and ground temperature is mostly dependent on the amount of incident radiation and not bulk wind speed. For wall surfaces, we observe that only in the morning wind direction has a large effect on average wall temperature since wind speed at the heated (east) wall changes dramatically for along-wind versus cross-wind canyons. Consequently sensible heat flux from wall surfaces is affected as also demonstrated in [29]. However, during the rest of the day the heterogeneity in wall temperature is smaller and solar radiation and buoyant forcing become more dominant than momentum forcing, thus reducing the effect of the wall orientation and wind direction. For instance, the east wall is changed from a low-wind area in the lee of the building to having wind direction aligned to its surface on the sides of the streamwise canyon as the wind direction turns $\theta = 90°$. This affects the superposition of mechanical and thermal forcing and consequently sensible heat flux from wall surfaces. As expected, roof surface temperature responds most strongly to the bulk wind speed and angle.

This paper demonstrates the strong interaction between turbulent flow and thermal fields and the necessity of dynamic-coupling of these forcings in numerical simulations of the urban environments (as also investigated in [27],[28],[29]). On the other hand, modeling of the diurnal variation of direct shortwave radiation and the resulting non-uniform heating of urban surfaces yields more accurate of urban micro-climate analysis, and building energy load calculations.

The generality of geometry and mesh generation in a commercial CFD code simplifies the extension of the present simulations to more realistic urban settings in the future. However, the numerical model also imposes a variety of restrictions and requires larger computational resources than more specialized academic codes.

More accurate results of the urban flow could be achieved by utilizing more advanced turbulence representations such as Large Eddy Simulations. The correction of non-physical accumulation of heat in the periodic boundary conditions also requires further attention. This problem is commonly addressed through two approaches: 1) A constant temperature boundary condition at the top of the domain , 2) a constant inflow temperature boundary condition. Since we simulate a diurnal cycle the temperature boundary condition is slowly changing following the TMY3 air temperature. We apply (2) for computational simplicity, but at the cost of unphysical temperature fields downstream of the inlet. Further research is required to dynamically update the temperature at top or inlet boundary to achieve a desired setpoint temperature in the domain while allowing the flow and thermal field to evolve dynamically.

Acknowledgements

The text and data in chapter 3, in full, is a reprint of the material as it appears in "CFD simulation of an idealized urban environment: Thermal effects of geometrical characteristics and surface materials", Nazarian, Negin; Kleissl, Jan, *Urban Climate*, 12 (2015), 141-159. The dissertation author is the primary investigator and author of this article.

Bibliography

[1] Luke Howard. *The climate of London: deduced from meteorological observations made in the metropolis and at various places around it*, volume 2. Harvey and Darton, J. and A. Arch, Longman, Hatchard, S. Highley [and] R. Hunter, 1833.

[2] Tim R Oke. The energetic basis of the urban heat island. *Quarterly Journal of the Royal Meteorological Society*, 108(455):1–24, 1982.

[3] TR Oke, GT Johnson, DG Steyn, and ID Watson. Simulation of surface urban heat islands under idealconditions at night part 2: diagnosis of causation. *Boundary-Layer Meteorology*, 56(4):339–358, 1991.

[4] Y Nakamura and TR Oke. Wind, temperature and stability conditions in an east-west oriented urban canyon. *Atmospheric Environment (1967)*, 22(12):2691–2700, 1988.

[5] James A Voogt and CSB Grimmond. Modeling surface sensible heat flux using surface radiative temperatures in a simple urban area. *Journal of Applied Meteorology*, 39(10):1679–1699, 2000.

[6] M Kanda, M Kanega, T Kawai, R Moriwaki, and H Sugawara. Roughness lengths for momentum and heat derived from outdoor urban scale models. *Journal of Applied Meteorology and Climatology*, 46(7):1067–1079, 2007.

[7] K Niachou, I Livada, and M Santamouris. Experimental study of temperature and airflow distribution inside an urban street canyon during hot summer weather conditions. part ii: Airflow analysis. *Building and Environment*, 43(8):1393–1403, 2008.

[8] Mehdi Shahrestani, Runming Yao, Zhiwen Luo, Erdal Turkbeyler, and Hywel Davies. A field study of urban microclimates in london. *Renewable Energy*, 73:3–9, 2015.

[9] ER Meinders and K Hanjalić. Vortex structure and heat transfer in turbulent flow over a wall-mounted matrix of cubes. *International Journal of Heat and Fluid Flow*, 20(3):255–267, 1999.

[10] Kiyoshi Uehara, Shuzo Murakami, Susumu Oikawa, and Shinji Wakamatsu. Wind tunnel experiments on how thermal stratification affects flow in and above urban street canyons. *Atmospheric Environment*, 34(10):1553–1562, 2000.

[11] K Richards, M Schatzmann, and B Leitl. Wind tunnel experiments modelling the thermal effects within the vicinity of a single block building with leeward wall heating. *Journal of wind engineering and industrial aerodynamics*, 94(8):621–636, 2006.

[12] Jonas Allegrini, Viktor Dorer, and Jan Carmeliet. Wind tunnel measurements of buoyant flows in street canyons. *Building and Environment*, 59:315–326, 2013.

[13] Xiaomin Xie, Chun-Ho Liu, Dennis YC Leung, and Michael KH Leung. Characteristics of air exchange in a street canyon with ground heating. *Atmospheric Environment*, 40(33):6396–6409, 2006.

[14] Jose Luis Santiago, Alberto Martilli, and Fernando Martín. Cfd simulation of airflow over a regular array of cubes. part i: Three-dimensional simulation of the flow and validation with wind-tunnel measurements. *Boundary-layer meteorology*, 122(3):609–634, 2007.

[15] Marcus Oliver Letzel, Martina Krane, and Siegfried Raasch. High resolution urban large-eddy simulation studies from street canyon to neighbourhood scale. *Atmospheric Environment*, 42(38):8770–8784, 2008.

[16] Jong-Jin Baik, Jae-Jin Kim, and Harindra JS Fernando. A cfd model for simulating urban flow and dispersion. *Journal of Applied Meteorology*, 42(11):1636–1648, 2003.

[17] Zheng-Tong Xie and Ian P Castro. Large-eddy simulation for flow and dispersion in urban streets. *Atmospheric Environment*, 43(13):2174–2185, 2009.

[18] DA Philips, R Rossi, and G Iaccarino. Large-eddy simulation of passive scalar dispersion in an urban-like canopy. *Journal of Fluid Mechanics*, 723:404–428, 2013.

[19] Y Cheng, FS Lien, E Yee, and R Sinclair. A comparison of large eddy simulations with a standard k–ε reynolds-averaged navier–stokes model for the prediction of a fully developed turbulent flow over a matrix of cubes. *Journal of Wind Engineering and Industrial Aerodynamics*, 91(11):1301–1328, 2003.

[20] Zheng-Tong Xie and Ian P Castro. Efficient generation of inflow conditions for large eddy simulation of street-scale flows. *Flow, turbulence and combustion*, 81(3):449–470, 2008.

[21] Yoshihide Tominaga and Ted Stathopoulos. Cfd modeling of pollution dispersion in a street canyon: Comparison between les and rans. *Journal of Wind Engineering and Industrial Aerodynamics*, 99(4):340–348, 2011.

[22] Xian-Xiang Li, Chun-Ho Liu, Dennis YC Leung, and KM Lam. Recent progress in cfd modelling of wind field and pollutant transport in street canyons. *Atmospheric Environment*, 40(29):5640–5658, 2006.

[23] Haider Taha, Hashem Akbari, Arthur Rosenfeld, and Joe Huang. Residential cooling loads and the urban heat islandthe effects of albedo. *Building and Environment*, 23(4):271–283, 1988.

[24] E Scott Krayenhoff and James A Voogt. A microscale three-dimensional urban energy balance model for studying surface temperatures. *Boundary-Layer Meteorology*, 123(3):433–461, 2007.

[25] Neda Yaghoobian, Jan Kleissl, and E Scott Krayenhoff. Modeling the thermal effects of artificial turf on the urban environment. *Journal of Applied Meteorology and Climatology*, 49(3):332–345, 2010.

[26] Neda Yaghoobian and Jan Kleissl. Effect of reflective pavements on building energy use. *Urban Climate*, 2:25–42, 2012.

[27] Bojan Ničeno, ADT Dronkers, and Kemal Hanjalić. Turbulent heat transfer from a multi-layered wall-mounted cube matrix: a large eddy simulation. *International journal of heat and fluid flow*, 23(2):173–185, 2002.

[28] Xian-Xiang Li, Rex E Britter, Tieh Yong Koh, Leslie K Norford, Chun-Ho Liu, Dara Entekhabi, and Dennis YC Leung. Large-eddy simulation of flow and pollutant transport in urban street canyons with ground heating. *Boundary-layer meteorology*, 137(2):187–204, 2010.

[29] Seung-Bu Park, Jong-Jin Baik, Siegfried Raasch, and Marcus Oliver Letzel. A large-eddy simulation study of thermal effects on turbulent flow and dispersion in and above a street canyon. *Journal of Applied Meteorology and Climatology*, 51(5):829–841, 2012.

[30] VBL Boppana, Z-T Xie, and IP Castro. Thermal stratification effects on flow over a generic urban canopy. *Boundary-Layer Meteorology*, 153(1):141–162, 2014.

[31] Harindra Joseph Fernando. *Handbook of Environmental Fluid Dynamics, Volume Two: Systems, Pollution, Modeling, and Measurements*, volume 2. CRC press, 2012.

[32] MW Rotach. Profiles of turbulence statistics in and above an urban street canyon.

Atmospheric Environment, 29(13):1473–1486, 1995.

[33] Tsan-Hsing Shih, William W Liou, Aamir Shabbir, Zhigang Yang, and Jiang Zhu. A new k-*epsilon* eddy viscosity model for high reynolds number turbulent flows. *Computers and Fluids*, 24(3):227–238, 1995.

[34] Brian Edward Launder and DB Spalding. The numerical computation of turbulent flows. *Computer methods in applied mechanics and engineering*, 3(2):269–289, 1974.

[35] EH Chui and GD Raithby. Computation of radiant heat transfer on a nonorthogonal mesh using the finite-volume method. *Numerical Heat Transfer*, 23(3):269–288, 1993.

[36] ANSYS Fluent. 12.0 theory guide. *Ansys Inc*, 5, 2009.

[37] ASHRAE Handbook. Fundamentals. *American Society of Heating, Refrigerating and Air Conditioning Engineers, Atlanta*, 111, 2001.

[38] Jörg Franke, Antti Hellsten, Heinke Schlünzen, and Bertrand Carissimo. *Best practice guideline for the CFD simulation of flows in the urban environment*. 2007.

[39] Tim R Oke. Street design and urban canopy layer climate. *Energy and buildings*, 11(1):103–113, 1988.

[40] Ian D Stewart and Tim R Oke. Local climate zones for urban temperature studies. *Bulletin of the American Meteorological Society*, 93(12):1879–1900, 2012.

[41] Xian-Xiang Li, Rex E Britter, Leslie K Norford, Tieh-Yong Koh, and Dara Entekhabi. Flow and pollutant transport in urban street canyons of different aspect ratios with ground heating: large-eddy simulation. *Boundary-layer meteorology*, 142(2):289–304, 2012.

Chapter 4

Realistic Urban Heating and Wind Flow: Air Exchange and Street Ventillation

4.1 Introduction

The world is currently experiencing the largest wave of urbanization in history. According to the 2011 World Urbanization Prospects [1], more than 78% of the population in developed countries already lives in urban areas and the fraction is expected to increase worldwide. As urbanization progresses, microclimate modifications are aggravated in various ways [2–4] and Urban Heat Island effects become more prevalent [5]. The progressive replacement of natural surfaces by impervious materials and buildings modifies regional morphology and land cover. The urban radiation balance is altered by the reflection and obstruction of solar radiation as well as the reduction of thermal radiation losses due to small sky view factors [5]. Building roughness provides

a momentum sink and causes wind sheltering within street canyons. The contrast between the urban and undisturbed climates is further enhanced by the input of anthropogenic heat, moisture and pollutants into the atmosphere by human activities [6]. Therefore, it is essential that we develop more sophisticated and comprehensive methods of urban thermal and flow analysis in order to investigate the combined effect of various urban climate processes.

Thermal forcing plays an important role in determining flow patterns and turbulent transport in built environments [7, 8]. Various surface controls that affect the dynamic thermal and flow field behavior are widely documented in the literature (through numerical modeling or wind tunnel experiments) and are mostly categorized in 4 major factors: 1) building canyon geometry and configuration [9–12], 2) surface thermal properties [13–15], 3) ambient wind speed and direction [15, 16], and 4) distribution and strength of surface heating with respect to the ambient wind [17–22]. When the building facades are heated by solar radiation during the day, buoyancy enhances turbulence [23], and the combination of buoyancy and inertial forces governs the heat and mass removal from the street canyon. For example, when the windward wall is warmer than the air, the upward buoyancy flux opposes the downward mechanical advection in the building canyon, and the flow structure in the building cavity adjusts to these counteracting effects.

It is essential to also recognize the three-dimensional (3D) nature of the urban canopy, including the interaction between buildings under non-idealized conditions [24]. For example, variation of solar position and insolation throughout the day result in 3D heterogeneous distribution of thermal forcing on urban facets. Non-uniform, 3D surface heating is not commonly considered in the literature. Since the solar irradiance

field is not realistic the flow field within and above the canopy is also not expected to represent real conditions. To address this shortcoming, non-uniform thermal forcing and its 3D effect on urban flow field will be investigated.

Convective heat transfer coefficients (CHTCs) at exterior building surfaces determine turbulent heat fluxes and therefore affect building thermal loads and energy demands, canopy air exchange and pollutant dispersion. Empirical CHTC correlations for external urban surfaces have been evaluated using field measurements [25–30] and wind tunnel experiments [18],[22],[31]. However, due to wind direction variability and complex canopy roughness especially in field experiments, the flow field and therefore the CHTC are very sensitive to the boundary conditions and inconsistencies between measurement campaigns were found [32–34]. Wall resolving Computational Fluid Dynamics (CFD) avoids the need to model Convective Heat Transfer Coefficients at external building surfaces [35–38]. However, the computational cost for simulations at realistic Reynolds numbers and over the diurnal cycle is too large. Consequently, simplified correlations are used to calculate or impose the value of CHTC. This results in large discrepancies among some of the widely used building simulation tools as reported by [39] and [40]. The latter suggests 20% to 40% difference in energy demands with different choice of Convective Heat Transfer Coefficient. Furthermore, non-uniform and dynamic surface heating and associated changes in the flow field motivate the investigation of spatio-temporal distributions of CHTCs.

The air removal, or the capacity of the street canyon to "ventilate" itself, has a critical role on air quality, city breathability [41] and therefore quality of life of urban dwellers. Urban airflow and pollutant transport has received significant attention and several parameters have been introduced to quantify the ventilation performance.

Liu et al ([42] and [43]) considered the roof-level fluctuating vertical velocity as the sole responsible mechanism for air removal and pollutant dilution in the 2D street canyon. The Air Exchange Rate (ACH) was introduced by Liu et al [44] to represent the volumetric air per unit time that is exchanged from the street canyon to the surrounding atmosphere. ACH was applied to compare the ventilation efficiency of street canyons [45–48]. The differential heating of building surfaces can also influence the exchange of air and pollutants [8]. Yet, numerical investigations on the effect of buoyancy on canyon ventilation have been relatively rare ([20],[46],[49]) and focused on idealized uniform surface heating scenarios. It is expected that non-uniform heating, significantly affects the air exchange rate.

In this paper, numerical fluid flow and heat transfer simulations of a three-dimensional (3D) urban environment are performed using the finite volume solver ANSYS/FLUENT 14.5. CFD simulation of urban microclimate is shown to be a powerful tool that can accurately model the urban thermal environment, as well as providing the possibility for comparative analysis [50]. Several studies demonstrated the importance of including shortwave and longwave radiation on accurately predicting the urban thermal environment and UHI effects in real urban configurations [50–53], however detailed analysis on the effect of thermal forcing on the local (street-scale) flow field is scarce. In this study an idealized compact low-rise geometry is used for generality [54], and the focus is on the detailed study of the determinants of urban thermal and flow environments. Accordingly, the main objective is to analyze the impact of non-uniform thermal forcing caused by varying incidence angles of direct beam shortwave radiation and shading effects between buildings on mean flow, turbulence statistics, temperatures, and canyon ventilation. Our model also extends

previous urban analysis of CHTCs through a dynamic coupling of heat transfer and fluid flow in a 3D street-scale urban environment. The differential thermal forcing in the building canyon is parameterized through a new potentially universal dimensionless Richardson number. Additionally, more advanced numerical modeling of turbulent flow (Large Eddy Simulation) is performed to improve the accuracy in the state variables and fluxes compared to RANS.

Section 4.2 of the present paper explains the simulation setup, including the model description, numerical methods, grid dependency, and test cases. Different turbulence models are compared and results are validated against experimental measurements in Section 4.3. The relative importance of momentum versus buoyancy forcing is characterized by defining two different Richardson numbers as explained in Section 4.4.2. Results and discussions are further subdivided in three sections: the impact of three-dimensional non-uniform heating on mean flow field is analyzed in section 4.4.3, followed by the analysis of CHTC distribution on building walls (Section 4.4.4), and street canyon ventilation is studied by means of 3D Air Exchange Rate in Section 4.4.5. Conclusions are presented in section 4.5.

4.2 Methods

4.2.1 Model Description

The geometry consists of a matrix of 3x3 equally-spaced buildings with canyon aspect ratio of 1 (AR = Height-to-Width ratio), situated on top of multiple soil layers (Fig. 4.1). This configuration results in a roughness plan aspect ratio $\lambda_p = A_p/A_T$ of 0.25, where A_p is the plan area of roughness elements relative to the total surface

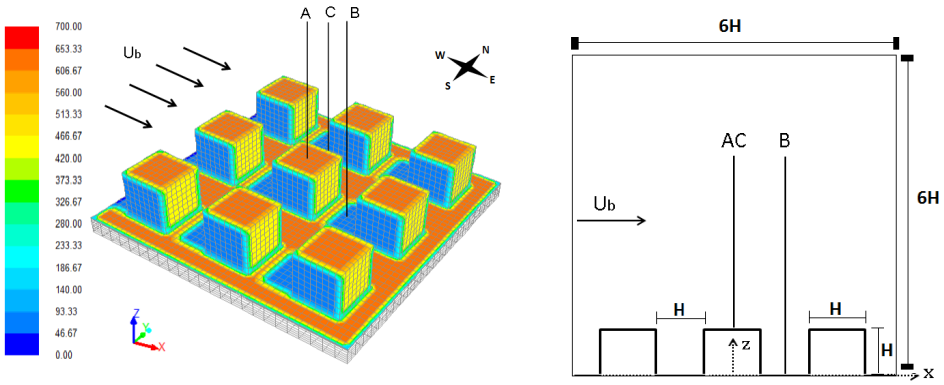

Figure 4.1: Left: Absorbed solar heat flux (S_{abs}) in W m^{-2} in the computational domain for ground surface albedo of 0.18 at 1500 LST on June 21st. Right: X-Z view at plane Y/H=0 with locations where vertical profiles are analyzed. A: Above center building X/H=0, Y/H=0, B: Downwind halfway between buildings X/H=1, Y/H=0, C: Center-line street canyon X/H=0, Y/H=1.

area A_T. The configuration density is classified as the "compact low-rise" areas in the local climate zone (LCZ) classification by Stewart and Oke [54]. The streamwise, spanwise and vertical coordinates are denoted by x, y and z, respectively. To achieve a fully-developed flow field, periodic boundary conditions are used in stream and span-wise directions and a no-shear velocity condition is applied at the domain top ($6H$). Nazarian and Kleissl ([15]) performed domain size sensitivity tests with RANS and concluded that larger domain heights do not affect the results, consistent with [55] who suggested a domain height of $4H$.

The dynamic coupling of flow field and heat transfer is taken into account by simultaneously solving the Navier Stokes equations, energy equation, and Discrete Ordinate non-gray radiation model by [56] in the fluid domain. Natural convection from the heated surfaces and buoyancy effects on the flow are considered and the Boussinesq approximation is used for density. The shortwave radiation (S) is calculated using a solar ray tracing algorithm provided in ANSYS/FLUENT [57] that simulates direct solar radiation and shading by buildings. S is applied to the energy equation

as a source term for each cell and is the primary driver of non-uniform heating of building and ground surfaces. This approach is more realistic than forcing constant non-uniform heat flux on urban surfaces, as other energy balance components are coupled to S. The unsteady conduction heat flux (Q_c) into the thermally massive soil layers is calculated at the ground surface, while the 1D steady heat conduction equation is solved to calculate the external surface temperature of buildings. The thermal properties of soil layers and ground and wall surfaces are as in Nazarian and Kleissl ([15]) and summarized in Appendix A. A constant sky radiation temperature of 255 K is set at the upper boundary of the computational domain to simulate longwave radiation from clear sky conditions. A constant temperature boundary condition (295 K) is used at the external solid surfaces of the domain (the base of the deepest soil layer and the internal surface temperature in roofs and walls) as input to the conduction heat flux calculation from the solid layers. While periodic boundary conditions are considered for the velocities, the inflow air temperature T_a is forced to be homogeneous and to follow the TMY3 diurnal cycle.

4.2.2 Turbulence Modeling and Numerical Methods

The unstructured finite volume solver ANSYS FLUENT 14.5 is applied with a constant time step of 0.1 s resulting in average CFL numbers of 0.3 and maximum CFL numbers of 1-1.1 observed locally in areas of high velocity. After a detailed comparison and validation of various turbulence models (section 4.3), Large Eddy Simulation and Algebraic Wall-Modeled subgrid-scale model (WMLES) is chosen and used with near wall treatment by Werner and Wengle [58] (Section 4.3). The numerical method is described in detail in Nazarian and Kleissl ([15]) and the key points are

restated here. A detailed description of the Large Eddy Simulation model (LES) and Algebraic Wall-Modeled LES Model (WMLES) can be found in Appendix A-C. In the following simulations urban surfaces are considered smooth and the effect of building surface roughness is not included in this study due to the limitation imposed by the ANSYS/FLUENT software that does not allow specifying roughness length when WMLES is used combined with the near wall treatment of Werner and Wengle [58].

4.2.3 Mesh Configuration and Grid Dependency Analysis

The 3D Cartesian grids are built with ANSYS 14.5 resolving each cube cavity with 16 cells in all directions. The grid dependency is tested for the computational domain described in 4.2.1 (3×3 matrix of building with AR=1 and domain height of $6H$). Three structured grid systems as described in Table 4.1 are used. Computing resources limited the range of grid points for the grid dependency analysis. The $2H \times 2H \times 6H$ subchannel unit of the computational domain (Figure 4.2) consists of $32 \times 32 \times 52$ control volumes in the flow along the x, y and z directions, respectively for the coarse grid (Base case shown in Table 4.1). The entire domain contains 9 (3×3) times the area shown in Figure 4.2 or 723,600 cells (including 75,000 cells for the soil layers) in the Base case. The high resolution (HR) cases contain $40\times$ 40×52 control volumes and in case HR-NWR, grids are more refined close to the building walls and ground surfaces to achieve smaller dimensionless wall distance (z^+), which results in better resolution of the energy-containing scales near the wall, but also grid cells with larger aspect-ratio (pencil-like grids) further away from the wall.

Vertical profiles of mean streamwise velocity and streamwise and spanwise

Table 4.1: "HR" stands for "high resolution" and "NWR" refers to near-wall resolution. To obtain the total number of grid points multiply N_x and N_y by 6.

Case	N_x (per $2H$)	N_y (per $2H$)	N_z	$\mathbf{z}^+$
Base	32	32	52	120
HR	40	40	52	80
HR-NWR	40	40	52	30

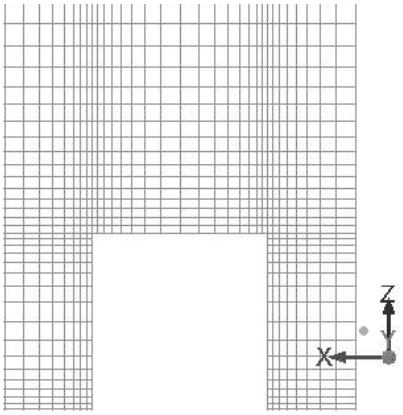

Figure 4.2: Subsection of the computational grids (2Hx2H) in the x-z plane around the building canyon for the Base case (Table 4.1).

velocity variances are compared for different grid resolutions. Downstream of the cube (Location B in Figure 4.1) refining grids in the horizontal directions does not significantly affect the profile of mean velocity and mean temperature (Base versus HR in Figure 4.3). The largest Mean Average Percentage Error (MAPE) is observed for the variance of streamwise velocity in Base case with HR at MAPE = 7%. For the HR-NWR case, results away from the wall are affected by the large aspect-ratio in this region, as also observed by Niceno et al 2002 ([18]). Similar independence to grid resolution and near-wall refinement was observed at the locations A and C and can be attributed to the robust near-wall approach by Werner and Wengle [58] and the WMLES SGS model used. Therefore the computational grid of the Base case is the best compromise between accuracy and computational cost and used for the following

simulations.

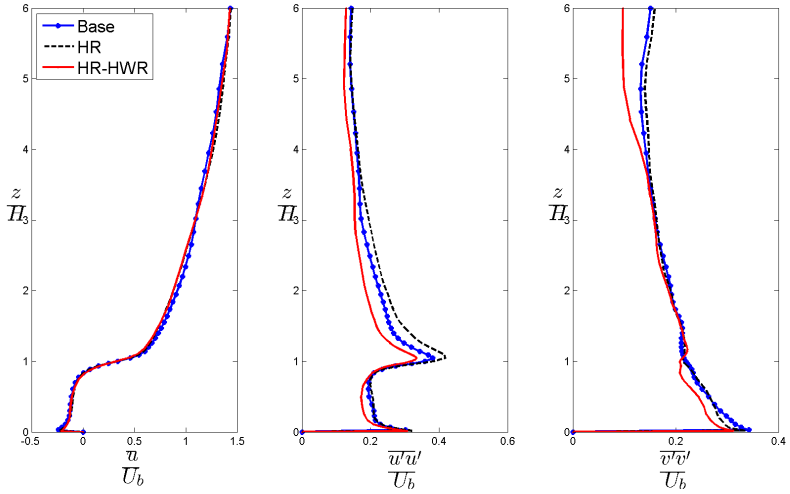

Figure 4.3: Vertical profiles of mean velocity and velocity variances at Location B (Fig. 4.1) and different grids (Tab. 4.1).

4.2.4 Simulation Cases During the Diurnal Cycle

Simulations are conducted for steady-state weather conditions at 06, 08, 10, 12, 14, 16, 18 PST on a clear summer day in San Diego (June 21), and initialized with temperature and wind forcing data using Typical Meteorological Year (TMY3 file for Miramar NAS) data and the solar load model of the corresponding hour. The bulk velocity U_b is forced to be the average wind speed in the Typical Meteorological Year (TMY3) data at a representative coastal urban weather station in southern California (San Diego Miramar NAS, 32°52′N, 117°09′W). In the streamwise direction a corresponding mass flow rate is specified and the Reynolds number based on the cube height $Re_H = U_b H/\nu$ is 5.2×10^5. To confirm that a quasi-steady state (t_{qs}) was reached before data collection commenced, resolved and normalized resolved turbulent kinetic energy ($k^+ = \frac{k}{u_\tau^2}$) averaged over the whole domain was monitored as a function of time, where k is the turbulent kinetic energy and u_τ is the friction velocity near

ground. The sampling time for computing time averages is set to 1500 s time interval, which is at least 15 times the Lagrangian integral time scale (t_L) and then output is sampled every 10 time steps ($1s$) .

4.3 Validation and Turbulence Model Comparison

In order to choose and validate the appropriate turbulence model provided in FLUENT, Detached Eddy Simulations (DES), and Large Eddy Simulations (LES) are compared to an experiment by Meinders [59] and the LES simulation of Niceno et al [18]. The standard Smagorinsky subgrid-scale model was used in [18], and the first grid point was at $z^+ \approx 1$.

The experimental measurements by Meinders [59] were conducted for a heated cube placed in an equidistantly spaced matrix of wall-mounted cubes in a wind tunnel. The center-to-center distance between cubes are $4H$, were H is the height of the cubes. The height of the channel is $3.4H$.

The subchannel unit of dimension $4H \times 4H \times 3.4H$ is chosen as the computational domain and periodic boundary condition are applied for the streamwise and spanwise directions, x and y, respectively, consistent with the LES simulation in Niceno et al [18]. However, since only the center cube is heated in Meinders, periodic boundary conditions are not applied for temperature; instead the inlet temperature is fixed to 20°C. No slip and 20°C boundary conditions is also applied for channel floor and domain top. The center cube is heated using a constant-temperature core (75°C) covered with a thin layer of 0.1 H thickness and thermal conductivity of 0.24 W m^{-1} K^{-1}. In our simulation the cube thickness is not resolved by grids; instead the 1D steady heat conduction equation is used to calculate the external surface temperature.

The computations were performed at a Reynolds number based on the cube height of $Re_H = U_b H/\nu$= 3,854, and a corresponding mass flow rate is specified in the stream-wise direction.

Table 4.2: List and acronyms and reference for turbulence models used in the intercomparison.

LES DS	Large Eddy Simulation with Dynamic Smagorinsky Subgrid-Scale Model	Germano [60]
LES WMLES	Large Eddy Simulation with Algebraic Wall Subgrid-Scale Model	Shur et al. [61]
DDES SA	Delayed Detached Eddy Simulation based on Spalart-Allmaras	Spalart et al [62]
DDES Ke-R	Delayed Detached Eddy Simulation based on $k-\epsilon$ Realizable	-

The turbulence models are described briefly in sections 4.2.2 and Appendix B-C. Large Eddy Simulation with two different SGS models and two different Delayed Detached Eddy Simulation models are used in this comparison as summarized in Table 4.2. Since Heidarzadeh et al. [38] found that WALE (Wall-adapting local eddy viscosity) models were inferior to DDES models in FLUENT simulations of convective heat transfer over a wall mounted cubes, the WALE model is not included in this comparison.

Figures 4.4 shows the vertical profile of time-averaged normalized streamwise velocity and the normalized streamwise and spanwise velocity variances in the canyon downwind of the heated building. URANS models are also compared but not included here as they were shown to be inadequate in predicting the velocity fluctuation and other turbulent parameters especially in the canyon region. The Algebraic Wall-Modeled Large Eddy Simulation (WMLES) model with near-wall treatment is closest to the experimental data, and this is also observed at the other locations (not shown). The vertical profile of streamwise velocity is captured well, especially in the region

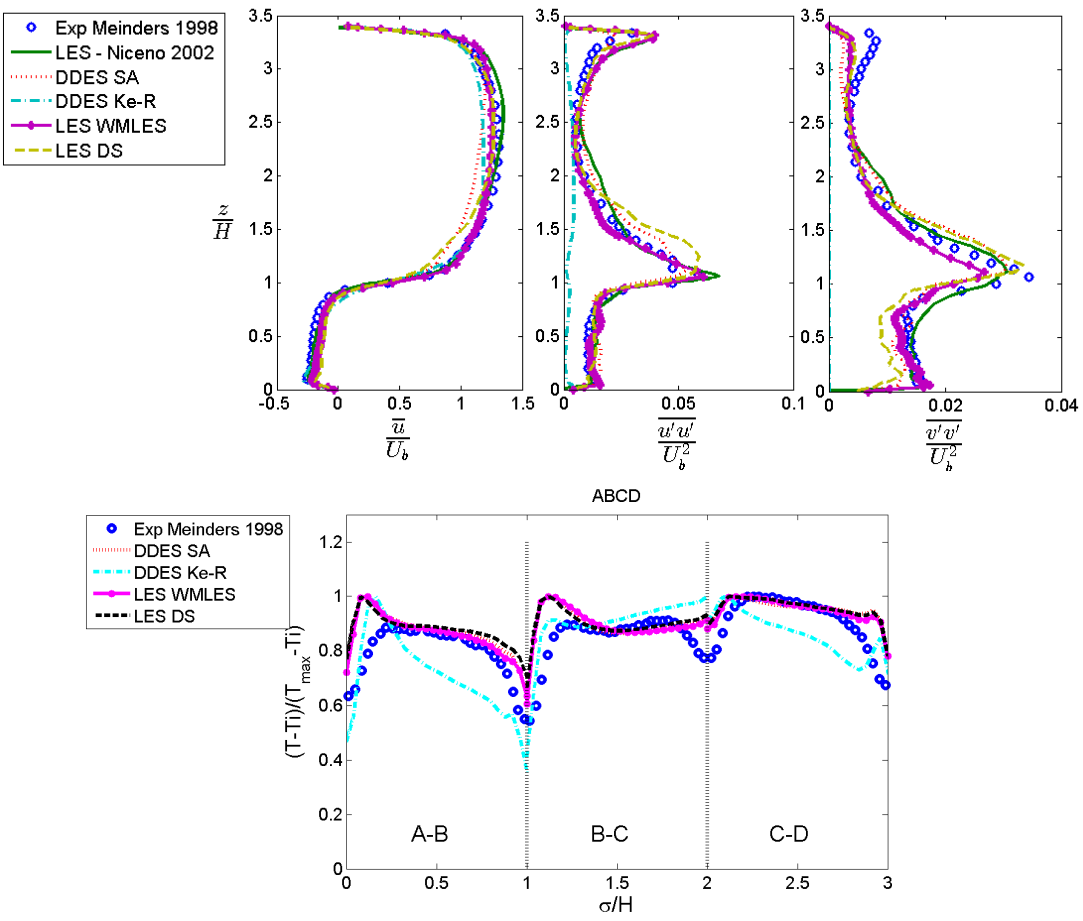

Figure 4.4: Top: Vertical profiles of mean velocity and velocity variances at Location B (Fig. 4.1) and different turbulence models (Tab 4.2). Bottom: Distribution of the normalized surface temperature along the path ABCD.

close to the wall. On the other hand, the larger vertical grid spacing above the buildings results in larger cell aspect-ratio (pencil-like cells) and negatively influenced the accuracy in this region. Nevertheless the agreement of WMLES results with experimental data for both mean and variance of the streamwise velocity is improved compared to Niceno et al [18], while the spanwise variance is slightly less accurate between $1 < z/H > 1.5$. The calculated temperature of the building surfaces is also validated following the same methodology and it is concluded (Figure 4.4) that LES models with Mean Absolute Percentage Error (MAPE) of 7-8.5 percent outperform

the DDES model (MAPE of 12.3 percent for DDES Ke-R) on their prediction of urban surface temperatures. The WMLES results are in close agreement with the experimental data in the center sections of the building surfaces, while larger errors exist near the edge of the cubes. The deviation can be attributed to the following reasons. First, a near-wall resolution of y+ of 1 is recommended by Niceno et al. [18] to accurately represent the near surface fields. In our validation study, the y+ ranges from 5-15, and the maximum occurs at the corners, specifically at the corner of the windward wall. Therefore lower resolution can contribute to the deviation of surface temperature at these locations. Additionally, the temperature boundary condition at the channel floor and domain top is set to be constant in the CFD simulation, while heterogeneity may exist in the experiment as these temperatures are not controlled.

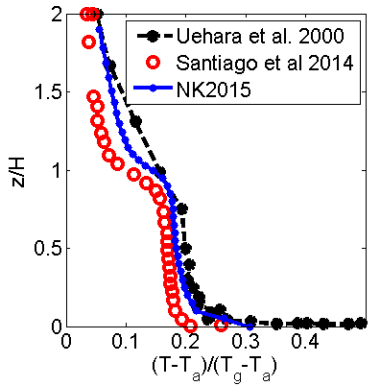

Figure 4.5: Vertical profile of normalized temperature $(T - T_a)/(T_g - T_a)$ at Location B (Fig. 4.1) for WMLES model.

For a more comprehensive validation of simulated temperature, the experimental data from Uehara et al. [11] have been used (similar to previous studies by Xie et al., [46]; Park et al., [21]; and Santiago et al. [63]). The experimental configuration is so that the temperature of the ground is higher than the ambient air temperature. The simulations are conducted for a bulk Richardson number ($Ri_b = gH(T_a - T_g)/T_a U_b^2$) of

-0.21, where T_g is the canyon floor temperature. Here, this configuration is modelled with the same resolution and same geometrical simulation setup as in Section 3 to validate the model under the same conditions as in the simulations used to produce the results for this paper. The temperature profile calculated with the LES in this study (NK2015 in Figure 4.5) shows improved accuracy compared to the RANS simulation of Santiago et al. [63], with normalized mean square error (NMSE) of 0.97×10^{-2} compared to NMSE value of 1.3×10^{-2} in [63]. The temperature profile is well reproduced in the street canyon with MAPE of 9 percent, while the temperature is underestimated above the building height and close to the floor and can be attributed to the grid resolution in the boundary layer region as discussed before.

4.4 Results

4.4.1 Thermal Forcing in the Canyon

Previous studies pointed to the importance of thermal forcing on microclimate, but limited their evaluation to uniform heating of merely one surface, which is unlikely in realistic conditions. The significance of three-dimensional non-uniform heating is analyzed in this section. For reference, a neutral case (called "N" onward) is simulated where the solar forcing is zero and the temperature of all surfaces is equal to the inlet air temperature at 288.4 K.

The sunlit wall configuration and solar heat flux intensity depends on time, location, and street canyon geometry. Figure 4.6 shows time-averaged snapshots at different Time of Day (ToD) of non-uniform surface temperature on building walls. Results in the right column of the figure are averaged over the $H\times H\times H$ volume

downwind of the center building in the spanwise canyon, hereonafter referred to as "Building Canyon" and indicates the non-uniform ground heating in the spanwise canyon. At 0600 and 0800 PST, the leeward wall of the building is partially heated, while the magnitude of solar heating and the ratio of the heated to overall wall surface at 0800 PST is significantly larger. From 0800 to 1000 PST, the transition from non-uniform to uniform leeward heating occurs, and the ground surface in the building canyon is also partially subjected to solar heating (shown in the right column). Solar heating is near uniform and mostly restricted to the ground and roof surfaces at noon (solar noon is at 1150 PST). Afterwards, wall heating transitions to windward and the magnitude of solar insolation and ratio of the heated wall decrease from 1400 to 1800 PST. The ground surface in the streamwise canyon (E-W outside the building canyon) and roof surfaces encounter only minor shadowing throughout the day, except for 0600 and 1800 PST when the solar altitude is low. Additionally, roof heating is significantly larger than uniform wall heating at 1000 and 1400 PST. Similar to east and west walls, north and south walls also go through heating transition, affecting the flow structure and temperature distribution in the building canyon.

4.4.2 Characterizing Momentum Versus Buoyancy Forcing

Traditionally, the bulk Richardson number calculated based on the vertical temperature gradient is used to quantify the thermal instability in the street canyon. Few studies (including [63]) used the total surface heat flux for calculating the buoyancy parameter. The characteristics of the thermally stratified flow also depend on the canyon aspect ratio. Fernando et al [64] assumed that $\frac{\partial u}{\partial x} \sim \frac{\partial w}{\partial z}$ and showed that the defined buoyancy parameter becomes proportional to the reciprocal of aspect

ratio squared $(W/H)^2$ for a 2D canyon. Additionally, Dallman et al [65] introduced a non-dimensional buoyancy parameter, B, considering the canyon aspect ratio and temperature difference between walls; however this buoyancy parameter does not distinguish the directionality of the temperature gradient. Using CFD of a 2D street canyon, Magnusson et al [66] also concluded that the results are dependent on the canyon aspect ratio as B varies, despite the fact that AR is included in the buoyancy parameter, B.

As of yet, the methods to characterize thermal forcing neglect the horizontal temperature gradient, and fall short in comprehensive characterization of the flow. Here we define two non-dimensional numbers to convey more information about the directionality of thermal forcing in relationship to the canyon vortex in addition to the bulk vertical instability in the canyon. Canyon aspect ratio appears in the definition of horizontal Richardson number, however the effect of geometry is not analyzed in this paper.

The bulk Richardson number, $\mathrm{Ri_v}$, indicates the atmospheric stability in the vertical direction

$$Ri_v = \frac{gH}{(U_b^2)} \frac{(\overline{T_H} - \overline{T_g})}{T_a} \ , \tag{4.1}$$

where $g = 9.81$ ms^{-1} is the gravitational acceleration, T_H is the air temperature at roof level, T_g is the temperature of the ground surface inside the building canyon (Fig. 4.6), T_a is the inflow air temperature, and U_b is the bulk wind velocity in the streamwise direction. T_g and T_H are averaged over the building canyon and in time (the two spanwise canyons downwind and upwind of the center building as described in Section 4.4.2).

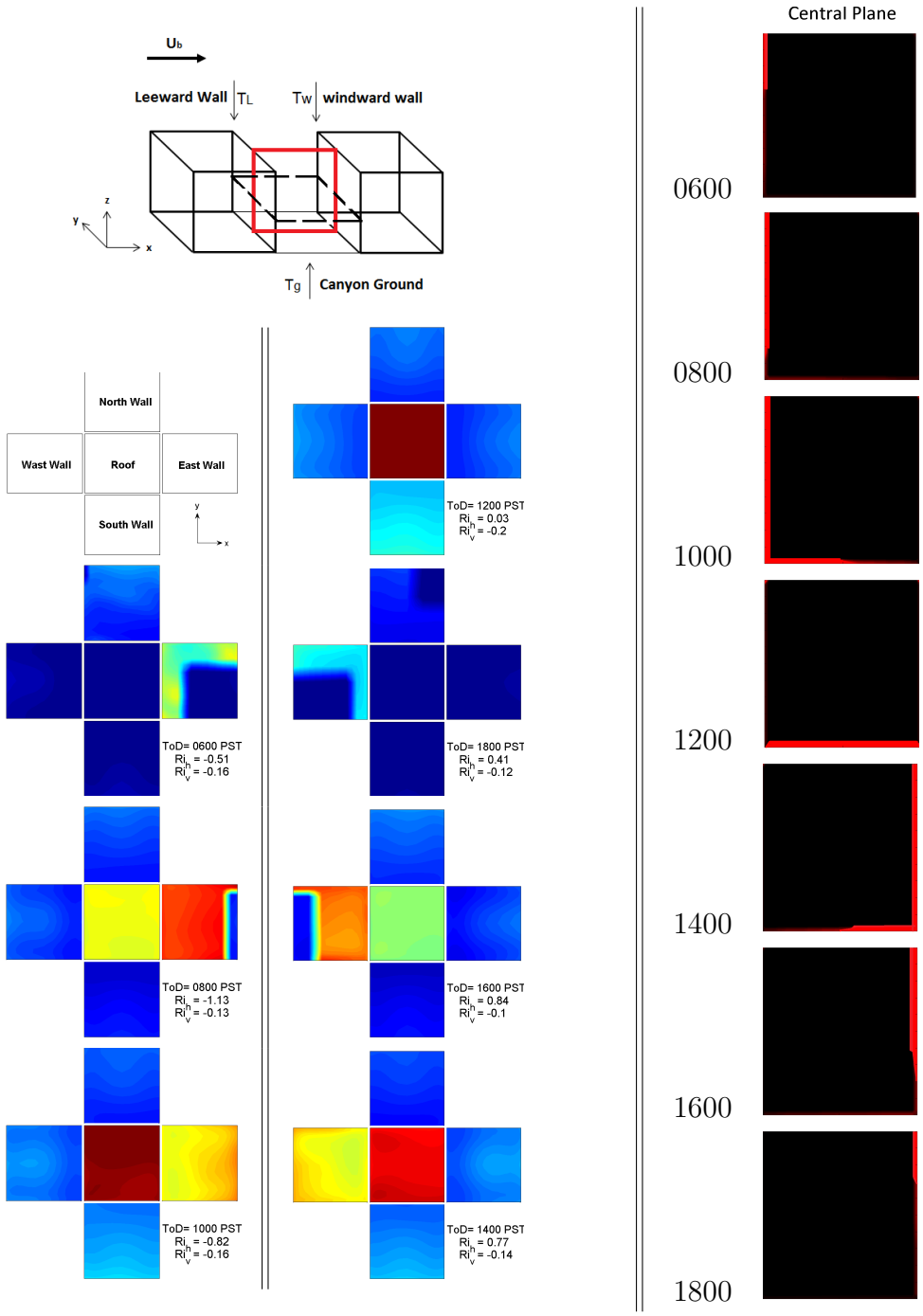

Figure 4.6: Schematic of surface temperature distribution at building walls at different Times of Day (ToD). The three dimensional geometry of buildings and the spanwise canyon between them is shown on the top left; with the red square indicating the vertical plane at the center of the building canyon. The right column displays sunlit surfaces in that plane including the ground surface which is not shown in the left column and can be used as a reference for following figures. The dashed square in the top left figure indicates the horizontal plane at $z/H = 0.5$ used later.

However, since the orientation of the heated wall affects the flow field inside the canyon, bulk Richardson number is not sufficient to characterize the flow field. In the micro-climate of the urban canyon, the temperature gradients in horizontal directions ($\frac{\partial T}{\partial x}$ and $\frac{\partial T}{\partial y}$ in the span-wise and stream-wise canyon, respectively), as well as the wind direction are expected to impact the strength of the canyon vortex. In the building canyon with wind direction as shown in Figure 4.1, the ratio of these terms forms a new buoyancy parameter as

$$Ri_h = \frac{\frac{g}{\overline{T}}\overline{\frac{\partial T}{\partial x}}}{(\overline{\frac{\partial U}{\partial z}})^2} \sim \frac{\frac{g}{T_a}\frac{(\overline{T_L}-\overline{T_W})}{W}}{\frac{U_b^2}{H^2}} \tag{4.2}$$

$$= \frac{gH}{U_b^2}\frac{(\overline{T_L}-\overline{T_W})}{T_a}\frac{H}{W} \ , \tag{4.3}$$

where T_W and T_L are the averaged surface temperature on windward and leeward walls (here west and east), respectively. $\mathrm{Ri_h}$ therefore indicates the effect of differential solar heating and also incorporates the effect of canyon aspect ratio H/W. Additionally, if the wind direction is not aligned with the streamwise canyon, bulk velocity (U_b) should be multiplied by $cos\alpha$, where α is the deviation angle (in the clockwise direction) from the stream-wise canyon. Ri_h combined with the commonly used bulk Richardson number Ri_v introduces a new potential way of comprehensively characterizing the flow under realistic surface heating.

Figure 4.7 shows the variation of $\mathrm{Ri_v}$ and $\mathrm{Ri_h}$. $\mathrm{Ri_v}$ ranges from -0.1 to -0.21 under unstable conditions between 0600 to 1800 PST, which is in the range of values reported by Nakamura and Oke [7] in urban field observations. The magnitude of Ri_v peaks at 1200 PST when ground heating peaks. The diurnal cycle of Ri_v deviates from what would be expected in reality for the following reason. The inlet air temperature,

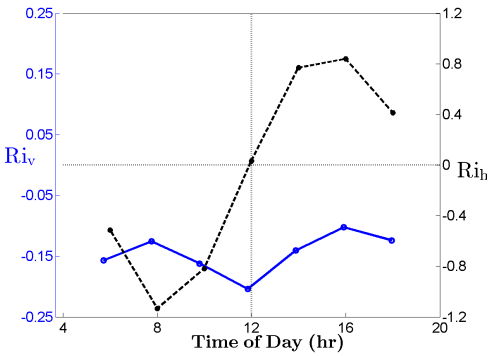

Figure 4.7: Richardson number variation with Time of Day (ToD). Blue solid line represents the vertical Richardson number (Ri_v) corresponding to the left vertical axis, and black dashed line shows the horizontal Richardson number (Ri_h) corresponding to the right axis.

T_a, is set to the hourly air temperature from TMY3 data, and T_g follows the same diurnal pattern as T_a (not shown). This is partially an artifact of our simulation setup; steady-state simulations at different ToD ignore prior heat storage in the ground that cause T_g to exhibit a greater amplitude than T_a in reality. However, our simulation setup allows us to focus on the effect on thermal forcing due to solar insolation only, and not to combine the additional effect of ground thermal inertia especially in afternoon hours. At 0600 and 1800 PST, in the absence of roof heating T_g is relatively warmer than T_H compared to 0800 and 1600 PST, resulting in larger atmospheric instability. There is some asymmetry in the graph due to the solar noon occurring before 1200 PST.

The Ri_h exhibits large variations with ToD. The sign of the $\mathrm{Ri_h}$ indicates whether the canyon is subject to windward or leeward heating as a result of solar azimuth changes. The sign of $\mathrm{Ri_h}$ changes after 1200 PST while its magnitude is symmetrical about noon. $\mathrm{Ri_h}$ peaks when the temperature gradient between building walls reaches its maximum. Ri_v and Ri_h are both zero for the neutral case (N).

4.4.3 Flow and Thermal Field in the Building Canyon

The flow and heat transport as influenced by the three-dimensional non-uniform heating is analyzed. This section is structured as follows. First, the effect of 3D thermal forcing on air temperature inside the canyon is analyzed (see Fig. 4.8 and 4.9 later). Then, the flow field and the canyon vortex are compared at different ToD, through vector and contour plots of time-averaged velocity components as well as pressure fields in the spanwise (N-S) and streamwise (E-W) cross sections (Figs. 4.10 - 4.13). Lastly, time-averaged turbulent kinetic energy (TKE) is calculated in order to measure the intensity of turbulence as effected by combined forcing of buoyancy and shear (Fig. 4.14). The results are calculated at the vertical and horizontal plane in the center of the spanwise canyon (red and dashed squares, respectively, in Fig. 4.6) and time-averaged over 1500 s corresponding to at least 15 times the integral time scale (Section 4.2.4). The results are also compared with previous studies with uniform heating of one or two urban surfaces in 2-D and 3-D canyons.

The effect of wall heating on air temperature inside the building canyon is shown in Figure 4.8 and 4.9. The spatial distribution of air temperature in the vertical plane (Fig. 4.8) demonstrate the transition from leeward (E-Facing) to windward (W-Facing) heating in addition to effects originating from the roof, while the results in horizontal cross sections (Fig. 4.9) allow the study of thermal forcing from the streamwise street canyon. At 1200 PST, the heat advected from the roof surface causes a larger temperature increase in the canyon than the convection from the ground (Fig. 4.8). Additionally, at 1200 PST the south-facing wall is warmest due to the southerly sun position and heat is advected into the spanwise canyon from the south (Fig. 4.9 - 1200 PST). Therefore air temperature and flow field (described in more detail below)

at 1200 PST deviates from the widely studied case of canyon ground heating (for example [17] and [22]).

The distinction between leeward versus windward wall heating is also apparent on the air temperature inside the building canyon. When the leeward wall is heated at 0800 and 1000 PST, elevated temperatures are more concentrated near the leeward wall and the heat is primarily transported vertically. For example at 0800 and 1000 PST the leeward heating adds to the effect of roof heating in heating the air at the top of the canyon, while the effect of partial ground heating at 1000 PST is less significant. In the windward heating cases, however, higher air temperature is observed within the canyon suggesting enhanced heat transfer and mixing inside the canyon (Fig. 4.9). This behavior is also reported in the study by Cai et al. [67] that analyzed the combined effect of uniform roof and wall heating in a 2-D canyon.

The contour plots of mean velocity magnitude superimposed by velocity vectors are shown in Figures 4.10 and 4.11, followed by the plots of static pressure (Figs. 4.12 and 4.13). Throughout the day, only one vortex is observed in the vertical plane and the vortex center is located above $z/H = 0.75$. While the windward wall is strongly heated in the afternoon ($Ri_h = 0.79$ and 0.83 at 1400 and 1600 PST, respectively) the thermal forcing from the heated wall is not enough to create a secondary vortex in the 3-D canyon. Our finding of a single vortex is consistent with field measurement of Offerle et al [68] who did not observe a secondary vortex near the windward wall as reported in previous numerical studies. The wind tunnel experiment of Allegrini et al [22] and numerical simulation by Kim and Baik [17] that analyzed uniform ground heating suggest that the vortex intensity increases with heating in canyons with small aspect ratio (range of 1 to 1.2). In our simulations, building aspect ratio is in that

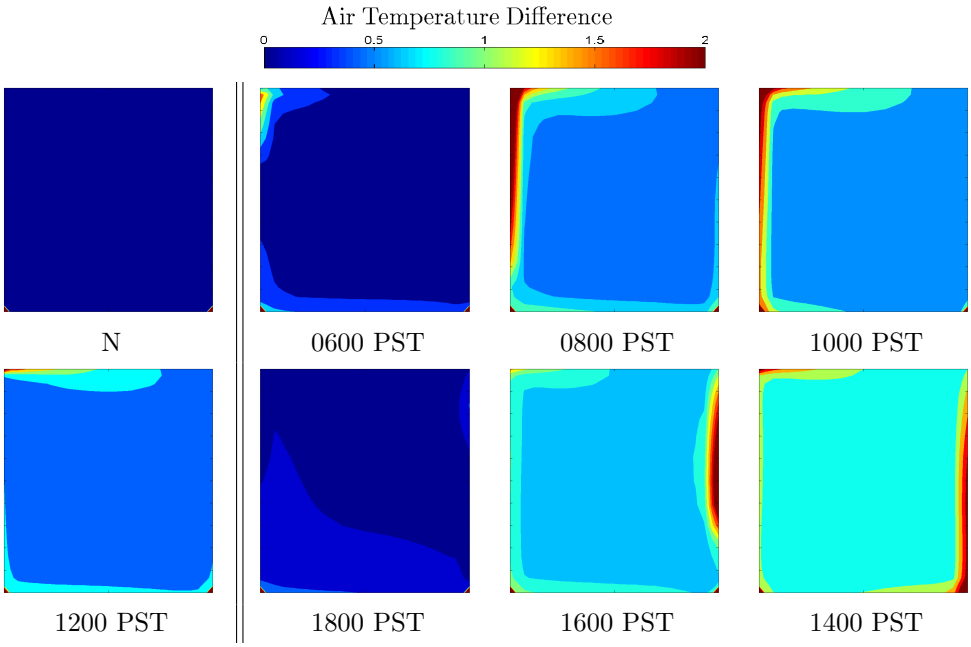

Figure 4.8: Contour plots of the air temperature anomaly from the inlet air temperature ($(T(x, z, t) - T_a(t))$) at different ToD. Results are calculated at the vertical plane in the building canyons (red square in Fig. 4.6) and time-averaged over 1500 s. The plots are arranged such that axisymmetrically opposed horizontal thermal forcing, i.e. similar $|Ri_h|$ as at 1000 and 1400 PST, are in one column. The left column shows the neutral case (N) and noon where wall heating is symmetric.

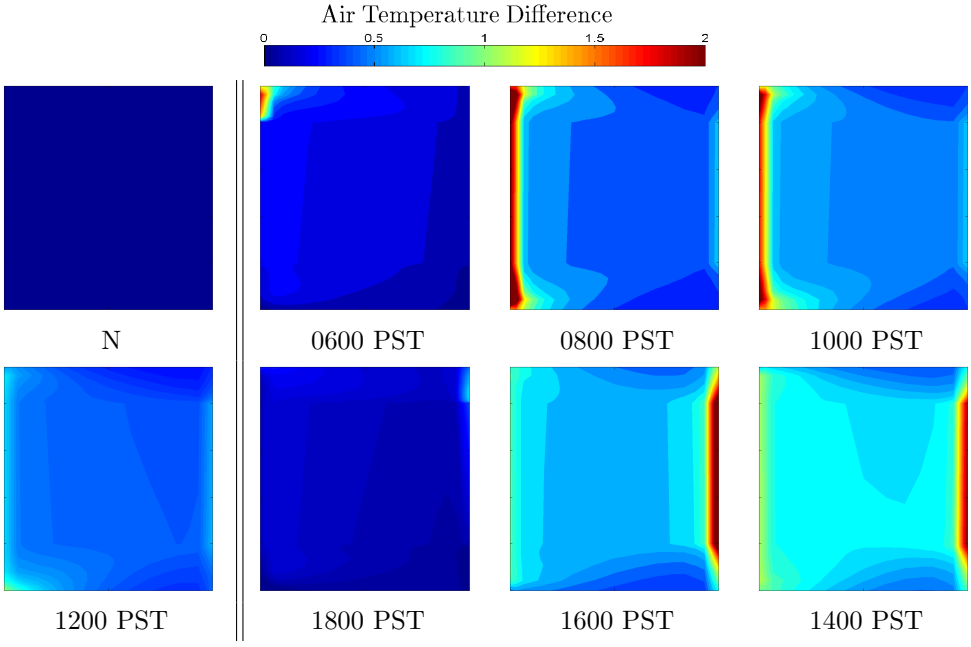

Figure 4.9: Similar to Figure 4.8 for the horizontal cross section at $z/H = 0.5$ (dashed square in Fig. 4.6).

range (AR=1) and the temperature gradient between ground and air at roof level at 1200 PST is approximately 6 K (Ri_v =-0.2 and Ri_h=0). However, the vortex intensity decreases at 1200 PST in contradiction with the uniform ground heating scenario of [17] and [22]. We hypothesize that the presence of roof heating causes the vortex intensity to decrease and the center location is shifted closer to the windward wall.

In comparison with the uniform ground/roof heating at 1200 PST and the neutral case (N), two regimes are observed:

a) In near neutral conditions of 0600 and 1800 PST without significant roof or ground heating, the flow structure is consistent with the neutral simulation (N) as expected. The flow field in this regime is only affected by the strength and orientation of the wall thermal forcing. While the vortex strength slightly increases for leeward heating (0600 PST), the fact that the changes in the flow are minor at 0600 versus 1800 PST despite the large variation in Ri_h suggest a dominance of inertial over buoyancy forcing. The weak effect may also be a result of the location of the heated wall. While the Ri_h consider the average wall temperature, natural convection scales with L^3 and therefore the short section of heating (Fig. 4.6).

b) In unstable conditions between 0800 to 1600 PST the flow is consistent with the 1200 PST simulation. The flow field in this regime is characterized by the superposition of wall, ground and roof heating in both building canyon and the streamwise canyon. Although the distinction between windward and leeward heating is apparent in the temperature fields (Figure 4.8 and 4.9), apparently other factors dominate the flow field as the vortex in Fig. 4.10 appears unchanged. For example, throughout the day the ground in the streamwise (E-W) canyon is mostly unshaded. However large velocity in the streamwise canyon results in larger convection therefore

lower temperatures at the floor of the streamwise canyon and this effect is commonly neglected in the literature. The effect of this temperature gradient in the spanwise direction is then seen in the horizontal pressure gradient (Figure 4.13). Additionally, the temperature difference between the air above the heated roof, and air at roof level averaged inside the canyon is dynamic during the day. For windward wall heating (Ri_h >0), larger horizontal (streamwise) temperature gradient exists at the roof level, therefore a lower pressure gradient is observed inside the canyon (upper part of the building canyon except for the top right corner) compared to the leeward heating cases. This horizontal pressure gradient results in higher velocity at the roof level and higher kinetic energy entering the building canyon in windward heating cases (Ri_h >0). Therefore, while considering the wall forcing only a weaker vortex would be expected, holistic consideration of the three-dimensional thermal forcing shows that other effects dominate. However, the location of the canyon vortex is affected by the wall heating. For leeward heating (Ri_h <0) the center of the canyon is closer to the windward wall. We hypothesize that the cooler air towards the top of the canyon (Fig. 4.10, 0800 and 1000 PST versus 1600 and 1400 PST) is partially caused by buoyancy from the leeward wall causing a weakening of the vertical pressure gradients near the canyon top (Fig. 4.12) and therefore less flow into the canyon from the top.

Additionally, when comparing the mean vertical velocity for cases with symmetrically opposed wall heating (not shown), the downdraft velocity is smaller compared to the neutral case at 1400 and 1600 PST due to windward heating that counteracts momentum forcing. However, the downward vertical velocity is larger at 1400 and 1600 PST than during hours with leeward heating. This can again be explained by the increase in vortex intensity due to the horizontal pressure gradient effect for the

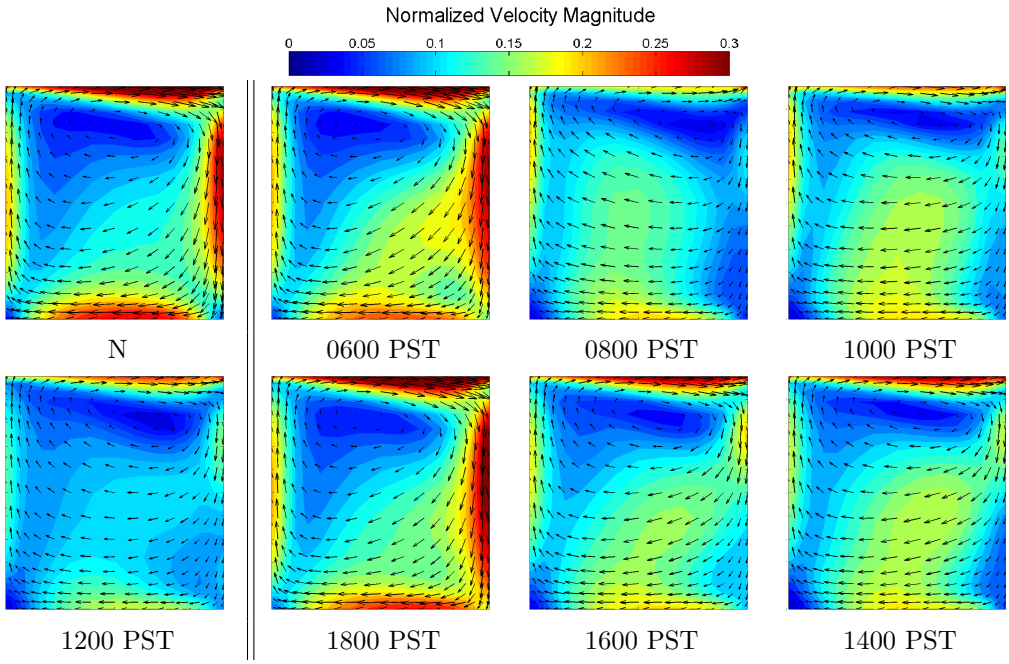

Figure 4.10: Contour of mean velocity magnitude normalized by bulk wind velocity, $\frac{\bar{U}}{U_b}$, overlaid by the mean velocity vector field at different ToD. Results are calculated at the vertical plane in the building canyon and time-averaged over 1500 s.

windward heating cases that brings more momentum into the canyon. The region of updraft velocity is also larger for negative Ri_h (leeward heating).

The three-dimensionality of thermal forcing is also apparent in horizontal cross section of the building canyon ($z/H = 0.5$ in Fig. 4.11). Two counter-rotating vortices are observed. While symmetrical in the neutral (N) case, the heat advected from the warmer wall in the streamwise canyon (North or South, see also section 4.5 and Fig. 4.6) affects the size and strength of the vortices in the horizontal plane. For example, the north-facing wall is warmer at 0600 and 1800 PST and convection of heat transported from the north wall creates a low pressure region in the streamwise canyon that weakens the pressure differential to the spanwise canyon resulting in a weaker north vortex. Similar albeit weaker behavior is observed at 0800 and 1600 PST (weak north wall heating, Fig. 4.6) as well as 1200 PST, when south wall heating

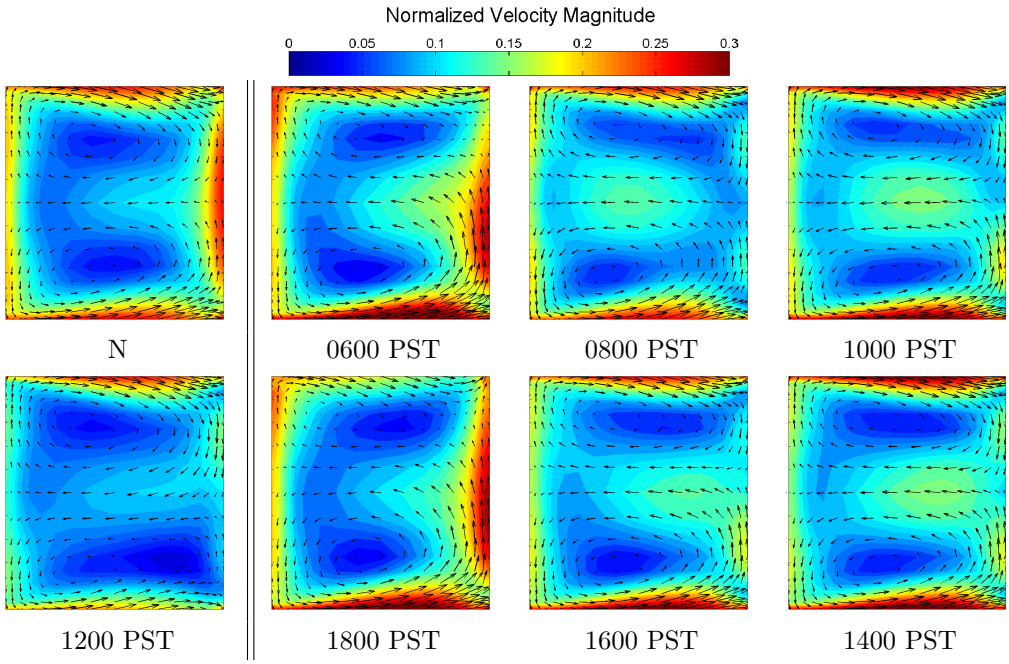

Figure 4.11: Similar to Figure 4.10 at the horizontal cross section shown in figure 4.6.

affects the southern vortex. At 1000 and 1400 PST, however, strong east-west wall heating in addition to ground heating seems to overcome the effect of the warm south wall and the two vortices are more symmetrical. The asymmetric behavior of flow in the horizontal plane is further analyzed in Section 4.4.5 in the context of air exchange from the building canyon.

Figure 4.14 shows the contour plots of turbulent kinetic energy (TKE) at the central vertical plane of the cross-stream canyon. In all cases, the highest TKE is observed in the area of large shear near the windward wall where the air enters the building canyon from above. Even when shear ($\frac{du}{dx}$) is smaller near the windward wall (0800 to 1600 in Fig. 4.10), TKE remains elevated there especially for the cases with windward heating (1400 and 1600 PST), presumably due to intermittent (counter-flow) buoyant updrafts. In leeward and ground heating cases, buoyancy acts in the same direction as the flow, adding to the kinetic energy in the building canyon while the

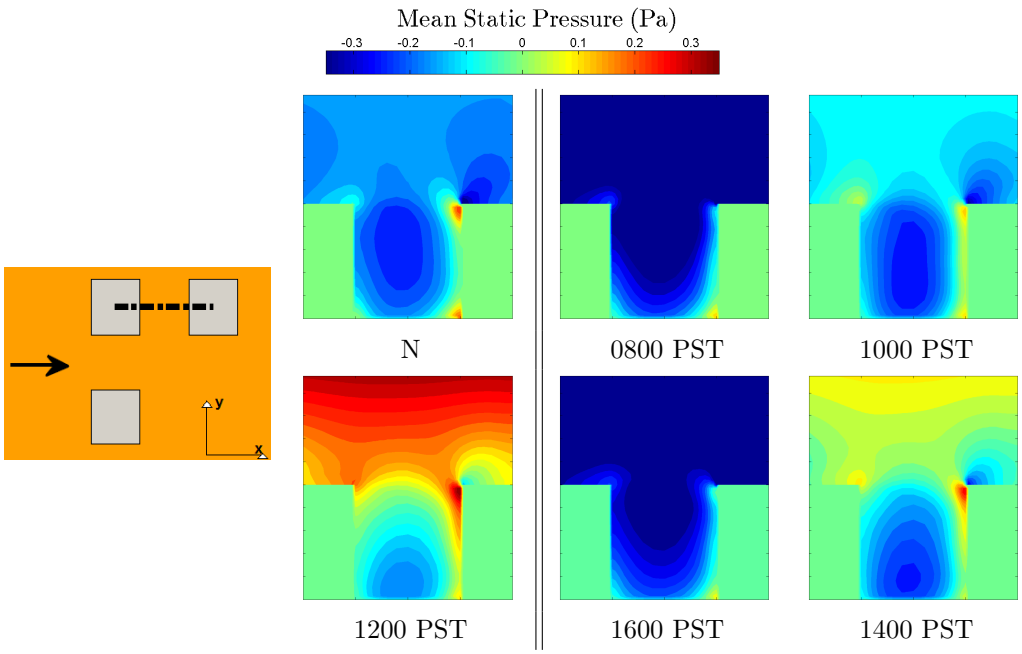

Figure 4.12: Contour plots of mean static pressure (Pa). Results are calculated at the vertical plane (x-z) in the building canyons and time-averaged over 1500 s.

windward heating causes larger TKE near the heated wall due to opposing thermal and momentum forcing. In the second regime (from 0800-1600 PST), the TKE inside the canyon increases for windward, leeward and ground heating (in that order). Horizontal cross-sections of TKE (not shown) support these conclusions.

4.4.4 Convective Heat Transfer Coefficient

The accurate evaluation of CHTCs on exterior building surfaces requires that the grid is refined in the boundary-layer region in order to obtain y+ (dimensionless wall distance) value of about 1 [36, 37]. However, due to the computational cost associated with the low resolution of the LES, this requirement cannot be met in the current study, therefore it is expected that the limited wall resolution may impact the CHTC accuracy, especially in the areas near the edge of building walls (as shown by

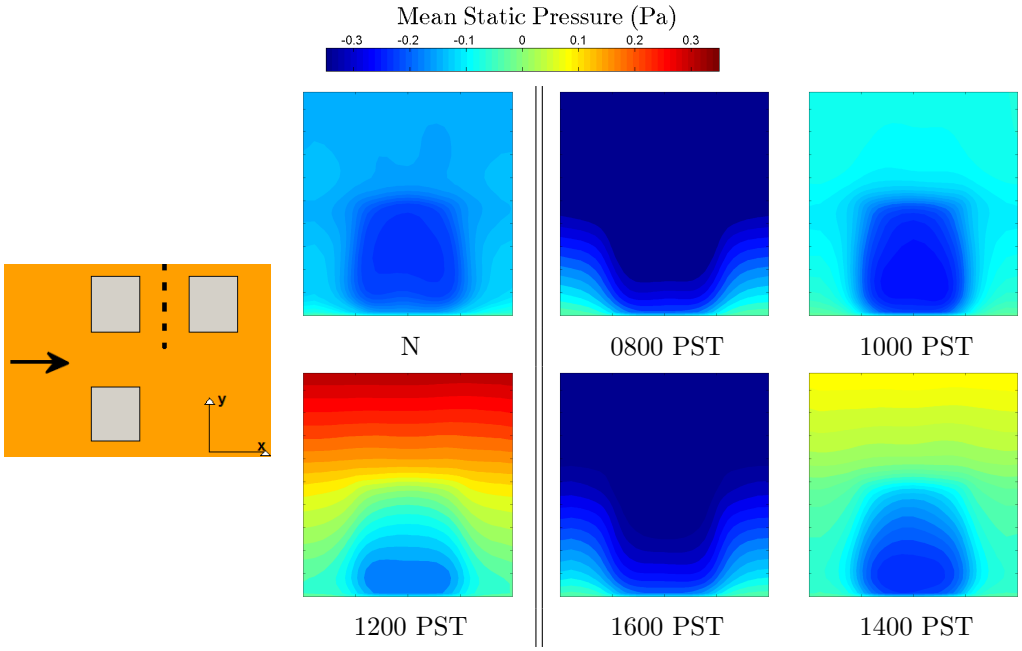

Figure 4.13: Contour plots of mean static pressure (Pa). Results are calculated at the vertical plane (y-z) in the building canyons and time-averaged over 1500 s.

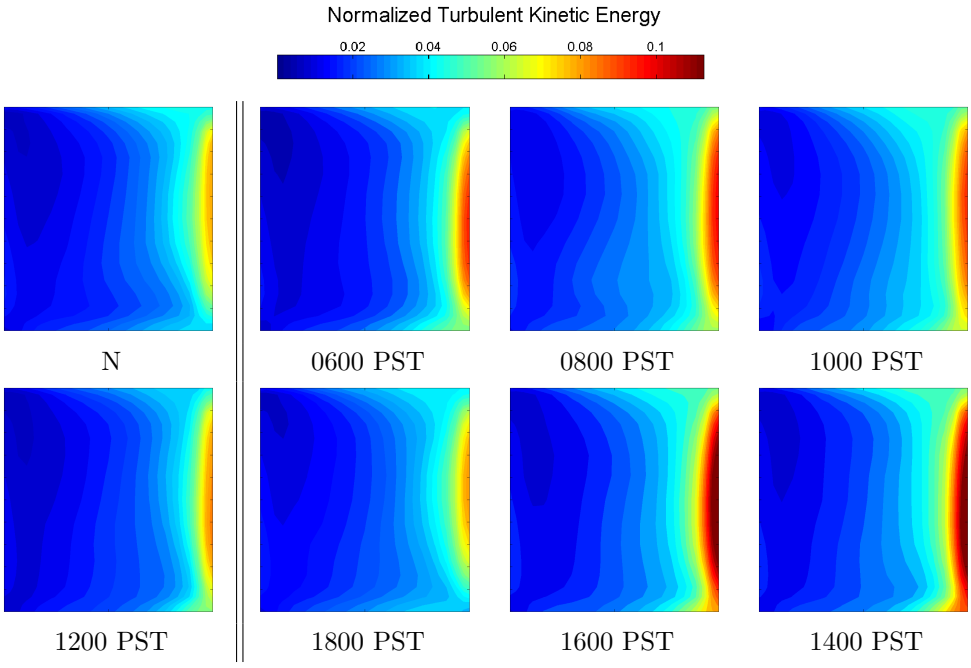

Figure 4.14: Contour plots of Turbulent Kinetic Energy normalized by U_b^2 with Time of Day (ToD). Results are calculated at the vertical plane in the span-wise building canyons (Fig. 4.6) and time-averaged over 1500 s. The plots are arranged such that axisymmetrically opposed horizontal thermal forcing, i.e. similar $|Ri_h|$ as at 1000 and 1400 PST, are in one column. The left column shows the neutral case (N) and noon where wall heating is symmetric.

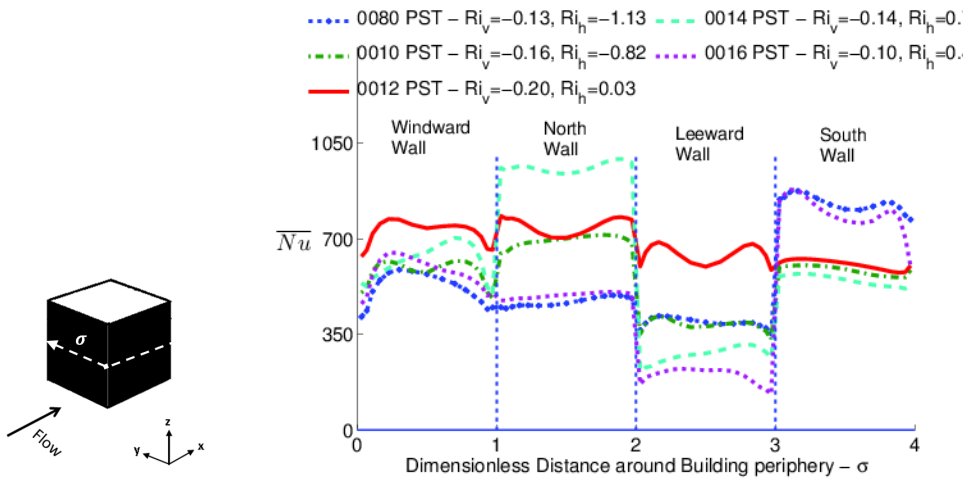

Figure 4.15: Local Nusselt number in the peripheral direction. For aesthetic reasons only selected ToDs are shown.

Figure 4.4 in the Section 4.3). However, the relative variation of CHTC at different times of day is presented to evaluate the sensitivity of CHTC to the non-uniform surface heating. This evaluation can further improve our understanding on the relative importance of thermal and momentum forcing inside the canyon on the outdoor ventilation performance.

In this section, we analyze local Nusselt number distributions on the center building (Fig. 4.1) under realistic wall heating. The non-dimensional parameter σ is defined for measuring distance along building walls in the peripheral directions, which is the distance from the South-West corner of the building moving around the building walls in the clockwise direction (Fig. 4.15). CHTC is then averaged in the vertical direction.

In general CHTC is larger in the west (windward) wall compared to east (leeward) wall, but the difference depends on the ToD. For example, when the windward wall is heated (1400 - 1800 PST), the associated buoyancy near the heated wall, in

addition to the enhanced vortex strength due to the lower pressure gradient inside the canyon, results in the largest CHTC at the windward wall, while reducing the CHTC at the leeward wall. North and south walls have exhibit higher CHTC since the velocity is higher in the stream-wise canyon. A diurnal cycle is evident where ToDs with similar solar zenith angles and thus similar south wall insolation (e.g. 0800 and 1600) exhibit similar normalized CHTC on the South wall.

Convective Heat Transfer Coefficient (CHTC) at the roof surface (not shown) is also influenced by the horizontal and vertical Richardson number (Ri_h and Ri_v, respectively). The CHTC at roof for neutral, 0600, and 1800 PST simulations is smaller than at 1200 PST. Similarly, Nusselt number at roof level is higher for the windward heating cases (positive Ri_h at 1400 and 1600 PST) compared to leeward heating (negative Ri_h at 0800 and 1000 PST). For all cases, there is a local maximum in CHTCs at the upwind edge of the roof surface, where there is a localized high velocity.

4.4.5 Street Canyon Ventilation and Determinants of Dispersion

In this section, we examine the effect of non-uniform heating on air ventilation of the urban canyon. The concept of Air Exchange Rate (ACH) was introduced by Liu et al [44] and calculated as the area-weighted average of vertical velocity fluctuations at roof-level. The removal or entry of air is indicated by positive (ACH+) or negative (ACH-) air exchange rate, based on the direction of the fluctuating vertical velocity. In 2D street canyons, roof-level ACH+ and ACH- balance due to the zero net vertical flux across the top of the street canyon. For 3D street canyons, Sun et al [69] observed

a balance of positive and negative ACH in each ventilating face in the absence of buoyant forcing. However, when considering the asymmetrical thermal forcing of street canyons during daytime, air exchange through the different ventilating faces of the building canyon is likely unbalanced and unsteady (please refer to Figure 4.11 and the explanation on flow field in the horizontal cross section in section 4.4.3). Applying kinetic (mass) balance in the 3D street canyon, 3D-ACH is defined by sum of air exchange rates along the top and sides of the canyon as

$$\overline{<\mathrm{ACH}>} = \overline{<\mathrm{ACH_{top}}>} + \overline{<\mathrm{ACH_{sides}}>} \ , \tag{4.4}$$

where the overbar represents temporal averaging and the brackets spatial averaging as

$$<\mathrm{ACH_{top}}> = \frac{\int\int w_{+}\mathrm{d}x\mathrm{d}y}{A_{top}} \ , \tag{4.5}$$

$$<\mathrm{ACH_{side\pm}}> = \frac{\int\int v_{\pm}\mathrm{d}x\mathrm{d}z}{A_{side}} \ . \tag{4.6}$$

Here only velocities exiting the canyon are considered, i.e. w_{+} are positive vertical velocities along the top plane and according to the orientation of the side plane, the sign of spanwise velocity (v) differs to represent air removal from the canyon. $A_{\mathrm{top}} = A_{\mathrm{side}} = H^2$ are the areas of top and side of the urban canyon (Fig. 4.16). To analyze the relative effects of mean flow and fluctuations on air removal from the building canyon, ACH is calculated both using the velocity and local velocity fluctuations (e.g. $v' = v - \overline{v}$) and referred to as $\mathrm{ACH_w}$ and $\mathrm{ACH_{w'}}$, respectively.

As additional measures of dispersion, turbulent kinetic energy (TKE) and kinetic energy are calculated and averaged over the cross-stream canyon.

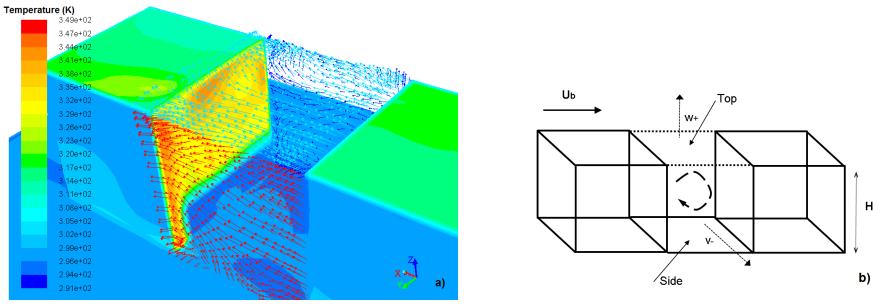

Figure 4.16: a) Contour of instantaneous temperature on urban surfaces (colorbar), overlaid by velocity vectors at the top and the side planes of the cross-stream canyon building space. Velocity vectors are colored based on their ventilating face. b) A sketch of the variables used to calculate the air exchange rates between the cross-stream canyon and the surrounding atmosphere.

$$<\text{TKE}> = \frac{\int\int\int (u'^2 + v'^2 + w'^2)\mathrm{d}x\mathrm{d}y\mathrm{d}z}{\text{V}_{\text{BC}}} \tag{4.7}$$

$$<\text{KE}> = \frac{\int\int\int (u^2 + v^2 + w^2)\mathrm{d}x\mathrm{d}y\mathrm{d}z}{\text{V}_{\text{BC}}} \tag{4.8}$$

V_{BC} in the above equations is the volume of the space between two buildings.

Figure 4.17 shows the variation of air exchange rate and kinetic energy with time, normalized with U_b. In comparison with the neutral case (N), thermal forcing generally increases the ACH, but by less than 10% and ACH is actually smaller at 1200 PST. The air exchange rate induced by velocity fluctuations ($ACH_{w'}$) is only 10% smaller than the total air exchange rate (ACH_w), indicating the dominant effect of turbulence on ventilation from the street canyon. Air removal from the building canyon is enhanced for leeward heating compared to windward heating (positive Ri_h). From 0600 to 1000 PST, when the strength of leeward heating increases and transition to ground heating occurs, ACH and TKE increase. Considering different ventilation faces during these hours (Fig. 4.18), most of the air is ventilated through the the top

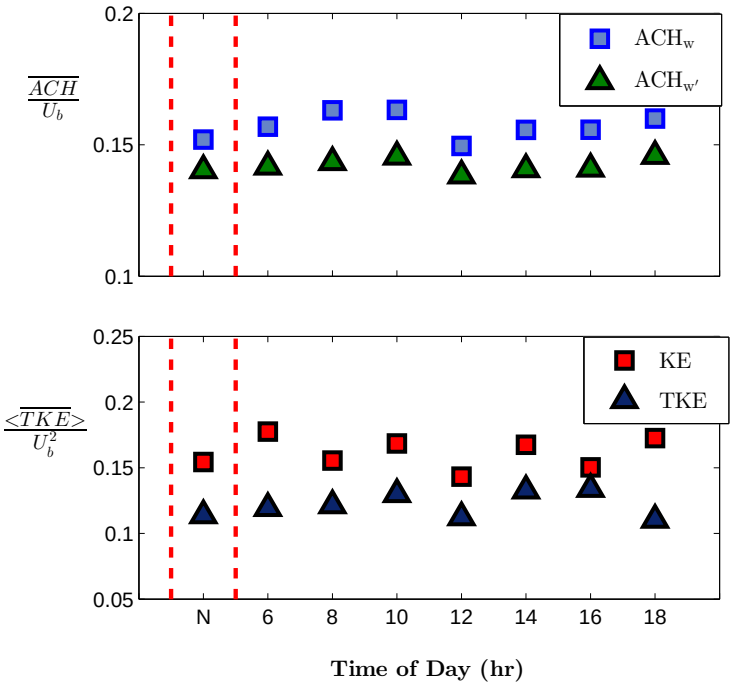

Figure 4.17: Total Normalized Air Exchange Rate at all ventilating surfaces (top) and Turbulent Kinetic Energy (bottom) in the building canyon as a function of ToD. The neutral case (N) is shown as a reference and separated with red dashed lines.

plane (at roof-level), while the north plane (side plane at positive y) is the lowest due to heating of air in the streamwise canyon adjacent to the north wall as described in Section 4.4.3. There is a significant ACH decrease at 1200 PST when the leeward heating effect is removed, and the roof heating is enhanced. The decrease in ACH_w at the top plane shows the effect of roof heating on building canyon air removal (Fig. 4.18). Similarly, air removal from the south ventilation plane is decreased since south facing wall is warmer at 1200 PST (Fig. 4.8). Thermally induced and mechanically induced forcing are in opposite directions in the windward heating cases which explains the lower value of ACH at 1400 PST compared to 1000 PST. As the strength of windward heating and the area ratio of the wall exposed to direct sunlight decreases from 1400 to 1800 PST, ACH increases.

Figure 4.17 (bottom) shows turbulent kinetic energy (<TKE>) and kinetic

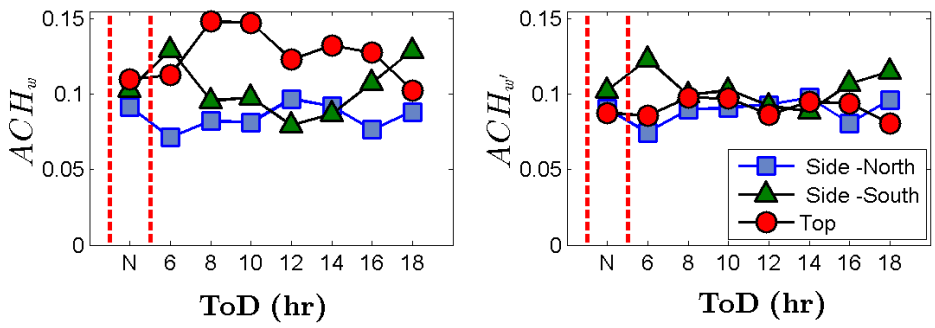

Figure 4.18: Air Exchange Rate at different ventilation surfaces of the building canyon as a function of ToD. Left: Total time-averaged ACH. Right: Time-averaged ACH induced by velocity fluctuations. The neutral case (N) is shown as a reference and separated with red dashed lines.

energy ($<$KE$>$) integrated over the volume between buildings. The magnitude of TKE for the windward heating cases is slightly higher as buoyancy opposes momentum forcing at the windward wall (Fig. 4.14) creating a intermittent flow patterns. The increase in TKE from the neutral case to 1000 PST can be explained by the increase in the surface heating and buoyancy-induced turbulence. The effect of TKE induced by roof heating is expected to have significant effects on building canyon TKE at near-solar-noon hours when roof is uniformly heated. TKE is not correlated with the orientation of the heated wall, rather it depends on the strength of overall wall heating in the building canyon. Kinetic energy does not follow the same pattern as ACH.

4.5 Conclusions

A three dimensional configuration of a compact urban environment is simulated with realistic surface heating. Simulations are performed for a clear summer day at a latitude of 33°N and the differential thermal forcing in the building canyon is parameterized through a new potentially universal dimensionless number.

In order to examine the validity of numerical modeling in representing the flow, performance of several turbulence models are compared with the wind tunnel experiment by Meinders [59]. Similar to Xie and Castro [70], this study concludes that Large Eddy Simulations (LES) performs well in resolving turbulent fluctuations in and above the urban-like obstacles. Reynolds-averaged Navier-Stokes (RANS) and Detached Eddy Simulation (DES) models are however shown to be inadequate, especially in representing the turbulent parameters within the canopy. Additionally, the correction of common but non-physical accumulation of heat in the periodic boundary conditions is performed by a constant inflow temperature boundary condition. Achieving a desired air setpoint temperature in the domain while allowing the flow and thermal field to evolve dynamically requires further research; a possible solution could be to update the heat source/sink term at the top boundary dynamically according to the surface heat flux.

The significance of considering realistic boundary conditions is emphasized in this paper. In summary, two factors influence the flow under realistic conditions: A) the three-dimensional geometry of the building canyon as opposed to 2D canyons with infinitely long width in the spanwise direction: The temperature gradient and therefore air exchange in the spanwise direction is shown to modify the canyon vortex significantly. For example, for a canyon aspect ratio of one, the center of the canyon vortex is above $z/H = 0.75$ for our 3D simulations throughout the day, while reported to be at the center height for the 2-D canyon with the same aspect ration (AR=1). Additionally, the formation of the secondary vortex in the windward heating cases is not observed, which can also be attributed to flow forcing in the spanwise direction. B) the consideration of three-dimensional thermal forcing in the span-wise and stream-

wise canyon: Walls and ground surfaces undergo different patterns of shaded and sunlit areas during the day, therefore more than one urban surfaces is often heated. In simplified uniform heating scenarios studied previously, the effect of multiple surface heating as well as heating in the streamwise canyon are often neglected, while we show that spatial patterns of surface heating generate horizontal temperature and pressure gradients in and above the canyon, influencing the strength of the canyon vortex. For example, canyon ground heating has received wide attention in wind tunnel experiments (such as Allegrini et al [22] and Uehara et al [11]) and numerical modeling (such as Kim and Baik [17] and Li et al [20]). In these papers, ground heating was shown to increase the strength of the main canyon vortex for relatively small aspect ratios (AR=$1 - 1.2$). However, in realistic conditions, roof heating is present with ground heating and we observe a decrease of vortex strength instead, presumably because of horizontal temperature gradients at the roof level. Similarly, the variation of air exchange rate at different ventilating faces demonstrate the significance of combined heating of windward or leeward walls, with roof and north-south walls heating. s been applied frequently in categorizing the vortex structure inside the canyon with aspect to atmospheric stability and vertical wind shear. In addition to the vertical stratification, the horizontal temperature gradient creates buoyant forcing in the street canyon. Therefore buoyancy effect arising from ground surface heating and the resulting Richardson number are insufficient to describe atmospheric instability. Additionally, the geometry of the roughness was shown to influence the vortex formation and the relative importance of inertia to buoyancy forcing. Therefore, a second buoyancy parameter (Ri_h) is introduced that quantifies the orientation of wall heating with respect to the wind, and the horizontal temperature difference inside

the canyon. while the canyon aspect ratio appears in the definition of Ri_h the effect of geometry is not studied in the present paper, and an analysis of the related similarity is left for future work. Also, the flow structure in a vertical plane through the canyon center is not significantly affected by leeward versus windward surface heating.

Street canyon ventilation characterizes the amount of air entering or leaving the building canyon which has implications for air quality, especially dispersion of automobile emissions. Strong roof heating at 1200 PST decrease the total ACH, while wall heating enhances the air removal for leeward and windward heating (in order of importance). Velocity fluctuations at ventilating faces is shown to be the primary mean of air removal, indicating the dominant effect of turbulence on ventilation from the street canyon. Under three-dimensional thermal forcing, air exchange through the spanwise direction is significant (compared to roof ventilation) and exhibits asymmetrical behavior in north and south faces with ToD.

Air exchange from the street canyon is shown to be a function of horizontal temperature gradient. Therefore in a non-idealized configuration of buildings, the orientation of the street canyon can significantly affect the air exchange during daytime. For the range of Richardson numbers studied here (small vertical stratification since large roof heating and high wind speed counteract floor heating, and large horizontal variability during the day) the ACH is enhanced during periods when wall heating dominates, suggesting the north-south canyons would feature enhanced removal of pollutant.

Acknowledgments

The text and data in chapter 4, in full, is a reprint of the material as it appears in "Realistic solar heating in urban areas: Air exchange and street-canyon ventilation", Nazarian, Negin; Kleissl, Jan, *Building and Environment*, 95 (2016), 75-93. The dissertation author is the primary investigator and author of this article.

Bibliography

[1] Gerhard K Heilig. World urbanization prospects: the 2011 revision. *United Nations, Department of Economic and Social Affairs (DESA), Population Division, Population Estimates and Projections Section, New York*, 2012.

[2] Helmut E Landsberg. *The urban climate*, volume 28. Academic Press, 1981.

[3] Timothy R Oke. Review of urban climatology, 1968-1973. 1974.

[4] Timothy R Oke. Review of urban climatology, 1973-1976. 1979.

[5] Timothy R Oke. *Boundary layer climates*. Routledge, 2002.

[6] Haider Taha. Urban climates and heat islands: albedo, evapotranspiration, and anthropogenic heat. *Energy and Buildings*, 25(2):99–103, 1997.

[7] Y Nakamura and TR Oke. Wind, temperature and stability conditions in an east-west oriented urban canyon. *Atmospheric Environment (1967)*, 22(12):2691–2700, 1988.

[8] Jean-François Sini, Sandrine Anquetin, and Patrice G Mestayer. Pollutant dispersion and thermal effects in urban street canyons. *Atmospheric Environment*, 30(15):2659–2677, 1996.

[9] Yasushi Sakakibara. A numerical study of the effect of urban geometry upon the surface energy budget. *Atmospheric Environment*, 30(3):487–496, 1996.

[10] Jae-Jin Kim and Jong-Jin Baik. A numerical study of thermal effects on flow and pollutant dispersion in urban street canyons. *Journal of applied meteorology*, 38(9):1249–1261, 1999.

[11] Kiyoshi Uehara, Shuzo Murakami, Susumu Oikawa, and Shinji Wakamatsu. Wind tunnel experiments on how thermal stratification affects flow in and above urban street canyons. *Atmospheric Environment*, 34(10):1553–1562, 2000.

[12] Rizwan Ahmed Memon, Dennis YC Leung, and Chun-Ho Liu. Effects of building aspect ratio and wind speed on air temperatures in urban-like street canyons.

Building and Environment, 45(1):176–188, 2010.

[13] Neda Yaghoobian, Jan Kleissl, and E Scott Krayenhoff. Modeling the thermal effects of artificial turf on the urban environment. *Journal of Applied Meteorology and Climatology*, 49(3):332–345, 2010.

[14] Neda Yaghoobian and Jan Kleissl. Effect of reflective pavements on building energy use. *Urban Climate*, 2:25–42, 2012.

[15] Negin Nazarian and Jan Kleissl. CFD simulation of an idealized urban environment: Thermal effects of geometrical characteristics and surface materials. *Urban Climate*, 12:141–159, 2015.

[16] Jose Luis Santiago, Omduth Coceal, and Alberto Martilli. How to parametrize urban-canopy drag to reproduce wind-direction effects within the canopy. *Boundary-layer Meteorology*, 149(1):43–63, 2013.

[17] Jae-Jin Kim and Jong-Jin Baik. Urban street-canyon flows with bottom heating. *Atmospheric Environment*, 35(20):3395–3404, 2001.

[18] Bojan Ničeno, ADT Dronkers, and Kemal Hanjalić. Turbulent heat transfer from a multi-layered wall-mounted cube matrix: a large eddy simulation. *International journal of heat and fluid flow*, 23(2):173–185, 2002.

[19] A Kovar-Panskus, L Moulinneuf, E Savory, A Abdelqari, J-F Sini, J-M Rosant, A Robins, and N Toy. A wind tunnel investigation of the influence of solar-induced wall-heating on the flow regime within a simulated urban street canyon. *Water, Air and Soil Pollution: Focus*, 2(5-6):555–571, 2002.

[20] Xian-Xiang Li, Rex E Britter, Leslie K Norford, Tieh-Yong Koh, and Dara Entekhabi. Flow and pollutant transport in urban street canyons of different aspect ratios with ground heating: large-eddy simulation. *Boundary-layer meteorology*, 142(2):289–304, 2012.

[21] Seung-Bu Park, Jong-Jin Baik, Siegfried Raasch, and Marcus Oliver Letzel. A large-eddy simulation study of thermal effects on turbulent flow and dispersion in and above a street canyon. *Journal of Applied Meteorology and Climatology*, 51(5):829–841, 2012.

[22] Jonas Allegrini, Viktor Dorer, and Jan Carmeliet. Wind tunnel measurements of buoyant flows in street canyons. *Building and Environment*, 59:315–326, 2013.

[23] Roland B Stull. *An introduction to boundary layer meteorology*, volume 13. Springer Science & Business Media, 1988.

[24] Neda Yaghoobian and Jan Kleissl. An improved three-dimensional simulation of the diurnally varying street-canyon flow. *Boundary-Layer Meteorology*, 153(2):251–276, 2014.

[25] N Ito. Field experiment study on the convective heat transfer coefficient on exterior surface of a building. *ASHRAE Trans.;(United States)*, 78, 1972.

[26] Steve Sharples. Full-scale measurements of convective energy losses from exterior building surfaces. *Building and Environment*, 19(1):31–39, 1984.

[27] Dennis Loveday and Ahmad Taki. Convective heat transfer coefficients at a plane surface on a full-scale building facade. *International Journal of Heat and Mass Transfer*, 39(8):1729–1742, 1996.

[28] Aya Hagishima and Jun Tanimoto. Field measurements for estimating the convective heat transfer coefficient at building surfaces. *Building and Environment*, 38(7):873–881, 2003.

[29] Y Liu and Douglas John Harris. Full-scale measurements of convective coefficient on external surface of a low-rise building in sheltered conditions. *Building and Environment*, 42(7):2718–2736, 2007.

[30] Anders Nottrott, Shiho Onomura, Atsushi Inagaki, Manabu Kanda, and Jan Kleissl. Convective heat transfer on leeward building walls in an urban environment: measurements in an outdoor scale model. *International Journal of Heat and Mass Transfer*, 54(15):3128–3138, 2011.

[31] Hajime Nakamura, Tamotsu Igarashi, and Takayuki Tsutsui. Local heat transfer around a wall-mounted cube in the turbulent boundary layer. *International Journal of Heat and Mass Transfer*, 44(18):3385–3395, 2001.

[32] Aya Hagishima, Jun Tanimoto, and Ken-ich Narita. Intercomparisons of experimental convective heat transfer coefficients and mass transfer coefficients of urban surfaces. *Boundary-Layer Meteorology*, 117(3):551–576, 2005.

[33] John Palyvos. A survey of wind convection coefficient correlations for building envelope energy systems modeling. *Applied Thermal Engineering*, 28(8):801–808, 2008.

[34] Thijs Defraeye, Bert Blocken, and Jan Carmeliet. Convective heat transfer coefficients for exterior building surfaces: Existing correlations and CFD modelling. *Energy Conversion and Management*, 52(1):512–522, 2011.

[35] Marcelo G Emmel, Marc O Abadie, and Nathan Mendes. New external convective heat transfer coefficient correlations for isolated low-rise buildings. *Energy and*

Buildings, 39(3):335–342, 2007.

[36] Bert Blocken, Thijs Defraeye, Dominique Derome, and Jan Carmeliet. High-resolution CFD simulations for forced convective heat transfer coefficients at the facade of a low-rise building. *Building and Environment*, 44(12):2396–2412, 2009.

[37] Thijs Defraeye, Bert Blocken, and Jan Carmeliet. CFD analysis of convective heat transfer at the surfaces of a cube immersed in a turbulent boundary layer. *International Journal of Heat and Mass Transfer*, 53(1):297–308, 2010.

[38] Habibollah Heidarzadeh, Mousa Farhadi, and Kurosh Sedighi. Convective heat transfer over a wall mounted cube using large eddy simulation. *CFD Letters*, 4(2):80–92, 2012.

[39] Hazim B Awbi. Calculation of convective heat transfer coefficients of room surfaces for natural convection. *Energy and Buildings*, 28(2):219–227, 1998.

[40] Ian Beausoleil-Morrison and Paul Strachan. On the significance of modelling internal surface convection in dynamic whole-building simulation programs. *ASHRAE Transactions*, 105(2):929–940, 1999.

[41] Ioannis Panagiotou, Marina K-A Neophytou, David Hamlyn, and Rex E Britter. City breathability as quantified by the exchange velocity and its spatial variation in real inhomogeneous urban geometries: An example from central london urban area. *Science of the Total Environment*, 442:466–477, 2013.

[42] Chun-Ho Liu and Mary C Barth. Large-eddy simulation of flow and scalar transport in a modeled street canyon. *Journal of Applied Meteorology*, 41(6):660–673, 2002.

[43] Chun-Ho Liu, Mary C Barth, and Dennis YC Leung. Large-eddy simulation of flow and pollutant transport in street canyons of different building-height-to-street-width ratios. *Journal of Applied Meteorology*, 43(10):1410–1424, 2004.

[44] Chun-Ho Liu, Dennis YC Leung, and Mary C Barth. On the prediction of air and pollutant exchange rates in street canyons of different aspect ratios using large-eddy simulation. *Atmospheric Environment*, 39(9):1567–1574, 2005.

[45] Xian-Xiang Li, Chun-Ho Liu, and Dennis YC Leung. Development of a k–ε model for the determination of air exchange rates for street canyons. *Atmospheric environment*, 39(38):7285–7296, 2005.

[46] Xiaomin Xie, Chun-Ho Liu, Dennis YC Leung, and Michael KH Leung. Characteristics of air exchange in a street canyon with ground heating. *Atmospheric Environment*, 40(33):6396–6409, 2006.

[47] WC Cheng, Chun-Ho Liu, and Dennis YC Leung. On the correlation of air and pollutant exchange for street canyons in combined wind-buoyancy-driven flow. *Atmospheric Environment*, 43(24):3682–3690, 2009.

[48] Xian-Xiang Li, Chun-Ho Liu, and Dennis YC Leung. Numerical investigation of pollutant transport characteristics inside deep urban street canyons. *Atmospheric Environment*, 43(15):2410–2418, 2009.

[49] Jong-Jin Baik, Yoon-So Kang, and Jae-Jin Kim. Modeling reactive pollutant dispersion in an urban street canyon. *Atmospheric Environment*, 41(5):934–949, 2007.

[50] Y Toparlar, B Blocken, P Vos, GJF van Heijst, WD Janssen, T van Hooff, H Montazeri, and HJP Timmermans. Cfd simulation and validation of urban microclimate: A case study for bergpolder zuid, rotterdam. *Building and Environment*, 83:79–90, 2015.

[51] Hong Chen, Ryozo Ooka, Kazuya Harayama, Shinsuke Kato, and Xiaofeng Li. Study on outdoor thermal environment of apartment block in shenzhen, china with coupled simulation of convection, radiation and conduction. *Energy and Buildings*, 36(12):1247–1258, 2004.

[52] Rajagopalan Priyadarsini, Wong Nyuk Hien, and Cheong Kok Wai David. Microclimatic modeling of the urban thermal environment of singapore to mitigate urban heat island. *Solar energy*, 82(8):727–745, 2008.

[53] Xiaoshan Yang, Lihua Zhao, Michael Bruse, and Qinglin Meng. Evaluation of a microclimate model for predicting the thermal behavior of different ground surfaces. *Building and Environment*, 60:93–104, 2013.

[54] Ian D Stewart and Tim R Oke. Local climate zones for urban temperature studies. *Bulletin of the American Meteorological Society*, 93(12):1879–1900, 2012.

[55] O Coceal, TG Thomas, IP Castro, and SE Belcher. Mean flow and turbulence statistics over groups of urban-like cubical obstacles. *Boundary-Layer Meteorology*, 121(3):491–519, 2006.

[56] EH Chui and GD Raithby. Computation of radiant heat transfer on a nonorthogonal mesh using the finite-volume method. *Numerical Heat Transfer*, 23(3):269–288, 1993.

[57] Ansys Fluent. 12.0 theory guide. *Ansys Inc*, 5, 2009.

[58] H Werner and H Wengle. Large-eddy simulation of turbulent flow over and around a cube in a plate channel. In *Turbulent Shear Flows 8*, pages 155–168.

Springer, 1993.

[59] Erwin Rinaldo Meinders. *Experimental study of heat transfer in turbulent flows over wall-mounted cubes.* PhD thesis, Delft University of Technology, 1998.

[60] Massimo Germano, Ugo Piomelli, Parviz Moin, and William H Cabot. A dynamic subgrid-scale eddy viscosity model. *Physics of Fluids A: Fluid Dynamics (1989-1993)*, 3(7):1760–1765, 1991.

[61] Mikhail L Shur, Philippe R Spalart, Mikhail Kh Strelets, and Andrey K Travin. A hybrid RANS-LES approach with delayed-des and wall-modelled LES capabilities. *International Journal of Heat and Fluid Flow*, 29(6):1638–1649, 2008.

[62] Philippe R Spalart, S Deck, ML Shur, KD Squires, M Kh Strelets, and A Travin. A new version of detached-eddy simulation, resistant to ambiguous grid densities. *Theoretical and Computational Fluid Dynamics*, 20(3):181–195, 2006.

[63] JL Santiago, ES Krayenhoff, and A Martilli. Flow simulations for simplified urban configurations with microscale distributions of surface thermal forcing. *Urban Climate*, 9:115–133, 2014.

[64] Harindra JS Fernando, Dragan Zajic, Silvana Di Sabatino, Reneta Dimitrova, Brent Hedquist, and Ann Dallman. Flow, turbulence, and pollutant dispersion in urban atmospheres. *Physics of Fluids*, 22(5):051301, 2010.

[65] Ann Dallman, Sigurdur Magnusson, Rex E Britter, Leslie K Norford, Dara Entekhabi, and Harindra JS Fernando. Conditions for thermal circulation in urban street canyons. *Building and Environment*, 2014.

[66] Sigurdur Magnusson, Ann Dallman, Dara Entekhabi, Rex E Britter, Harindra JS Fernando, and Leslie K Norford. On thermally forced flows in urban street canyons. *Environmental Fluid Mechanics*, pages 1–15, 2014.

[67] Xiaoming Cai. Effects of differential wall heating in street canyons on dispersion and ventilation characteristics of a passive scalar. *Atmospheric Environment*, 51:268–277, 2012.

[68] Brian Offerle, Ingegärd Eliasson, CSB Grimmond, and Björn Holmer. Surface heating in relation to air temperature, wind and turbulence in an urban street canyon. *Boundary-layer Meteorology*, 122(2):273–292, 2007.

[69] Long Sun, Anders Nottrott, and Jan Kleissl. Effect of hilly urban morphology on dispersion in the urban boundary layer. *Building and Environment*, 48:195–205, 2012.

[70] Zheng-Tong Xie and Ian P Castro. Large-eddy simulation for flow and dispersion in urban streets. *Atmospheric Environment*, 43(13):2174–2185, 2009.

Chapter 5

Realistic Urban Heating and Pollutant Concentration: Air Quality and City Breathability

5.1 Introduction

Two classes of factors determine the pollution concentration in urban environments: a) the nature of relevant emissions, and b) the state of the atmosphere in and above the street canyon [1]. In the first category, the vehicular exhaust is the primary and dominant source of emission which is subjected to a substantial growth due to the increasing rate in urbanization and modernization[1]. The dispersion, transformation and eventual removal of pollutants from the air is then governed by atmospheric motion and stability.

In summary, the major parameters affecting street-scale flow, thermal and dispersion fields are local ambient conditions (wind speed and direction), roughness

morphology (building height, street width, and roof shape), and thermal stratification (solar radiation and orientation, skyview factor, anthropogenic heats and building envelope energy). When considering the traffic pollution dispersion, the vehicle movement (size, number, and frequency) and plume buoyancy is also of importance. The complexity of interaction between these mechanisms in urban environments motivated numerous analyses through different methodologies, including field observation, wind-tunnel experiments and numerical simulations. Major field campaign studies include full-scale measurements by DePaul and Sheih [2], Nakamura and Oke [3], Qin and Kot [4], Berkowicz et al. [5] and xie et al [6]. Additionally, the Joint Urban 2003 field study (centered in the Central Business District (CBD) of Oklahoma City) gathered data over the course of 34 days with more than 20 organizations involved [7], and the "Dispersion of Air Pollution and its Penetration into the Local Environment" (DAPPLE) project was conducted in Westminster, London, executing five field campaigns over the course of 2003-2008 [8]. These measurements are widely used for evaluating computational and empirical dispersion models. However, the complexity of real-world settings, such as convoluted roughness element, vehicle-induced turbulence, anthropogenic heats and the sudden events caused by human activities restricts general conclusions from the data.

Additionally, wind-tunnel experiments (Meroney and Pavageau [9], Kastner-Klein and Plate [10], Baker and Hargreaves [11], Kastner-Klein and Fedorovich [12], Kastner-Klein and Rotach [13]) and Computation Fluid Dynamic (CFD) simulation of dispersion in urban-like geometries (Li et al. [14], Cheng and Liu [15], Park et al. [16] and Tan et al. [17]) have been widely adopted to study pollutant transport in street canyons and can be used to analyze the effect of various parameters (e.g. wind

speed, wind direction, turbulence levels) separately

Complex morphology of real urban areas impose variety of challenges for accurate simulation of flow field and dispersion. Two-dimensional simplified morphology is often used for CFD simulation of street canyons, which is shown to reproduces more accurate sky-view factors in the highly dense neighborhoods, specifically in European cities [18]. However, for smaller λ_p (built to non-built area ratio) and building height variability, often seen in American cities and compact residential/industrial neighborhoods, three-dimensional representation of urban morphology is preferred. In addition to flow modifications, urban surface heating is also significantly influenced by the 3D morphology of the urban street canyon. Nazarian and Kleissl [19] showed that in the 3D urban environment, uniform heating of merely one surface is unlikely and the flow, and consequently the pollution removal to the free stream, is affected by the superposition of wall, roof and ground heating.

Thermal forcing plays an important role in scalar dispersion patterns in urban streets by inducing different turbulence coherent structures or just by increasing the activity of turbulent eddies [3, 20, 21]. Until recently, simplified and uniform heating of one urban surface (often ground) was considered as the representation of solar heating [16, 22–25]. Few recent studies considered the effect of 3D realistic heating, analyzing the energy balance components of urban facets [26], flow and turbulence in street canyon [19, 27] and drag coefficient of urban roughbess for mesoscale parametrization [28]. However, to date the effect of realistic surface heating on dispersion is not evaluated.

The realistic heating of urban surfaces in starting to receive attention in the literature, yet there is no universal and comprehensive way of characterizing the

flow in the street canyon under stable condition. Nazarian and Kleissl showed that bulk Richardson number gives insufficient information regarding flow characteristics and parametarized the differential heating into directional thermal forcing defined by horizontal and vertical Richardson numbers. In this paper, we aim to answer several questions regarding this characterization method: Is the flow field and turbulence in the street canyon more sensitive to the total surface heating (Ri_b), vertical instability inside the canyon (Ri_v), or horizontal heating of urban surfaces (Ri_h) due to solar insolation? and does thermal, flow and dispersion fields respond similarly to the proposed characterization method?

To address these questions, a detailed indoor-outdoor building energy model (TUF-IOBES) is employed to compute heat fluxes from street and building surfaces, which are then used as boundary condition for a PArallelized Large-Eddy Simulation Model (PALM). In comparison with previous studies, our model considers the transient non-uniform surface heating caused by solar insolation and inter-building shadowing, while coupling the indoor-outdoor heat transfer, flow field and passive pollution dispersion. Additionally, LES is shown to be superior in its representation of flow field statistics [19] and therefore used for improved accuracy. Series of fluid flow and thermal field simulations are then performed for an idealized, compact mid-rise urban environment with no vegetation and the pollution dispersion and exchange behavior in and above buildings is investigated. The study is divided into two parts, first analyzing the detailed flow and dispersion field under 3D realistic heating, while the second part is focused on the practical relevance of these findings on analyzing the effect of urban design on city breathability and climate.

The following sections describe the methodology and structure of the presented

work. Numerical tools and the simulation setup are described in Section 5.2 followed by the discussion on the spacio-temporal averaging technique employed in this study 5.2.4. The characterization of the flow and thermal field is examined and their degree of universality is evaluated in section 5.3 as a function of two dimensionless number. Subsequently, spatial distribution of dimensionless concentration and turbulent fluxes are investigated as varied with the prescribed characterization method in Section 5.4. Higher order statistics of turbulent transfer are analyzed in Section 5.4.2 by means of quadrant analysis. Additionally, Air and Pollutant Exchange rate from the ventilating faces are analyzed at different stability conditions to evaluate the air quality in the street canyon.

5.2 Methods

Large Eddy Simulations are used as a superior method for evaluating turbulence characteristics and dispersion behavior in the street canyon. The PArallelized Large-eddy simulation Model (PALM) developed at the Leibniz University of Hannover (Raasch et al. [29] and Letzel et al. [30]) is employed with realistic thermal boundary conditions extracted from Temperature of Urban Facets Indoor-Outdoor Building Energy Simulation [31]. TUF-IOBES as well as the velocity and temperature fields of PALM were validated by Yaghoobian and Kleissl [31] and Park et al. [16] respectively. Yaghoobian et al. [27] validated the coupling method against the wind-tunnel experiment of Kovar-Panskus et al. [32] and demonstrated that one-way coupling of TUF-IOBES surface heat flux to PALM can accurately account for the effects of the realistic temperature distribution over urban canopy surfaces. For the purpose of this study, the prognostic equation for passive scalars is also solved in PALM that was

validated in Park et al. [16].

5.2.1 An Indoor-Outdoor Building Energy Simulator

TUF-IOBES is a building-to-canopy model that simulates indoor and outdoor building surface temperatures and heat fluxes to estimate cooling/heating loads and energy use of buildings in a three-dimensional urban area. The model dynamically solves for indoor and outdoor energy processes, including effects of real weather conditions, indoor heat sources, building and urban material properties, composition of the building envelope (e.g. windows, insulation), and waste heat from air-conditioning systems on urban canopy temperature. At each time step, the indoor and outdoor energy balance processes are coupled. Unlike the gridded energy model for exterior surfaces (outdoor energy balance model similar to [33]), the indoor model computes bulk heat exchange and temperature between surfaces based on subroutines in the ASHRAE Toolkit.

The outdoor surface energy balance consists of net longwave L_{net}, net shortwave S_{net} radiation (accounting for multiple reflections of direct solar radiation and shading), conduction Q_c, and convection Q_h that are solved and enforced for each outdoor patch surface. Direct and diffuse horizontal solar radiation is based on the TMY3 (Typical Meteorological Year 3) forcing data. Downwelling longwave radiation from the sky is based on Browns sky model [34] as implemented in the ASHRAE Toolkit [35], where L_{net} is a function of air and dew point temperatures, cloud cover and cloud height. The transient heat conduction is solved based on Z-transform method utilizing Conduction Transfer Functions (CTFs) and the diffusion equation by Hillel [36] is solved to obtain a sinusoidal temperature boundary condition at the surface and

a constant temperature boundary condition at soil depth. The surface convective heat fluxes are simulated based on the temperature differences between surfaces and canopy air multiplied by a convective heat transfer coefficient based on an empirical model known as the DOE-2 method. Further information on the model, including fenestration model and forcing data can be found in in Yaghoobian and Kleissl [31] and (TUF3D, [33]).

5.2.2 PArallelized Large-eddy simulation Model

The PArallelized Large-eddy simulation Model (PALM) [29, 30]) is employed in this study that solves the filtered, incompressible Boussinesq equations, the 1st law of thermodynamics, the equation for subgrid-scale (SGS) turbulent kinetic energy (TKE) and passive scalar (pollutant) equation. The numerical scheme used are the third-order RungeKutta scheme for time integration and the second-order Piacsek and Williams [37] scheme for advection. The SGS turbulent fluxes are parameterized using the 1.5-order Deardorff [38] scheme which uses SGS-TKE to calculate eddy viscosity. A detailed description of PALM can be found in Letzel et al. [30]. Except for the addition of the passive scalar equation, the simulation setup in this study is the same as that of Yaghoobian et al. [39], further explained in Section 5.2.3.

5.2.3 Boundary Conditions and Simulation Set-up

The schematic of the computational domain is shown in Figure 5.1. All simulations are performed over a 5 by 3 (5 buildings in the x-direction and 3 in y-direction) array of uniformly spaced obstacles with a canyon aspect ratio (canyon height-to-width) of 1. The configuration represents compact low rise urban zone,

corresponding to a roughness plan aspect ratio, $\lambda_p = A_p/A_T$, of 0.29 and frontal aspect ratio, $\lambda_f = A_f/A_T$, of 0.25. A_p , A_f and A_T indicate the plan area, the frontal area and the total area of roughness elements, respectively. Total domain height is 7.4H, where H is the building height (18.3 m). Each building wall has a window fraction of 0.47. The geometry configuration and grid size are chosen according to the series of sensitivity analysis recommended by Yaghoobian et al [39] and the validity of the grid resolution is further investigated for the time-space averaging method 5.2.4. For simplicity, the volume between buildings in the spanwise canyon and stream-wise canyon are referred to as "Building Canyon" (or "BC"), and "Street Canyon" (or "SC"), respectively.

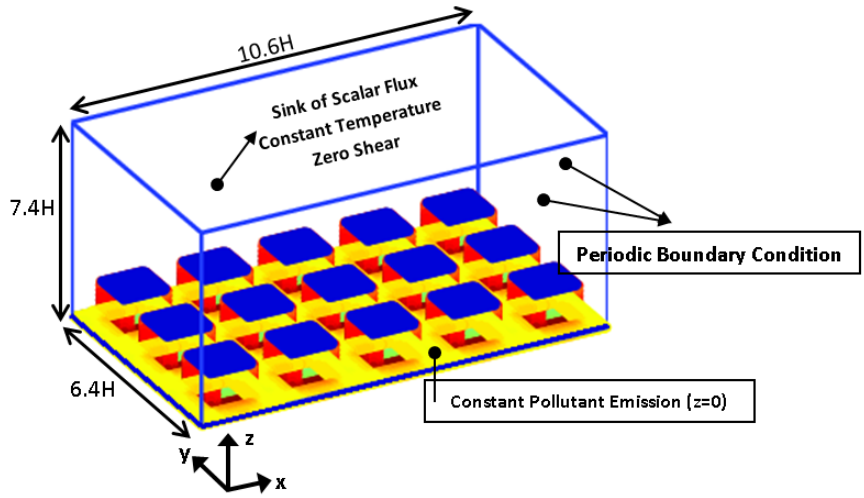

Figure 5.1: Schematic of the computational domain and boundary conditions

Thermal, radiative and material properties of urban surfaces are shown in Table 5.1. Latent heat fluxes are assumed to be zero. Surface heat flux at each grid points from TUF-IOBES are outputted in 15 minutes intervals and temporally interpolated

Table 5.1: Surface radiative and material properties

Surface	Roof	Ground	Walls
Albedo (-)	0.6	0.1	0.3
Emissivity (-)	0.9	0.95	0.9
Roughness length (m)	0.01	0.01	0.01

to PALM. Periodic boundary conditions are used in horizontal directions, conserving mass-flow rate in the streamwise direction. Uniform and constant pollutant emission is prescribed at the ground boundary condition (z=0), representing traffic emission. A constant sink term for scalar flux is imposed as top boundary condition. Using this boundary condition, the integral of the concentration in the whole domain is constant in time, therefore, the ensemble average can be approximated by the time average. Additionally, above the buildings the turbulent flux is nearly constant with height, which is a typical feature for the inertial sublayer (e.g. the upper part of the atmospheric surface layer).

The focus of this study is on unstable atmospheric stratification and the simulations are done for a temperate mid-latitude climate (Boston, Massachusetts with latitude of 42.36°N), while the results can be expanded to various locations and time of the years using the characterization method further explained in Section 5.3. The simulation day is set to clear summer day (8th of July) and the forcing data is extracted from the representative Typical Meteorological Year (TMY3) file.

5.2.4 Time-spatial Averaging Technique

LES explicitly resolves turbulence and simulates one realization of the flow at any time step. Results must be time averaged to obtain statistically significant quantities. Accordingly, the definition of the averaging interval is crucial. A guiding

principle is that, given the regularity of the array and the periodic boundary conditions, the time averaged flow in all the canyons must be identical in a neutral condition without variability in surface heating. However, 30 min averaged velocity fields shows a strong variability between different canyons in the following simulations (Fig. 5.2). To ensure that this behavior is not an artifact of the numerical settings, the choice of the domain size, and the boundary condition used to conserve the flow in horizontal direction was studied, but showed no influence on the variability of the results in the spanwise direction. It is observed that this behavior is due to the formation of roll-like

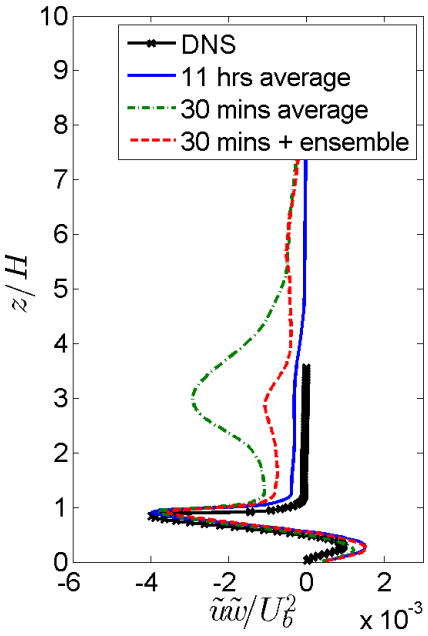

Figure 5.2: Comparison of horizontally-averaged profiles of dispersive stresses ($< \overline{\tilde{u}\tilde{w}} >$) with different averaging intervals with DNS data [40].

circulations with axes in streamwise direction and Coceal et al. [40] with DNS showed that to filter these it is necessary to average over a time period of 200-400 large eddy turnovers. Coceal et al. [40] also analyzed the so-called dispersive stress $< \overline{\tilde{u}\tilde{w}} >$ (Raupach and Shaw [41]) for this time averaging interval, where the time average is represented with an overbar, and the horizontal average with brackets. Accordingly, if

the fluctuation of an instantaneous value ψ from the time-averaged value at the same point is given with ψ', and the deviation of the time-averaged value from the time and space average over the horizontal plane is shown by $\tilde{\psi}$, the total momentum fluxes can be written as

$$<\overline{\mathrm{uw}}>=<\overline{\mathrm{w}}><\overline{\mathrm{u}}> + <\overline{\mathrm{u'w'}}> + <\overline{\tilde{\mathrm{u}}\tilde{\mathrm{w}}}> \tag{5.1}$$

where the last term on the right hand side represent the dispersive stresses that accounts for the transport due to time-avergaed structures smaller than the size of the averaging volume. Therefor, for a sufficiently large time-averaging interval (200-400 large eddy turnover time), the dispersive stresses approaches zero right above the canopy also shown by Coceal et al. [40]. This time interval corresponds to about 11 hours for our setup, however, in the unstable simulation of urban environments, it is not possible to use 11 h as averaging time, since the heat fluxes change significantly following the solar forcing. As a compromise, we divide the computational domain into 15 canyon units shown in Figure 5.2 and combine the 30 mins average, with an average over the units (ensemble average). The 30 mins ensemble average results shows similar flow field in canyons, filtering the variability in the spanwise direction, and a small dispersive stress above the canopy (Fig. 5.2) is seen. The simulation is then repeated for an unstable case with constant heat flux at ground surface and similar to the neutral case, the dispersive stresses above the canyon are reduced with ensemble averaging. Additionally, the point-by-point differences in velocity and temperature of about 0.1 $\mathrm{m\,s^{-1}}$ and 0.2K compared to an 11 h average is observed in the canyon.

5.3 Characterizing Momentum Versus Buoyancy Forcing

In a 3D urban environment with realistic heating, more than one urban surfaces is often heated and the uniform heating of merely one surface is unlikely [19]. Figure 5.3 shows the variation of convective heat flux at different urban facets at the simulation day when the solar noon is approximately at 1200 EDT. The convective heat flux at the roof surface is symmetric around solar noon, whereas Q_h at ground surfaces is higher in the afternoon hours due to the ground thermal storage (Fig. 5.3). Therefore, although solar flux received at east and west walls (leeward and windward, respectively) is symmetric around solar noon, due to the increased longwave radiation exchange between ground and wall surfaces in afternoon hours, Q_h at ground and wall surfaces exhibit larger value after 1200 EDT. Additionally, Q_h at the south wall is predominantly larger than the north wall with maximum heat flux difference occurring at 1330 EDT. Considering the three-dimensional and non-uniform nature of surface heating, it is crucial to break down the total thermal forcing into directional forcing in order to analyze the flow, thermal and dispersion field inside the canyon.

Traditionally, the bulk Richardson number (Ri_b) is used to indicate the atmospheric stability of urban areas, where total surface temperature of urban facets (T_s) is compared to T_a, the free stream wind temperature. Additionally, when analyzing the microclimate of urban streets with ground heating, Ri_v was commonly used to indicate the atmospheric stability due to the the temperature difference in vertical direction

$$Ri_v = \frac{gH}{(U_b^2)} \frac{(\overline{T_H} - \overline{T_g})}{T_a} \ , \tag{5.2}$$

where $g = 9.81$ ms^{-2} is the gravitational acceleration, T_H is the air temperature at roof level, T_g is the temperature of the ground surface inside the building canyon, T_a is the inflow air temperature, and U_b is the bulk wind velocity in the streamwise direction. The definition of Ri_v avoids the use of U_h due to the sharp gradient of velocity at roof level that is not easily controllable (similar to [14] and [24]).

Ri_v alone neglects the horizontal temperature gradient, and falls short in comprehensive characterization of the flow in the cross-stream canyon. Therefore, horizontal Richardson number as defined by Nazarian and Kleissl [42] compares the ratio between thermal forcing ($\frac{\partial F_t}{\partial x}$) and inertial forcing ($\frac{\partial F_m}{\partial z}$), which conveys more information about the directionality of thermal forcing in relationship to the canyon vortex.

Table 5.2: BC and SC stands for Building Canyon (spanwise) and Street Canyon (streamwise), respectively. Values of Ri_h and Ri_v are averaged over the 1800s time interval indicated by the overbar.

$U_b = 0.5\,ms^{-1}$	**AC1**	**AC2**	**NHH**	**OC**
Time of Day (EDT)	0900 - 0930	1100 - 1130	1300 - 1330	1500 - 1530
$\overline{Ri_v}(BC)$	-15.2	-56.1	-72.7	-54.1
$\overline{Ri_h}(BC)$	-33.1	-21.7	0	19.5
$\overline{Ri_v}(SC)$	-44.4	-52.1	-37.4	-7.0
$\overline{Ri_h}(SC)$	-5.4	-13.4	-15.5	-7.9

In the absence of the thermal forcing, the momentum force (F_m) inducing the vortex inside the canyon is ($\frac{\partial \overline{u'w'}}{\partial z}$), while for a sufficiently small bulk velocity,

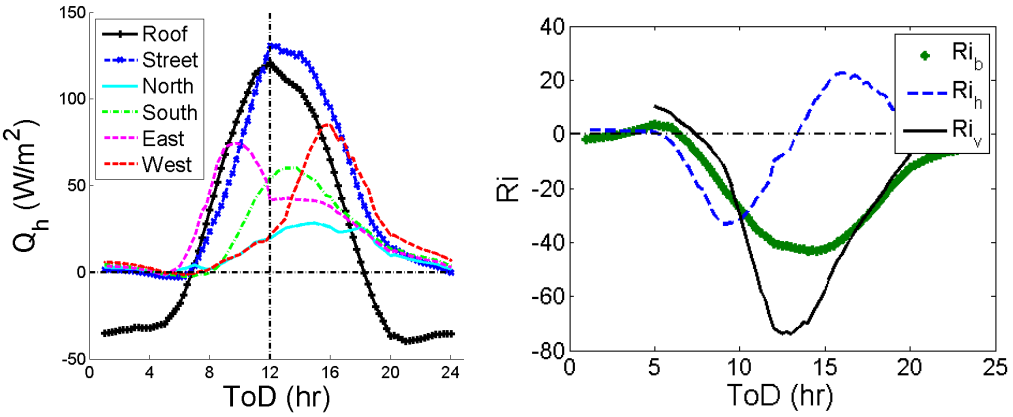

Figure 5.3: for $U_b = 0.5\,\mathrm{ms}^{-1}$.

thermal forcing (F_m) can be written as $g\frac{T_W - T_L}{T_a}$, where T_W and T_L are the averaged surface temperature on windward and leeward walls (here west and east), respectively. Therefore, horizontal Richardson number can be defined by $\mathrm{Ri_h}$ tnat indicates the effect of differential solar heating and also incorporates the effect of canyon aspect ratio H/W.

$$Ri_h = \frac{\partial F_t/\partial x}{\partial F_m/\partial z} = \frac{gH}{U_b^2}.\frac{(\overline{T_L} - \overline{T_W})}{T_a}\frac{H}{W} \tag{5.3}$$

According, the total thermal forcing inside the canyon is divided into directional heatings and their importance compared to momentum forcing is analyzed. The validity of this choice of non-dimensional numbers is demonstrated through simulations with different wind speed and surface radiative properties, but the same sets of Richardson numbers. Overall, similarity of mean and ensemble averaged properties is seen between two cases with same set of Richardson numbers and the local normalized values in two cases are shown to be very close.

In this study the average wind speed in simulation cases is varied from 0.5 to 3 $\mathrm{m\,s}^{-1}$ to span the weakly to strong unstable regimes. This setup results in a wide

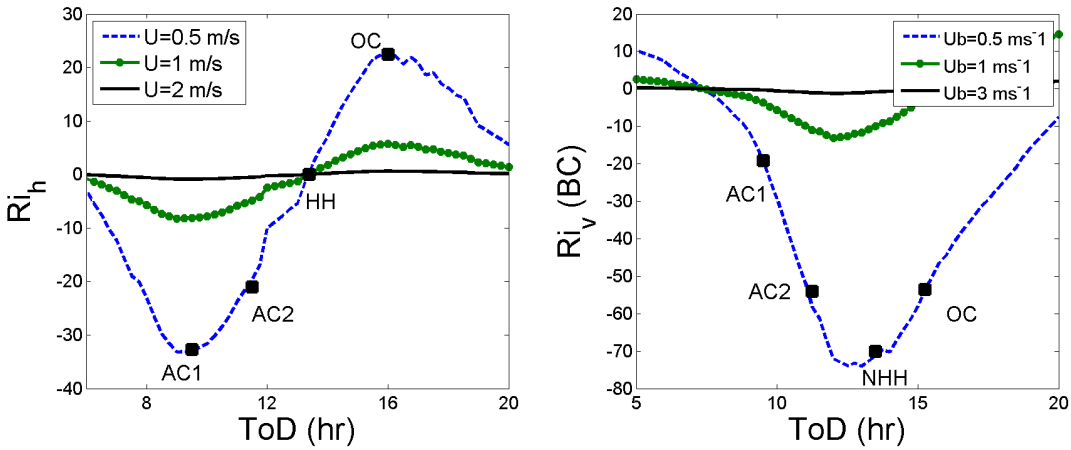

Figure 5.4: Horizontal (Ri_h) and vertical Richardson number (Ri_v) with ToD at different wind speeds.

span of vertical and horizontal Richardson numbers (Figure 5.4) and accordingly the analyses are performed for following conditions (Figure 5.4): a) assisting condition 1, AC1 (0900 - 0930 EDT) with maximum leeward heating occurring inside the canyon, i.e minimum Ri_h ($Ri_h < 0$), and small Ri_v due to the relative roof and ground heating at this hour, (Fig. 5.4), b) assisting condition 2, AC2 (1100-1130 EDT) with significant leeward ($Ri_h < 0$) and ground heating (large negative Ri_v) occurring inside the spanwise canyon, c) opposing condition, OC (1500 - 1530 EDT) when large windward heating occurs, i.e positive Ri_h, combined with roof/ground heating, so that the magnitude of Ri_v is the same as assisting condition, while the sign of Ri_h is different (windward versus leeward heating), and c) no horizontal heating condition, NHH (1300 - 1330 EDT) when both roof and ground surfaces are at maximum heating scenario with the largest Ri_v while Q_h at west and east walls are the same (Fig. 5.4), therefore $Ri_h = 0$. These choice of stability conditions allow us to evaluate and compare the effect of windward versus leeward heating (AC2 vs OC), as well as the importance of vertical versus horizontal temperature gradient (AC1 vs NHH) on

the pollutant concentration and thermal field under realistic 3D heating. It is also worth mentioning that although similar terminology is used for flow characteristic, the realistic consideration of surface heating imposes more complex conditions than opposing and assisting cases previously studied by Cai [43]. For instance, inter-building shading results in combined non-uniform heating of wall and ground surfaces; wall and ground surfaces in the stream-wise canyons are also heated during the day resulting in different set of Richardson numbers in the streamwise canyon; and the absolute value of Ri_v and Ri_h are slightly different when comparing the opposing and assisting conditions.

5.4 Results and Discussions

The analysis is structured as follows. First, the contour plots of flow, temperature and pollutant concentration are investigated at different locations in the stream/span-wise canyons. Additionally, turbulent fluxes of heat, momentum and scalar are investigated to analyze the effect of directional heating on turbulence inside the street canyon, compared with simplified cases of uniform heating (e.g. Li et al. [14] and Cheng and Liu [15]) and 2D street canyons (e.g. Tan et al. [17]). These detailed examinations in Section 5.4.1 further improve our understanding on the effects of three-dimensional heating orientation and intensity (quantified by Richardson numbers) on concentration distribution and the mechanisms involved in pollutant dispersion.

Secondly, the effect of surface heating on turbulent events are analyzed by performing a detailed quadrant analysis (Section 5.4.2). This analysis is performed at three different regions within the building roughness sublayer, identified for a

neutral flow over building roughness by Coceal et al. [40]: 1) within the building canopy, 2) shear layer at rooftop height, and 3) the rough wall flow above the building height. This is an effective method for specifying the frequency of coherent events (such as sweeps and ejections) as opposed to intermittent events (inward and outward interaction), and quantifying their contributions to the total turbulent transport at different positions.

Lastly, "Breathability" in urban environments is analyzed by studying the pollutant concentration distribution and exchange processes in the 3-D geometry. By adopting air quality concepts originally developed for indoor building environments, such as Air and Pollutant Exchange Rate, outdoor ventilation is defined as a measure of city breathability (Section 5.4.3).

5.4.1 Wind, Temperature, and Dispersion Fields

Mean Flow

The contour plots of mean velocity magnitude superimposed by velocity vectors, followed by the plots of dimensionless temperature and pollutant concentration are shown in Figures 5.5 and 5.6 corresponding to two bulk velocity of $U_b = 0.5$ and $3\,\mathrm{m\,s^{-1}}$, respectively. The results are time-averaged over 1800 s and ensemble averaged in the computational domain (5.2) and reported for the assisting (AC), opposing (OC), and no horizontal heating (NHH) conditions, according to thier Richardson numbers described in Section 5.3.

Following observations are made when comparing the vortex formation in the building canyon (BC) at different stability conditions. First, with the increase in U_b from 0.5 to 3 $\mathrm{m\,s^{-1}}$, and therefore decreasing Ri_v for the same heating distribution,

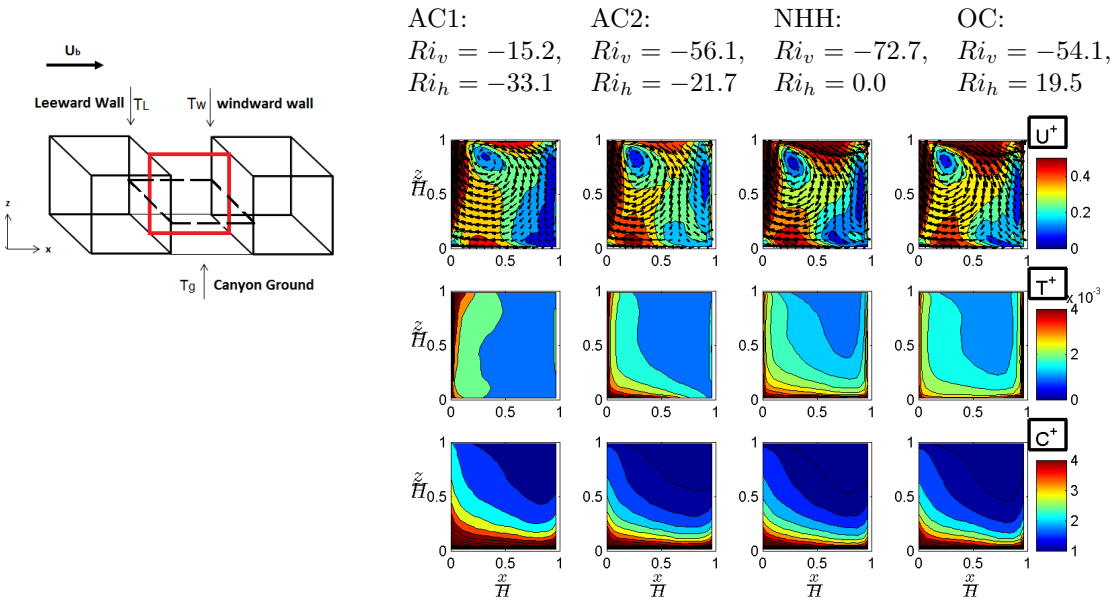

Figure 5.5: Contour plots of flow properties at different studied conditions (Table 5.2) for $U_b = 0.5\,\mathrm{m\,s^{-1}}$ in the vertical plane (x-z) in the center of the building canyon. Contour plots of flow properties at different studied conditions (Table 5.2) for $U_b = 0.5\,\mathrm{m\,s^{-1}}$ in the vertical plane (x-z) in the center of the building canyon. The first row of plots shows the velocity magnitude $(u^2 + v^2 + w^2)^{1/2}$ superimposed by velocity vectors, followed by the contour plots of normalized temperature ($T^+ = \frac{(T-T_{ref})}{Q_h L/U_b}$) and concentration ($C^+ = \frac{(C-C_{ref})}{E/U_b}$), where Q_h and Exu represent total surface heat and concentration flux, respectively, and reference height is chosen to be at $6H$. The results are time averaged over 1800s and ensemble averaged according to Section 5.2.4.

the vortex intensity decreases and the region of low velocity extends deeper in the canyon. Additionally, for the highly unstable case ($U_b = 0.5\,ms^{-1}$ and max(Ri_v) = -72.7), the size of the primary vortex is larger than the height of the building; the impingement of the fluid onto the top of the windward wall is more pronounced; and the formation of the secondary vortex is seen.

Nazarian and Kleissl 2016 [42] analyzed the pressure distribution in the horizontal directions, and showed that the sign of Ri_h (i.e. the orientation of thermal forcing in accordance to wind direction) significantly modifies the pressure field, and consequently the flow. For instance, for the opposing condition (Ri_h >0), larger horizontal (streamwise) temperature gradient exists at the roof level, and the opposing

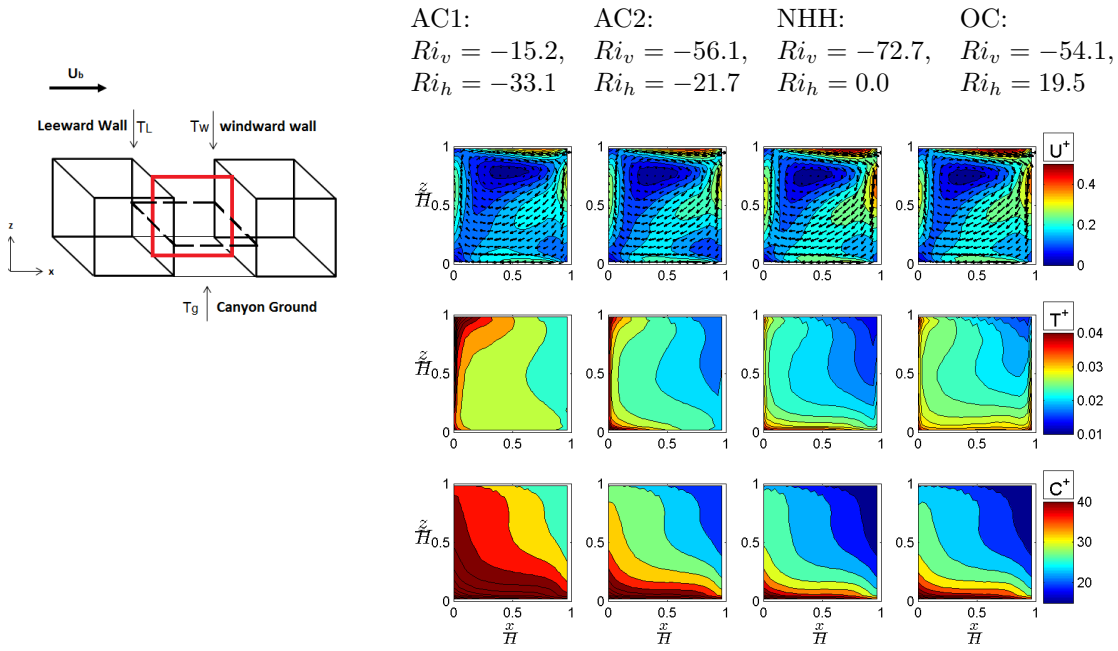

Figure 5.6: Same as Figure 5.5 for $U_b = 3\,\mathrm{m\,s^{-1}}$

windward heating results in higher resistance to the free-stream flow. Accordingly, a lower pressure gradient is observed inside the canyon compared to the assisting conditions ($Ri_h < 0$). The horizontal pressure gradient as well as the increased drag coefficient from the roughness then results in higher momentum entering the building roughness sublayer shown in Figure 5.5. However, while the intensity of the canyon vertex is seemingly larger and the center of the vortex is closer to the leeward wall, the opposing effect of buoyancy is apparent and the secondary vortex is pronounced in the windward corner of the building canyon for the highly unstable case of $U_b = 0.5\,\mathrm{m\,s^{-1}}$.

For the no horizontal heating condition (NHH, $Ri_h = 0$), the heat advected from the ground surface causes a larger temperature increase in the canyon than the convection from the roof, therefore increasing the strength of the vortex in the building canyon. It is worth mentioning that this behavior can be reversed when the more dominant roof heating decreases the vortex strength in the canyon [42].

Therefore the effect of roof heating should not be neglected and requires further investigation in the 3D street configuration. Comparing the flow field at cases AC2 and NHH with assisting condition 1 when strong horizontal heating is observed inside the canyon (AC1, $Ri_h = -33.1$ and $Ri_v = 15.2$), it can be concluded that the effect of vertical temperature gradient is more dominant than the horizontal thermal forcing in modifying the flow in the building canyon. The effect of horizontal heating becomes less significant when stability is increased.

The difference between assisting and opposing conditions (AC2 and OC) is more pronounced in the temperature distribution, when the thermal distribution is directly affected by the boundary conditions. At assisting conditions, the elevated temperatures are only concentrated near the heated leeward wall and the heat is primarily transported vertically along with wall, whereas in the opposing conditions, higher air temperature is observed within the canyon suggesting enhanced heat transfer and mixing inside the canyon (also shown in Nazarian and Kleissl [42]). Flow is conserved in the streamwise direction, and the resulting temperature gradient at roof level, in addition to the temperature/pressure gradient in span-wise direction is what contributes to increased momentum entering the building sublayer at opposing conditions.

Subsequently, the distribution of the pollutant concentration can be explained by the vortex formation in the building canyon. The primary vortex moves the ground-level emission and the maximum of the pollutant is always concentrated at the corner of the leeward wall and ground, while there exist a second point of maximum concentration at windward corner for $U_b = 0.5\,\mathrm{m\,s^{-1}}$ due to the formation of the secondary vortex. The minimum value is located at the top-east corner of the canyon.

When comparing the cases with the similar magnitude of Ri_v but opposing wall heating (OC and AC2), the concentration is larger at AC2 due to the lower intensity of the canyon vortex. However, compared to the temperature distribution, the concentration is only slightly different, suggesting that unlike the thermal field the distribution of concentration is less dependant on the horizontal temperature gradient, and is more affected by overall heating of surfaces (Ri_b), as also seen in AC1 case. Accordingly, the no-horizontal heating condition with the maximum value of vertical Richardson number has the lowest concentration due to the enhanced mixing in the absence of wall heating in the stream-wise canyon ($Ri_h = 0$). Normalized concentration increases with the decrease in vertical and horizontal Richardson numbers (increasing U_b) since the flow approaches the neutral stability conditions.

The effect of three-dimensional canyon configuration and realistic surface heating in the streamwise canyon can be better understood by investigating the flow properties in the spanwise direction (Figure 5.7). In the absence of surface heating, several factors distinguishes the roughness flow in 3D aligned arrays compared to 2-D street canyons: 1) In the building canyon (BC, $z < H$), formation of two symmetric counter-rotating vortices is seen in the z-y plane where the vortex size and its center varies with height. 2) The pair of counter-rotating vortices results is a hairpin-like structures within the BC that is demonstrated as "conditional eddies" by coceal et al. [40]. Accordingly, the center of the canyon vortex in the $x - z$ plane is moved upward as opposed to the center position in 2D canyons. 3) Due to the strong canopy-top shear layer, small eddies are shed off at the building edge into the streamwise canyon and above the building height. Above the buildings, the hairpin-shaped eddies with high frequency of ejections and sweeps, as well as low momentum regions are seen in

both configurations.

The presence of surface heating further modifies the flow structure. For brevity, only the opposing condition is analyzed here and vector field, normalized temperature and concentration are compared for different stability levels (Figure 5.7). The formation of counter-rotating vortices are modified by differential heating in a) building canyon (BC) and b) street canyon (SC). In the first category, formation of the secondary vortex in the x-y plane is apparent close to the windward wall, specifically for the at the highly unstable case ($U_b = 0.5\,ms^{-1}$ and max(Ri_v) = -72.7). Additionally, the two counter-rotating vortices in the $x - y$ are moved closer to the leeward wall. On the contrary, in the near neutral case of $U_b = 3\,\mathrm{m\,s^{-1}}$, the size of two vortices in the x-y plane are as large as canyon width, while they are modified by the ground heating in the y-z plane. In the second category, the temperature difference between north and south wall in the street canyon (SC) influences the symmetry of the vortices formed in the spanwise direction (x-y plane), as well as modifying the vortex shed off at building edges due to the strong shear layer (more pronounced for lower instability). Additionally, the ground heating at the street canyon (SC) forces more flow in the building canyon, and enhances downward velocity in the y-z plane for $U_b = 0.5\,\mathrm{m\,s^{-1}}$. Subsequently, the region of low momentum above the building height is more pronounced for this case.

The distribution of normalized temperature and concentration in the spanwise direction is illustrated in Figure 5.7. The range of contour colors are scaled with the velocity ratio in the two cases to aid comparison in this graph. The normalized temperature and concentration increases with inlet bulk velocity. Both temperature and concentration fields are modified by the flow structure in the building canyon and

more mixing is seen compared to street canyon. T^+ and C^+ are more concentrated close to the ground and the leeward wall for $U_b = 0.5\,\mathrm{m\,s^{-1}}$ and asymmetry due to differential heating in the street canyon is apparent in the x-y plane (south wall is predominantly warmer than the north wall).

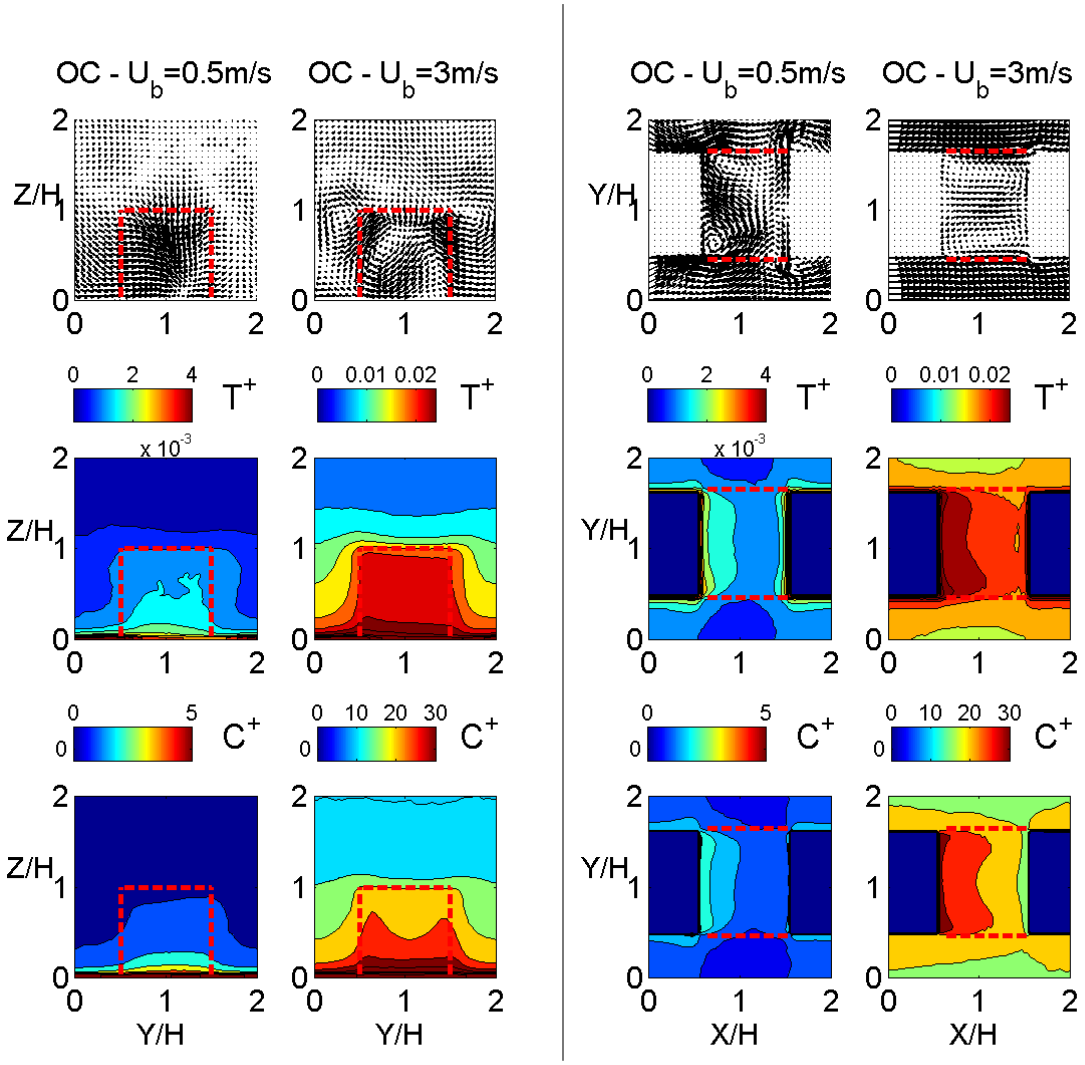

Figure 5.7: Contour plots of flow properties at the y-z (left) and x-y (right) planes in the center of the building canyon. Results are shown for the opposing condition (OC according to Table 5.2) for $U_b = 0.5, 3\,\mathrm{m\,s^{-1}}$. The contour color range is scaled with the velocity ratio in two cases for a better comparison.

Turbulent kinetic energy

Figure 5.8 depicts the contour plots of turbulent kinetic energy and the contribution of velocity variances in the Cartesian coordinates. The plots are outputted for different values of Ri_h and Ri_v at the center of building canyon ($x-z$ plane shown in Figures 5.5 and 5.6). Regardless of the heating orientation, TKE has the largest value at the windward corner, which is mostly generated by the shear from the primary canyon vortex. It is evident that the TKE is markedly enhanced with Ri_v due to the added effect of buoyancy (TKE is the largest for the NHH case and smallest at AC1). Additionally, the effect of horizontal heating orientation, Ri_h, is apparent when the opposing effect of momentum and buoyancy forcing at OC, results in significantly larger TKE than AC2.

The total TKE is dependent on both Ri_h and Ri_v, while the structure of turbulence remains unchanged with the heating intensity and orientation. The most pronounced sensitivity to the surface heating is seen for $w\prime w\prime$ at the leeward side, followed by $u\prime u\prime$ at the roof level. Unlike the 2D street canyon (Cheng and Liu [15]), the value of $\overline{v'v'}$ has the most contribution to the TKE production and cannot be neglected in the BC (Figure 5.8, note that the scales are different to show the variation with studied conditions). Another difference from the 2D canyon with uniform heating is seen when the largest contribution of $\overline{v'v'}$ to the TKE is at the corner of the windward wall. This is due to the modification of counter-rotating vortices by the surface heating in the streamwise canyon, as well as the ground heating in the BC.

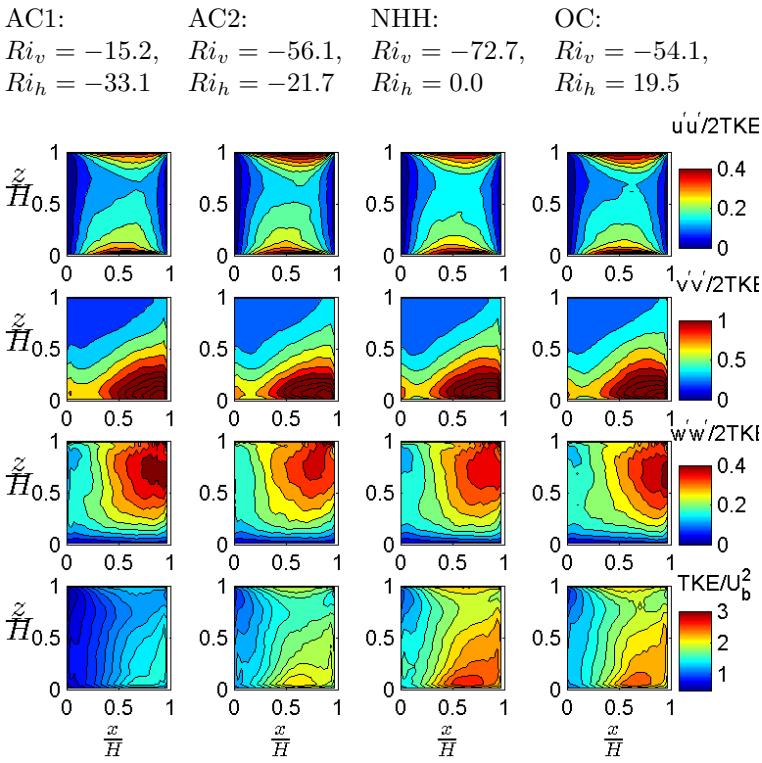

Figure 5.8: Contour plots of normalized turbulent kinetic energy (TKE/U_b) and velocity variances ($\overline{u_i'u_i'}/2TKE$) for $U_b = 0.5, 3\,\mathrm{m\,s^{-1}}$. The plane position and averaging is similar to Figure 5.5.

Turbulent transfer

Apart from the velocity standard deviations, the contours of turbulent fluxes of momentum ($\overline{u_i'u_j'}$), heat ($\overline{u_i'T'}$), and pollutant ($\overline{u_i'C'}$) are compared at different thermal forcing, where u_i indicates different components of velocity vector in a Cartesian system. Analysis are done for the convective case ($U_b = 0.5\,\mathrm{m\,s^{-1}}$).

Contour plots of Reynolds stresses at the $x-z$ cross section in the center of the building canyon are shown in Figure 5.9. It is evident that the turbulent momentum flux in a 3D canyon is dominated by the vertical transport of the horizontal momentum ($\overline{u'w'}$ and $\overline{w'v'}$), while the horizontal Reynolds stress, $\overline{u'v'}$, exhibits a random-like behavior with a relatively small magnitude. Unlike the 2D canyon, the magnitude

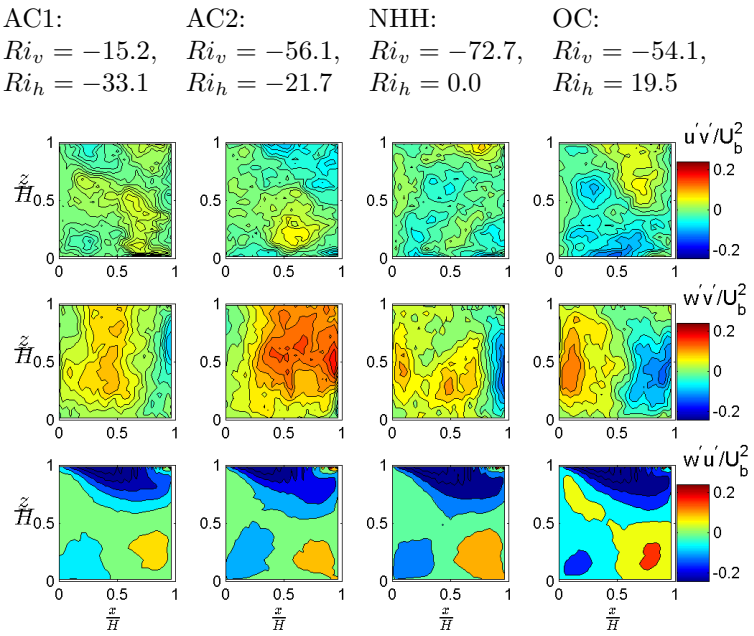

Figure 5.9: Similar to Figure 5.8 for Reynolds stresses normalized with inlet bulk velocity ($\overline{u_i' u_j'}/U_b^2$).

of $\overline{w'v'}$ is significant in the vertical momentum flux, and shows sensitivity to the orientation of the surface heating. For instance, at assisting conditions, roughly uniform and positive value of $\overline{w'v'}$ is seen inside the building canyon, whereas in the no-horizontal heating and opossing condition, a region of negative $\overline{w'v'}$ is also observed adjacent to the leeward wall. It should be noted that, although heat flux at south and north walls are varied, the temperature difference is the same for OC and AC2. Therefore, the difference in $\overline{w'v'}$ cannot be attributed to the surface heating in the street canyon (SC), and is directly affected by sign of Ri_h. At the roof level, large negative $\overline{u'w'}$ is seen for all heating conditions, that indicates substantial exchange of mass and momentum entrainment due to the strong shear layer. Besides, the roof-level vertical momentum flux is enhanced for the no-horizontal heating and opposing condition which is due to the increased intensity of the primary vortex. A second point of negative $\overline{u'w'}$ is seen at the leeward corner of the canyon, which was not previously

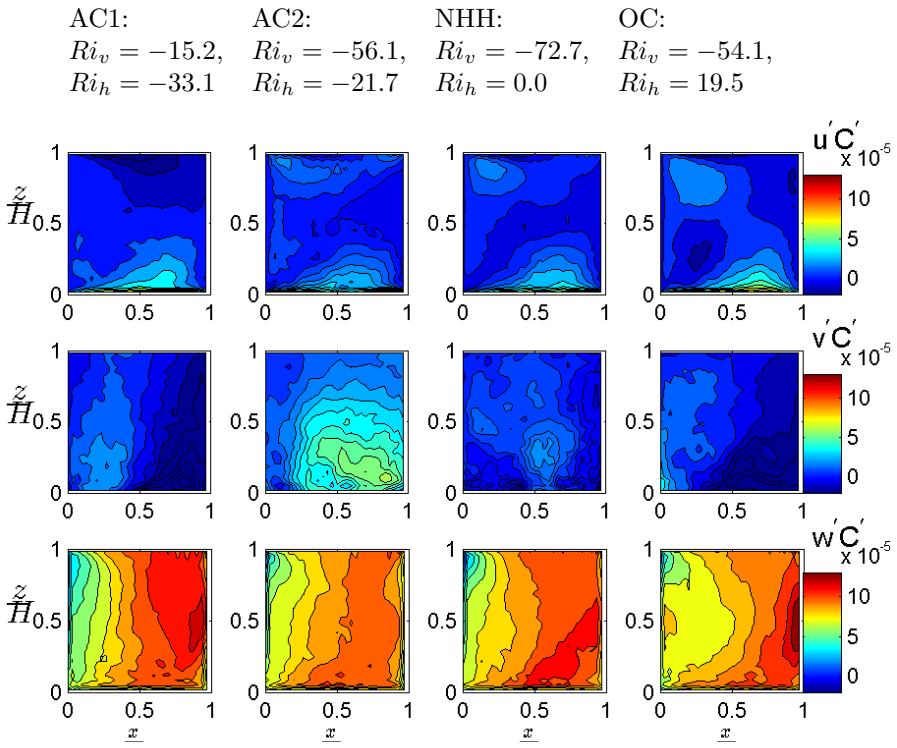

Figure 5.10: Similar to Figure 5.8 for time-averaged turbulent scalar flux ($\overline{u_i' C'}$).

observed in the 2D canyons with uniform heating ([15] and [25]). The negative vertical momentum flux can be attributed to the 3D effect of the building canyon, where the mass transfer occurs due to the counter-rotating vorticies formed in the $x - y$ plane.

In the windward corner of the building canyon, significant positive momentum flux $\overline{u'w'}$ is observed, which is generated and enhaned due to the buoyancy-driven flow in unstable conditions. In the windward heating case with the formation of the secondary vortex, the value of $\overline{u'w'}$ in this region is significantly increased due to the opposing buoyancy effect at this condition. Turbulent transfer of heat and pollutant are mostly governed by the fluctuation of vertical velocity, w'. Other components of momentum heat and scalar fluxes are negligible, except for the$\overline{w'T'}$ at the roof level particularly for the assisting conditions. Vertical heat transfer, $\overline{w'T'}$, is maximum at the windward heating due to the increased vortex intensity, and the opposing buoyancy

effect at OC, followed by the no-horizontal heating (NHH) condition. On a contrary, $w'C'$ shows little sensitivity to the heating orientation in the building canyon.

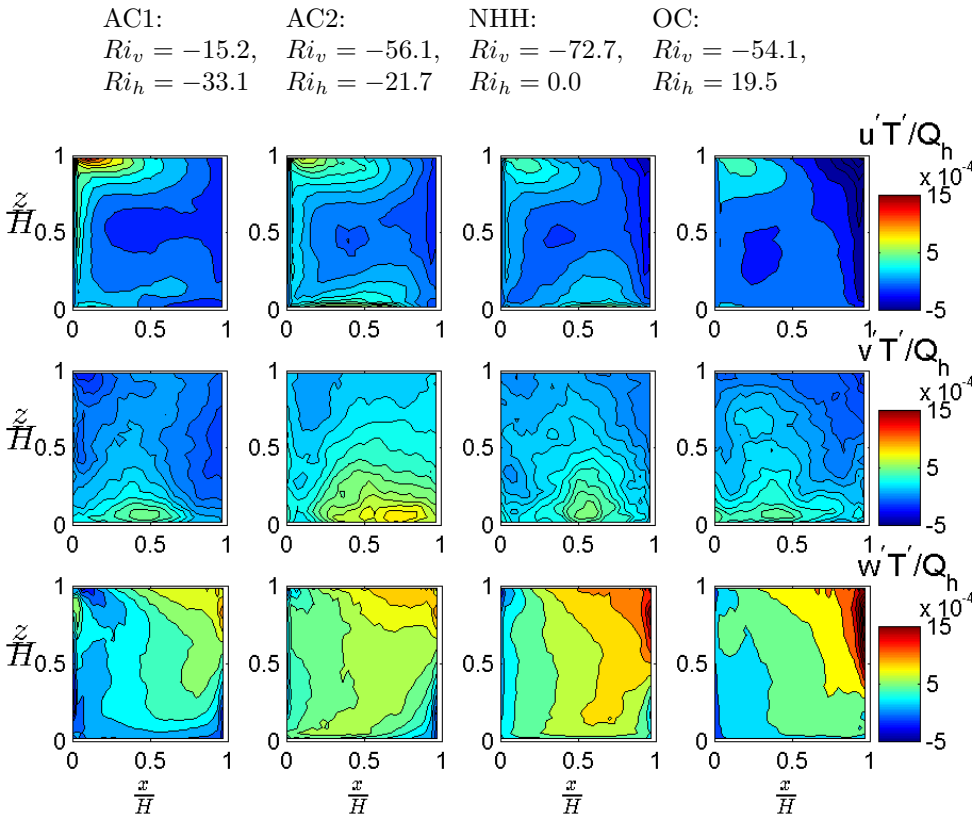

Figure 5.11: Similar to Figure 5.8 for time-averaged turbulent heat flux ($\overline{u_i' T'}$).

5.4.2 Coherent Structures in Unstable Urban Roughness

The mean flow properties discussed in Section 5.4.1 give insight on the turbulent flow field, but do not reveal the mechanisms involved in turbulent exchange. Thus, for a deeper understanding on the modifications of the turbulence structure by thermal forcing in the roughness sublayer, joint probability and quadrant measures of flux densities (turbulent momentum, heat and scalar flux) are analyzed in this section.

The quadrant analysis is a method of decomposing the turbulent fluxes, such

as Reynolds stress ($u'w'$), turbulent heat flux ($w'T'$), and turbulent scalar flux ($w'C'$), into 4 events based on the sign of the fluctuating components. For instance, when analyzing Reynolds stress, the events in quadrant 2 and 4 ($u'w' < 0$) are called ejections and sweeps, respectively, and indicate the coherent structures that contribute positively to the downward momentum flux. Additionally, events in quadrant 1 and 3 ($u'w' > 0$) are called outward and inward interaction, respectively, and represent the intermittency of turbulence. Figure 5.12 shows an example of the joint probability of $u'w'$ and the schematic of quadrant analysis, measured by Christen et al. [44] for an unstable condition at the roof level of a 2-D canyon.

The numbers mentioned in each box in Figure 5.12 represent the time fractions of event i, ϑ_i, which is the relative total duration of events in quadrant i. ϑ_i can be calculated for any two parameters a and b as

$$\vartheta_i = \int_{l_a}^{u_a} \int_{l_b}^{u_b} P(a,b) da db \,, \tag{5.4}$$

where $P(a,b)$ is the joint probability density function of a and b, and the lower and upper integration limits are defined based on the flux density. Table 5.3 summarizes the integral limits based on desired a and b. Typically, $u'w'$ is directed towards the surface while all other flux densities transport mass or energy away from the surface. Therefore, the numbering of quadrants are arranged so that the mean vertical wind gradient is opposite to the mean vertical temperature and concentration gradient [44]. Furthermore, the contribution of each event to the total flux density can be computed

Table 5.3: The lower and upper integration limits of the four quadrants according to the direction of the flux.

		Quadrant Number			
a = **u**	b = **w**	1	2	3	4
a = **T, C**	b = **w**	2	1	4	3
	l_a	0	$-\infty$	$-\infty$	0
	u_a	∞	0	0	∞
	l_b	0	0	$-\infty$	$-\infty$
	u_b	∞	∞	0	0

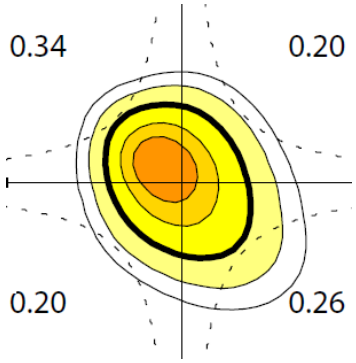

Figure 5.12: Normalized JPDFs of $u'w'$ at the roof level for an unstable condition measured by Christen et al. [44] and the schematic of quadrant analysis.

as the flux (or stress) fraction, S_i, introduced by Raupach [45]

$$S_i = \frac{1}{r_{ab}} \int_{l_a}^{u_a} \int_{l_b}^{u_b} abP(a,b)dadb\,. \tag{5.5}$$

The JPDF integral over the entire space is equal to one, therefore from 5.5, it is seen that

$$\Sigma_{i=1}^{4} S_i = 1\,. \tag{5.6}$$

From the stress fraction S_i, two measures of the relative importance of sweeps and ejections can be obtained: the difference between ejections (low momentum eddies

moving up) and sweeps (high momentum eddies moving down)

$$\Delta S_0 = S_4 - S_2 \,. \tag{5.7}$$

and their ratio

$$\gamma = S_2/S4 \,. \tag{5.8}$$

Additionally, Shaw et al. (1983) introduced Exuberance, Exu, as the the ratio of unorganized to coherent events,

$$Exu = \frac{S_1 + S_3}{S_2 + S_4} \,, \tag{5.9}$$

where the contribution of (unorganized) counter fluxes are compared to the (organized) contributions in the direction of the average flux. Accordingly, Exuberance is regarded as the measure of efficiency for the turbulent exchange.

In the following section, simulations of unstable urban environments are used to analyze the modifications of a) joint probabilities and frequency of events, b) coherent structures (ejections and sweeps), and c) efficiency of the turbulent transfer, due to the realistic surface heating. The analysis are done for the 4 studied conditions described in Section 5.3, and JPDs of vertical fluxes (combinations of u, C and T with w) are calculated. Six different height are chosen at urban roughness sublayer up to $6H$, where H is the building height, and 5 positions along the roof level are analyzed. Ensemble averaging approach described in section 5.2.4 is not a suitable method when analyzing the turbulent structures through time series of flow properties.

Thus, for calculating the quadrant measures, instead of using the diurnal simulation of flow, each studied conditions are run with corresponding surface boundary conditions constant with time, and flow properties are sampled every 3 seconds for an extended period of 8 hrs. The JPDFs are calculated with 26×26 bins for $\hat{u_i}$, $\hat{C}$, and $\hat{T}$, where $\hat{a}$ represents the fluctuation parameter a', normalized with variances of a, σ_a, so that $\hat{a} = a'/\sigma_a$. $\hat{u_i}$, $\hat{C}$, and $\hat{T}$ range from -4 to 4.

A) Quadrant analysis in neutral condition

The Direct Numerical Simulation (DNS) of aligned arrays of cubes is performed by Branford et al. [46] for a neutral condition, and is used to evaluate the results obtained by the Large Eddy Simulation (LES) model. The DNS output are gathered every 0.005s at heights $0.5H$ and $1.5H$ for 150 seconds. LES results are outputted at various locations every 3s for a period of 8 hours, therefore the number of data points are similar for the comparison. Grid resolution are similar with 32 and 30 grids per H for DNS and LES models, respectively.

Joint probability density functions and time fractions – The shape of the quadrants, and the frequency of events are in close agreement for both LES and DNS runs (Fig. 5.13). In the street canyon, the correlation between u and w is small and the JPDF has a roughly symmetric shape, with a slight dominance of intermittent over coherent events. Above the roof level at $z/H = 1.5$, however, a distinct quadrant shape is observed with higher frequency of organized events. In the neutral LES run, the quadrant shape is seen up to height of 3H, and the frequency of organized events can be as high as 65%. Along the roof level, JPDFs are highly dependent on their positions with regards to the leeward and windward walls. Close to the leeward wall,

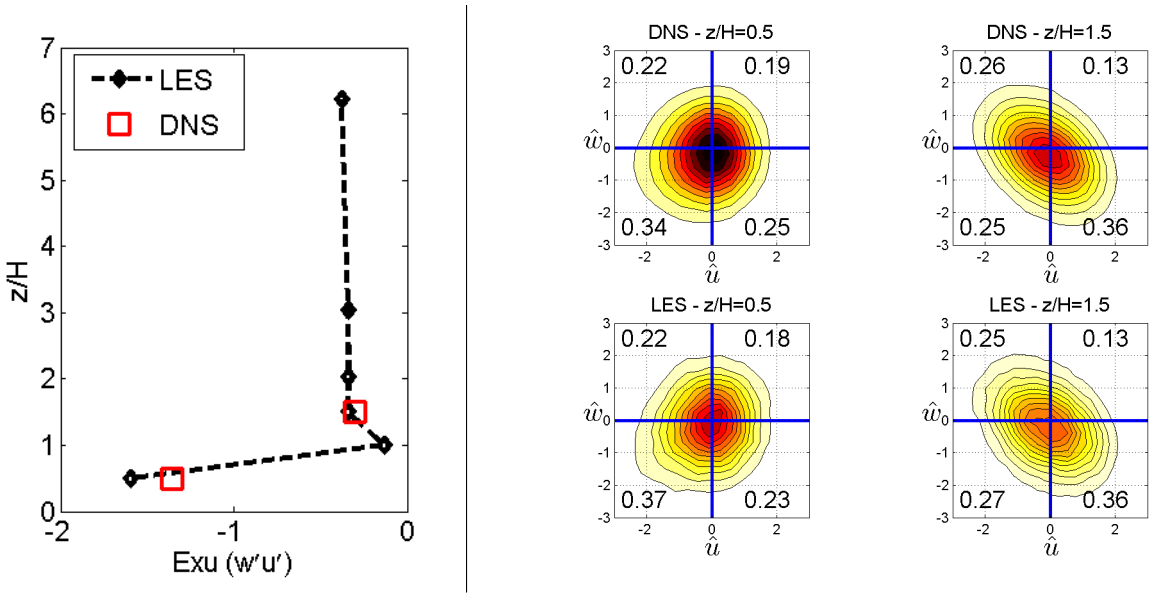

Figure 5.13: Left: Vertical profile of Exuberance (Exu) with height, and right: joint probability density functions for LES and DNS results of a neutral condition.

r_{uw} is very small ($u'w' \approx 0$) and the quadrant has a symmetric shape. In the center of roof level, the quadrant shape is seen and the frequency of organized events are more than 70% at $x/H = 0.75$. However, the quadrant shape is reversed and extended towards $E1$ and $E3$ adjacent to the windward wall.

Efficiency of turbulent transfer – Close agreement is seen in the value of exuberance at $0.5H$ and $1.5H$ for both LES and DNS runs (5.13). In the neutral LES runs, the highest efficiency of turbulent momentum transfer is at the center of roof level, and the lowest efficiency is inside the building canyon where the intermittent events are dominant. Additionally, exuberance is highly varied along the roof level in x-direction (5.16). Adjacent to the leeward and windward walls, intermittent events become more significant and the turbulent efficiency is low. In particular, adjacent to the windward wall, the value of $E \approx -2$ is seen, indicating twice intermittent events as organized structures. This can be attributed to the point of flow separation and impingement at the edge of the windward wall. Above the building height, exuberance

converges to approximately -0.3 at around 2 times the building height.

Coherent Structures – $u'w'$ is towards the surface (negative) except inside the canyon. Sweep events has large contribution to the total turbulent momentum transfer in the building canyon, while the flow transitions to ejection-dominated flow above the roof level height. In the x direction, adjacent to the leeward and windward walls, ejections are dominant, while in the center part of the canyon, the contribution of ejection and sweeps are similar (seen also in the DNS results) and the flow is only slightly sweep dominated. $u'w'$ is also mostly negative along the roof level, except adjacent to the windward wall.

B) Quadrant analysis in unstable condition

In this section, the structures that contribute to turbulent transfer are analyzed as modified by thermal forcing inside the canyon. Figures 5.14 - 5.22 show the JPDFs of Reynolds stress ($u'w'$), turbulent heat flux ($w'T'$), and turbulent scalar flux ($w'C'$) at different heights, and along the roof level in the building canyon. Additionally, the profiles of quadrant measures with z and x are demonstrated for different opposing-, assisting-, and no-horizontal heating conditions described in Section 5.3.

1) *Turbulent momentum transfer*

The value of Reynolds stress $u'w'$ is significantly enhanced due to the buoyancy effect induced by the surface heating (Fig. 5.16). $u'w'$ has small upward (positive) value at the street level, followed by the maximum downward momentum flux at the roof level. $u'w'$ then decreases with z and reaches zero at 6 times the building height (the height of the computational domain is 7.5H).

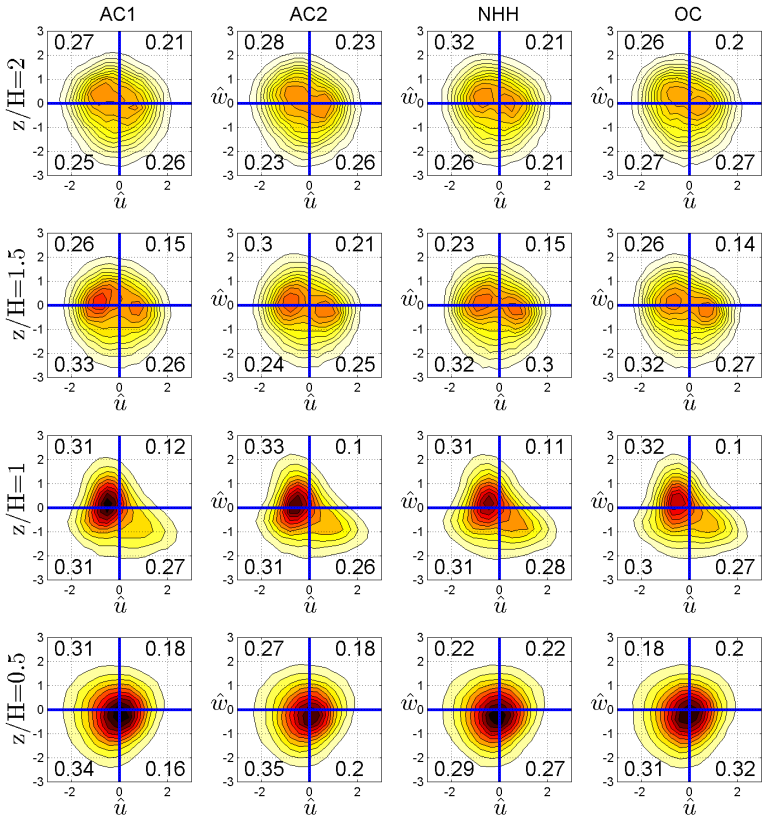

Figure 5.14: Normalized JPDFs of $\overline{u'w'}$ at different heights and stability conditions for $U_b = 0.5\mathrm{m\,s^{-1}}$. The numbers labelling the individual quadrants denotes the time fraction of each events.

Joint probability density functions and time fractions – At the *street level*, small correlation is seen between u' and w', and the JPDFs are characterized by a nearly rotational symmetric shape that is similar to the neutral condition. Regardless of the heating distribution, the time fraction of quadrants show slight dominance of intermittent events, where inward interactions are significantly more frequent. However, the frequency of organized events are dependent on the heating orientation, where windward heating case (OC) induces higher frequency of sweeps as opposed to the leeward heating case with symmetric heating distribution (AC2).

At the *roof level* in the building canyon, r_{uw} significantly increases at the center, and a quadratic shape is observed with strong dominance of organized events (up to 60%). Time fraction of ejections is larger than sweeps for all studied conditions, but the ratio between E2 and E4 varies with the heating orientation, where ejections are more dominant at assisting heating conditions. Similar to the neutral case, high variability of JPDFs is seen along the roof level for all heating conditions. However, as opposed to the neutral condition significant correlation is seen between u and w adjacent to the leeward wall where the quadrant shape is extended into the second and fourth quadrants and organized structures are more frequent (up to 63%). The r_{uw} is also larger adjacent to the windward wall with high frequency of intermittent events for all heating conditions.

As moving *above the building* height, the frequency of organized events becomes smaller, and the correlation between u and w decreases. At $z = 2H$, the frequency of all quadrants are similar, expect for the no horizontal heating condition that shows higher frequency of ejection. This behavior is different from the neutral condition, where the quadrant shape is still seen and organized event are predominantly frequent at this height.

Efficiency of turbulent transfer – Compared to the neutral case, the efficiency of the turbulent momentum transfer is larger at the street level, and smaller at and above the building height. In another word, surface heating increases the contribution of organized structures inside the canyon, while adding more intermittency to the flow above the building height. For the studied heating conditions, exuberance is not significantly sensitive to the heating orientation and the most effective turbulent momentum transfer is yet seen at center of the roof level. Adjacent to the windward

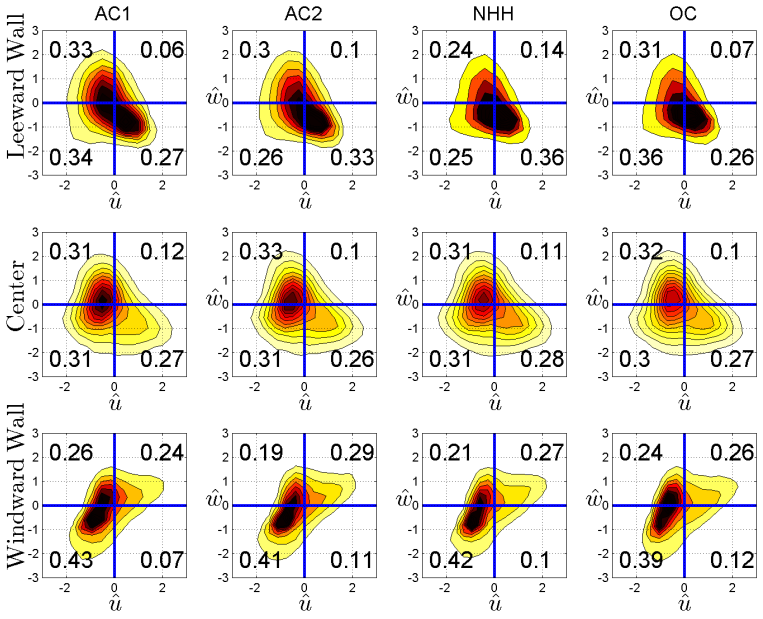

Figure 5.15: Normalized JPDFs of $\overline{u'w'}$ at different points along the roof level ($z/H = 1$), and different stability conditions for $U_b = 0.5\mathrm{m\,s^{-1}}$. The numbers labelling the individual quadrants denotes the time fraction of each events.

wall at the roof level where the point of flow impingement occurs, the intermittency is also significantly increased due to the surface heating, with the lowest efficiency (Exu) happening for the assisting conditions. Previously it was mentioned that lower momentum enters the canyon in assisting conditions and the vortex intensity is smaller, that can further explain the observation here for lower efficiency of turbulent transfer.

Coherent Structures – Surface heating inside the canyon induces sweeps with large contribution to the momentum flux density. Accordingly, as opposed to the neutral condition, the contribution of sweep events is larger to the turbulent momentum transfer at the street level in all heating orientations. At the roof level, sweep is once again dominant at the center for all cases, while ejections become more significant adjacent to the windward wall. Adjacent to the leeward wall, however, sweeps are more significant when heating is introduced. Heating orientation modifies the contribution

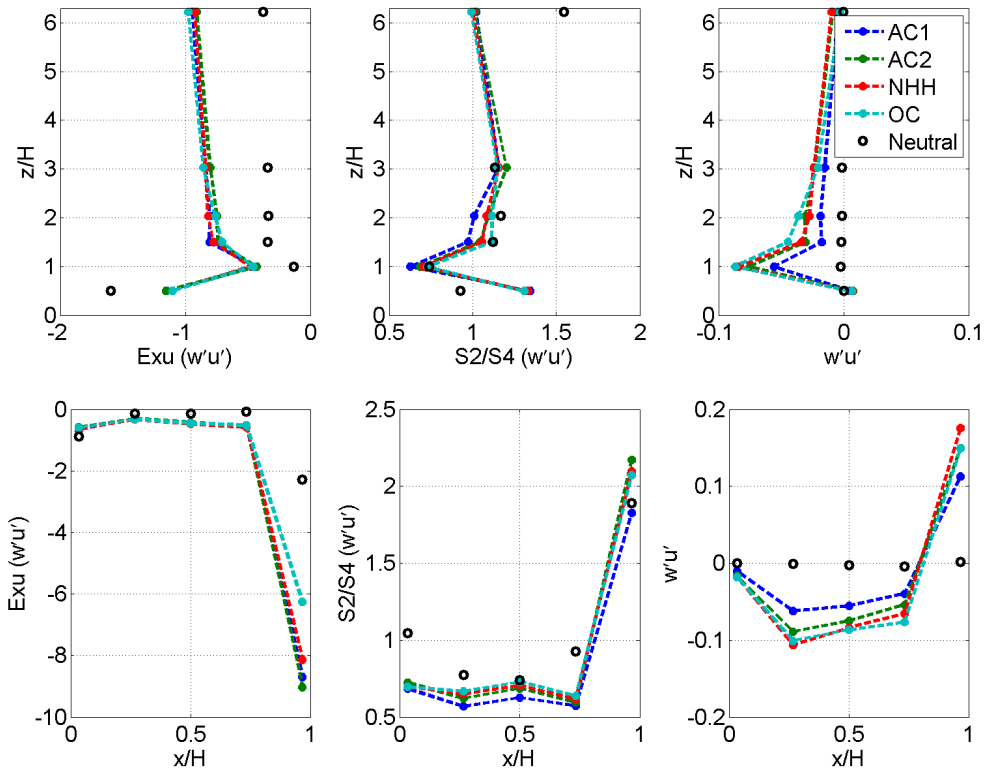

Figure 5.16: Profiles of quadrant measures for $\overline{u'w'}$ with height, z, and x along the roof level for $U_b = 0.5\mathrm{m\,s^{-1}}$.

of coherent structures further above the street canyon. At the assisting condition 1, ejections have the largest contribution to the turbulent momentum transfer from $z = H$ to $2H$, whereas sweeps are more dominant for the opposing condition at this height. This cab be further explained with the increased momentum entering the building canyon for opposing condition, where more high-momentum flow is transferred downward, thus more sweeps is observed.

2) *Turbulent heat transfer*

Joint probability density functions and time fractions – As apposed to the turbulent heat flux ($u'w'$) that is usually directed towards the surface in the building roughness sublayer, the direction of turbulent heat and pollutant flux is

generally upward, such that turbulence moves heat and concentration away from the surface. This behavior is also demonstrated by the positive value of $w'T'$ and $w'C'$ in Figures 5.19 and 5.22. Therefore, to keep the same physical meaning assigned to the quadrant analysis terminology, position of organized and unorganized quadrants are modified according to Table 5.3.

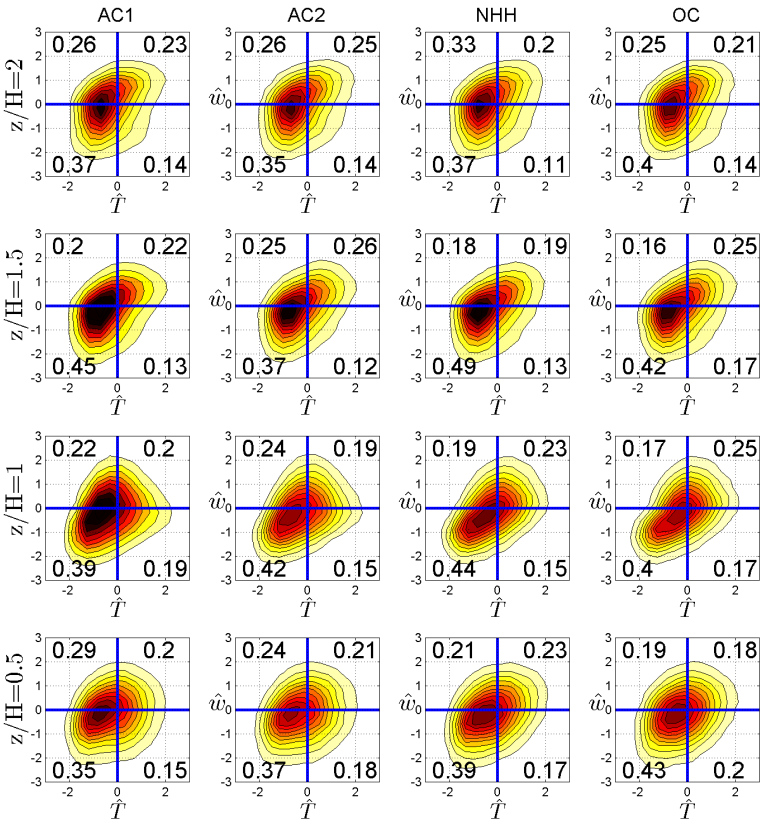

Figure 5.17: Normalized JPDFs of $\overline{w'T'}$ at different heights and stability conditions for $U_b = 0.5\mathrm{m\,s^{-1}}$.

Figure 5.17 shows the JPDFs of $\hat{w}$ and $\hat{T}$ at different heights and heating conditions. It is interesting to note that the correlation between w and T, r_{wT}, is significantly large even at the street level (as apposed to $u'w'$) and the JPDFs are extended to the $E2$ and $E4$ events at all heights up to $2H$. Additionally, the frequency of inward interactions is the lowest among all quadrants, while sweeps are the most

frequent events regardless of the heating orientation and height. Heating orientation, however, modifies the $E2/E4$ ratio. For instance, the opposing condition 1 (AC1) has higher frequency of sweeps compared to the opposing condition (OC), except at the roof level. Additionally, the frequency of intermittent events are lower at NHH condition.

The variability of JPDFs with heating orientation is more apparent along the roof level. Close to the leeward wall, the frequency of intermittent events, specifically inward interaction, is larger compared to the center, while ejections become less frequent. Adjacent to the windward wall, however, frequency of outward interaction is increased while sweeps are less frequent.

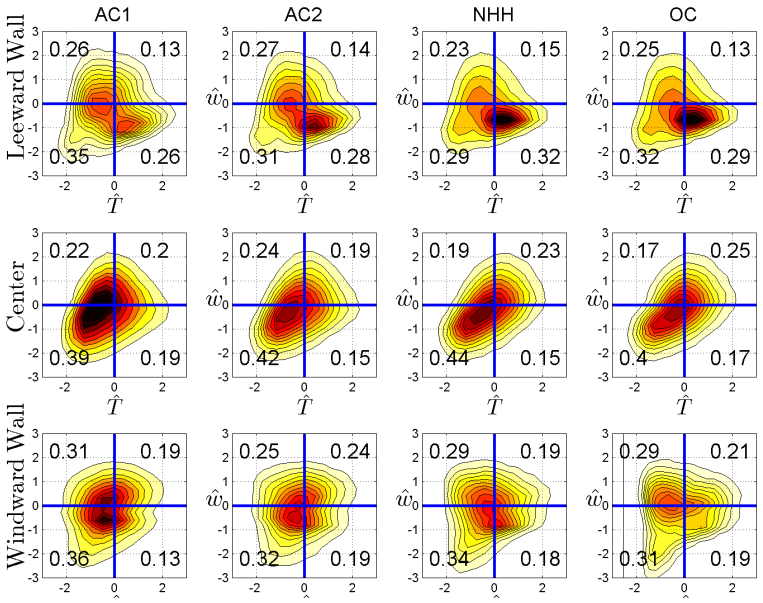

Figure 5.18: Normalized JPDFs of $\overline{w'T'}$ at different points along the roof level ($z/H = 1$), and different stability conditions for $U_b = 0.5\mathrm{m\,s^{-1}}$.

Efficiency of turbulent transfer – Efficiency of turbulent heat transfer is significantly higher than momentum transfer, as shown by the value of Exu. The highest efficiency of $w'T'$ transfer is seen at center of the roof level, and for no-horizontal heating conditions and opposing conditions. Assisting condition 1, with

large horizontal temperature difference on the other hand, exhibits the lowest efficiency of turbulent heat transfer, especially at the street level. Adjacent to the windward and leeward walls, Exu decreases significantly, while organized events still have the highest contribution to the total $w'T'$.

Coherent structures – Significance of ejections and sweeps to the total transfer of $w'T'$ varies with height and the heating orientation. For instance, at the street level, sweeps dominate the turbulent heat transfer, except for the no-horizontal heating condition where the flow is ejection-dominated. At the roof level, all locations show strong contribution of sweeps, while $S2/S4$ is significantly affected by the heating orientation. For instance, adjacent to the windward wall, assisting conditions exhibit same contribution of sweeps and ejections.

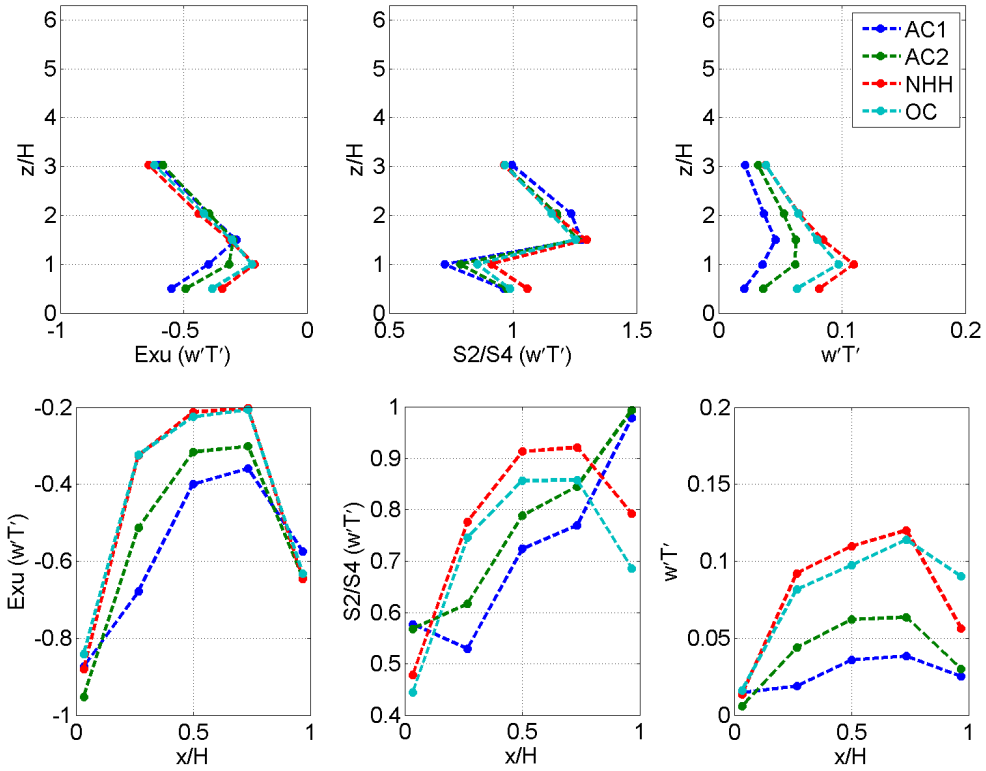

Figure 5.19: Profiles of quadrant measures of turbulent heat flux $\overline{w'T'}$ with height, z, and x along the roof level for $U_b = 0.5\mathrm{m\,s^{-1}}$.

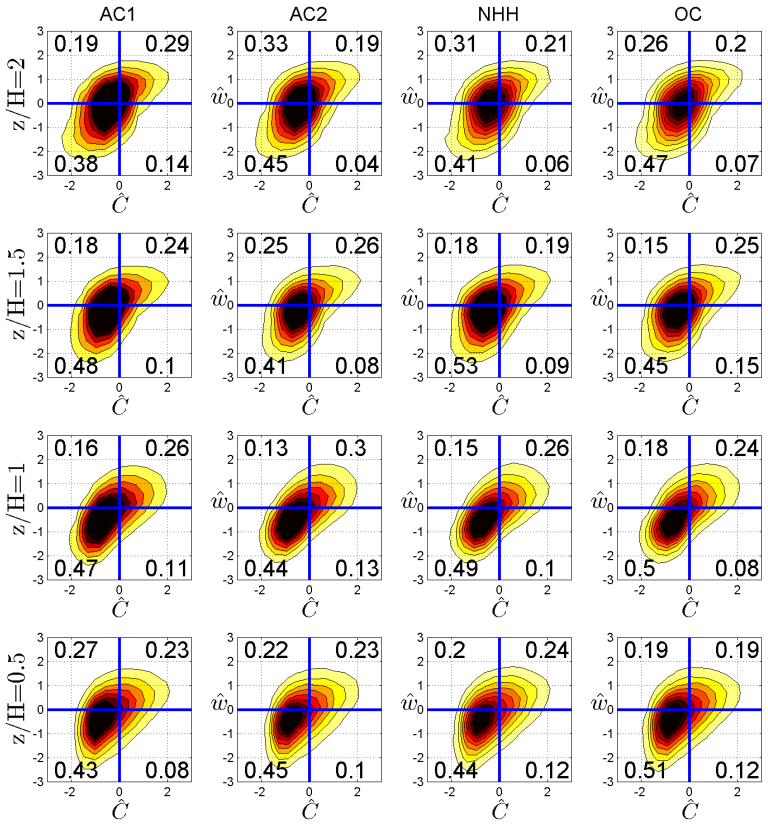

Figure 5.20: Normalized JPDFs of $\overline{w'C'}$ at different heights and stability conditions for $U_b = 0.5\mathrm{m\,s^{-1}}$.

2) *Turbulent pollutant transfer*

Joint probability density functions and time fractions – Similar to the JPDFs of turbulent heat flux, strong correlation is seen between w and C in and above the street canyon, and the frequency of organized events are significantly higher (up to 75%) for all heating conditions. On the other hand, inward interaction exhibits the lowest frequency while ejections are the most frequent events. The windward heating increases the frequency of organized events. At all heights, $E2 + E4$ is larger than $E1 + E3$ for opposing condition (OC) than assisting condition 2 (AC2).

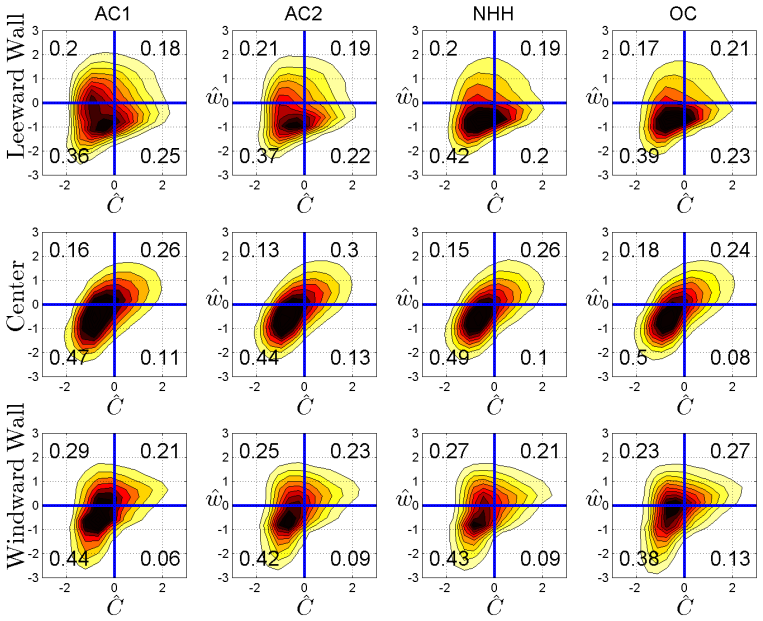

Figure 5.21: Normalized JPDFs of $\overline{w'C'}$ at different points along the roof level ($z/H = 1$), and different stability conditions for $U_b = 0.5\mathrm{m\,s^{-1}}$.

Efficiency of turbulent transfer – Efficiency of the turbulent pollutant exchange is significantly higher than heat and momentum transfer. The magnitude of counterfluxes (unorganized events) are 20% of the organized events inside the canyon (Exuberance shown in Figure 5.22). Exuberance reaches the minimum of -0.5 at the leeward edge of the roof level for the case of maximum assisting horizontal heating (AC1). It it noteworthy that minimum efficiency of the turbulent heat and pollutant transfer occurs at the leeward corner of the roof level, while Exu for $w'u'$ is minimum at the leeward corner.

Coherent structures – Pollutant transfer is ejection dominated up to $2H$ and transitions to sweeps after $3H$. At the roof level, however, sweeps are important adjacent to the windward and leeward walls.

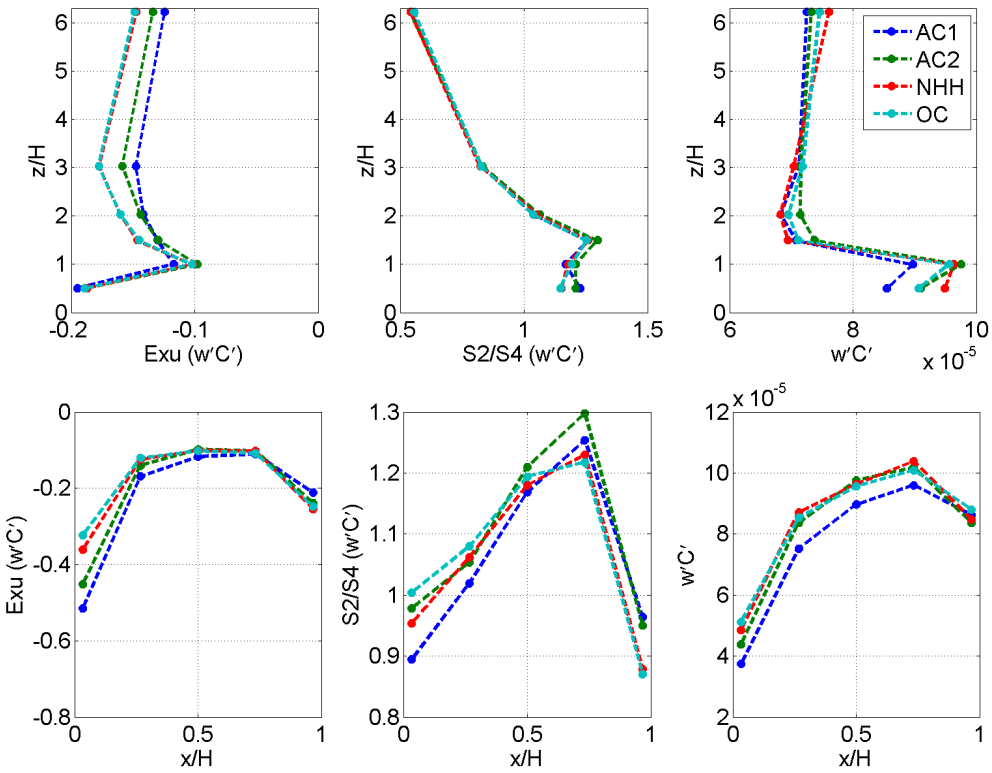

Figure 5.22: Profiles of quadrant measures of turbulent scalar flux $\overline{w'C'}$ with height, z, and x along the roof level for $U_b = 0.5\mathrm{m\,s^{-1}}$.

5.4.3 Breathability in Street Canyon

Breathability in the streat canyon is analyzed by comparing the daily variation of concentration, as well as exchange rate from ventilating faces. Figure 5.23 shows the concentration varying with Time of Day (ToD) and averaged in the canyon volume, as well as the horizontal plane at which the pedestrian breath in (z 1.8m). The parabolic shape of this figure represent the variation of Ri_v, while the average concentration is slightly higher when Ri_h is positive (opposing conditions) due to the increased momentum entering the canyon.

Figure 5.24 - 5.27 shows the variation of concentration at spanwise and streamwise canyons with vertical and horizontal Richardson number. There is a notable

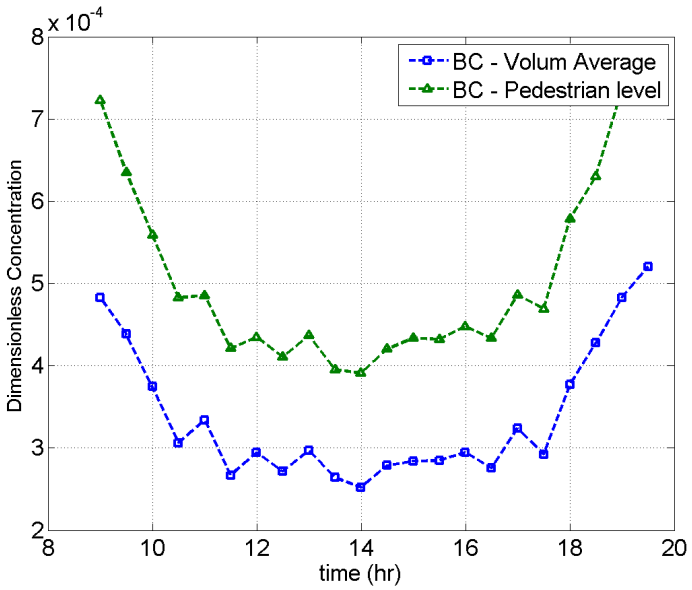

Figure 5.23: variation of dimensionless concentration with Time of Day (ToD), in the volume between the buildings in the spanwise canyon (BC).

correlation between the concentration in the building canyon and the vertical Richardson number Ri_v regardless of the wind speed (Fig. 5.24),while the concentration in the streamwise canyon seems to be more affected by the horizontal Richardson number. Additionally, figure 5.29 also demonstrated that when the value of vertical Richardson number is low, the horizontal temperature gradient (and the sign of Ri_h) then determines in the concentration in the spanwise canyon.

The concept of Air Exchange Rate in street canyon represents the volumetric air exchange (removal or entry) per unit time integrated over the ventilating faces of street canyons. Applying kinetic (mass) balance in the 3D street canyon, 3D-ACH is defined by sum of air exchange rates along the top and sides of the canyon as

$$<\mathrm{ACH_{top}}> = \frac{\int\int w_{+}\mathrm{d}x\mathrm{d}y}{A_{top}} \ , <\mathrm{ACH_{side\pm}}> = \frac{\int\int v_{\pm}\mathrm{d}x\mathrm{d}z}{A_{side}} \ . \tag{5.10}$$

Here only velocities exiting the canyon are considered, i.e. w_{+} are positive vertical

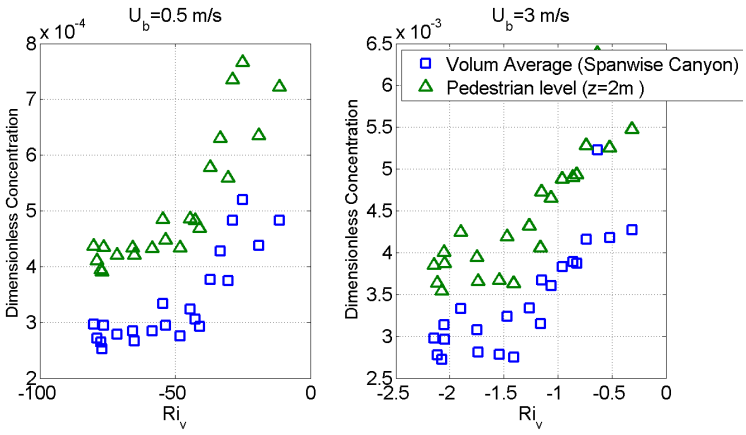

Figure 5.24: variation of dimensionless concentration with vertical Richardson number, in the volume between the buildings in the spanwise canyon (BC).

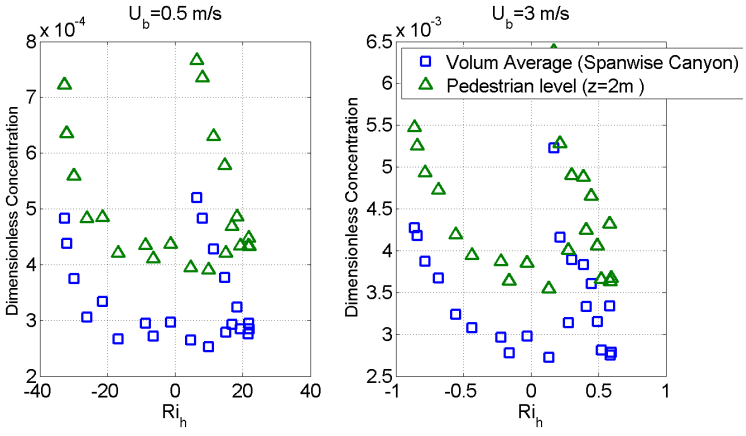

Figure 5.25: variation of dimensionless concentration with horizontal Richardson number, in the volume between the buildings in the spanwise canyon (BC).

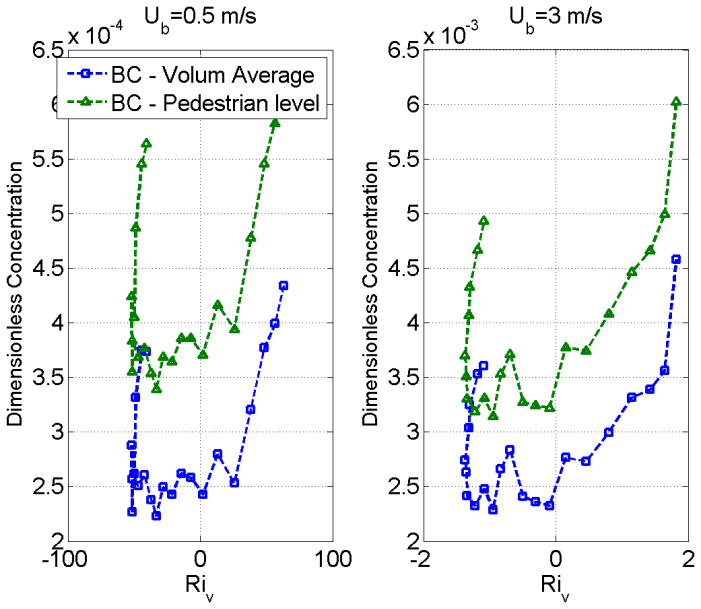

Figure 5.26: variation of dimensionless concentration with vertical Richardson number, in the streamwise canyon (SC).

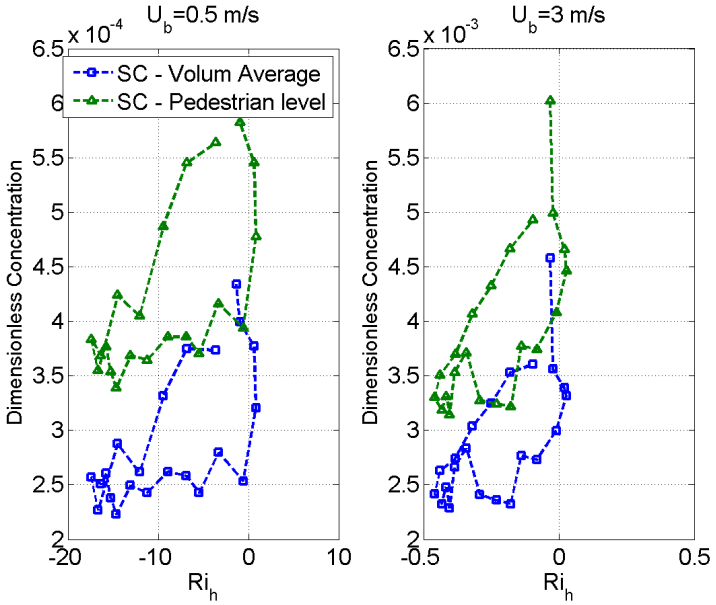

Figure 5.27: variation of dimensionless concentration with horizontal Richardson number, in the volume between the buildings in the streamwise canyon (SC).

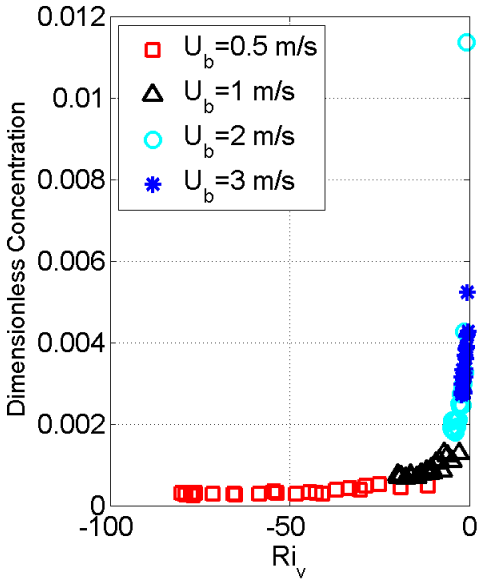

Figure 5.28: variation of dimensionless concentration with vertical Richardson number, in the volume between the buildings in the spanwise canyon (BC).

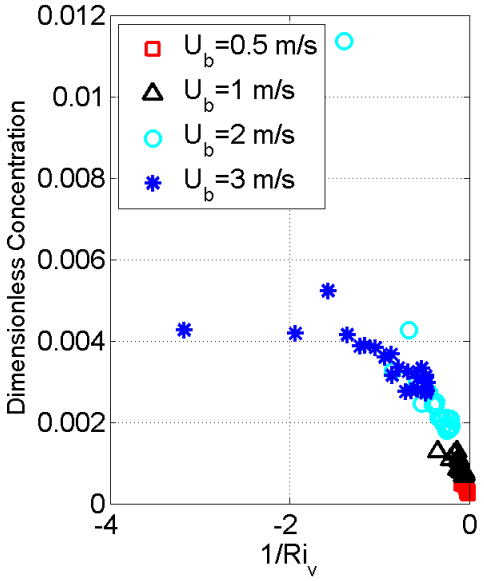

Figure 5.29: variation of dimensionless concentration with reciprocal of vertical Richardson number, in the volume between the buildings in the spanwise canyon (BC).

velocities along the top plane and according to the orientation of the side plane, the sign of spanwise velocity (v) differs to represent air removal. A_{top} and A_{side} are the areas of top and side of the urban canyon. To analyze the relative effects of mean flow and fluctuations on air removal from the building canyon, ACH is calculated both using the velocity and local velocity fluctuations (e.g. $v' = v - \overline{v}$) and referred to as ACH_{w} and $\text{ACH}_{\text{w}'}$, respectively.

Figure 5.30 shows the time series of ACH_{w} and $\text{ACH}_{\text{w}'}$ calculated for the simulation case with inlet bulk velocity of 3 $m\,s^{-1}$. The ventilating faces are identified as follows. In the span-wise building canyon, the vertical planes that bound the volume between the buildings are defined by their coordinate in span-wise (y) direction, where side +y and side -y are aligned with the north and south walls of the building, respectively. The horizontal surface at roof level in the span-wise and street-wise canyons are identified as building canyon and street canyon, "BC" and "SC", respectively.

The ACH do not have a symmetrical behavior around solar noon throughout a day and are influenced by the sign of Ri_h. In the assisting conditions when Ri_h is negative and the Ri_v is also large, the ACH does not increase, presumably due to the effect of warm air advected in the canyon from the heated roof. The air exchanged from the horizontal surface at top of the building canyon (BC, spanwise canyon) is the largest followed by south vertical ventilating face (side -y) and then north of the building canyon, with the horizontal surface at top of the street canyon (SC, streamwise canyon) having the smallest value of ACH (Fig. 5.30). The difference between ACH_w and ACH'_w is significant at the top BC face and the south ventilating face (side -y), while at SC and north horizontal face (side +y) the velocity fluctuation has

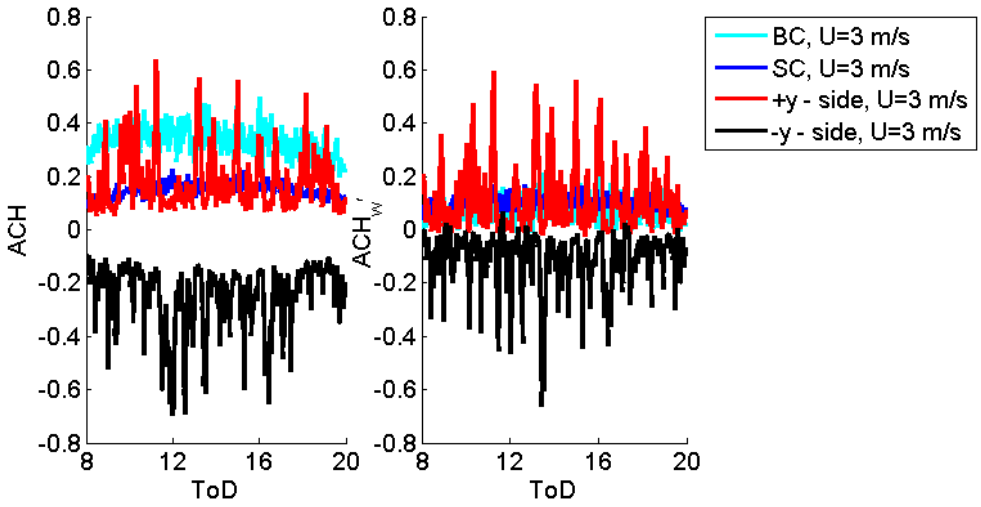

Figure 5.30: Comparison of instantaneous ACH calculated over all ventilating faces for U=3m/s.

the main contribution to ACH. Pollutant Exchange Rate has a very similar patterns tp ACH (not shown) which demonstrates that the correlation between concentration and velocity does not change during the day. Therefore only by analyzing the flow field we can have an accurate calculation of pollutant exchange from the canyon level.

5.5 Conclusions

In order to mitigate the concerns regarding the climate in urban environment, various methods are currently used as to reduce the pollutant emission. In parallel, there needs to be more analysis on the effect of design on adapting to the current reduced level of emission in the urban environment. This understanding can further inform urban designers on the impact of their design on air quality, human health and comfort. Additionally, in the case of poisionous release in a populated urban area, the informed estimates of the affected area and the rate at which the particles are

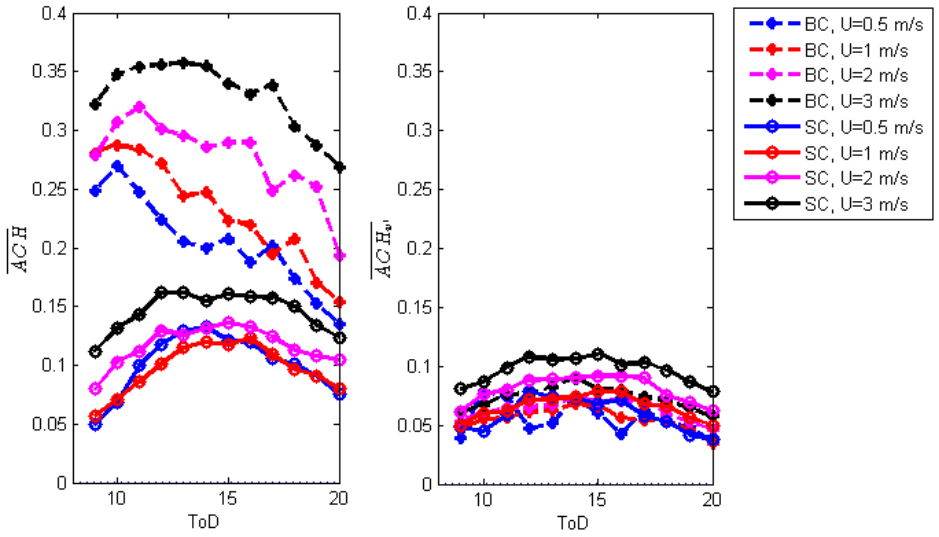

Figure 5.31: Time-average ACH over 60 mins interval calculated over the horizontal ventilating faces.

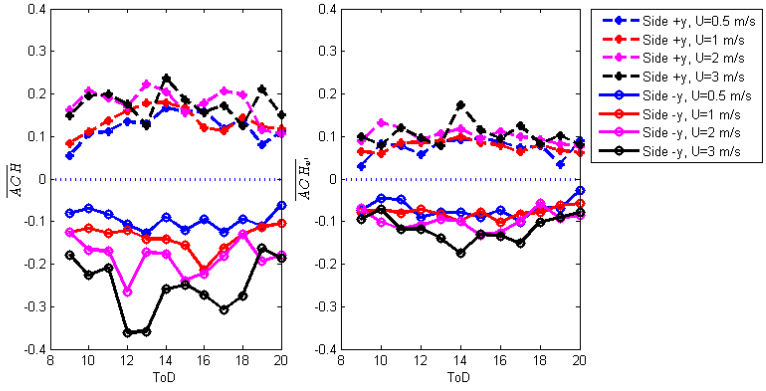

Figure 5.32: Time-average ACH over 60 mins interval calculated over the vertical ventilating faces.

removed vertically is crucial.

A three dimensional configuration of a compact urban environment is simulated with realistic surface heating and ground-level pollutant emission. The significance of considering realistic surface heating on the accurate analysis of pollutant dispersion is emphasized. Concentration distribution is shown to be correlated with horizontal and vertical Richardson numbers. Air Exchange Rate at street ventilating faces are analyzed and shown to have distinct characteristic according to the orientation and strength of the heated walls. Following this methodology, the study aims to further investigate the air quality and breathability in urban canopy.

Acknowledgements

Chapter 5, in part is currently being prepared for submission for publication of the material. Nazarian, Negin; Martilli, Alberto; Kleissl, Jan. The dissertation author was the primary investigator and author of this material.

Bibliography

[1] Timothy R Oke. *Boundary layer climates*. Routledge, 2002.

[2] FT DePaul and CM Sheih. Measurements of wind velocities in a street canyon. *Atmospheric Environment (1967)*, 20(3):455–459, 1986.

[3] Y Nakamura and TR Oke. Wind, temperature and stability conditions in an east-west oriented urban canyon. *Atmospheric Environment (1967)*, 22(12):2691–2700, 1988.

[4] Y Qin and SC Kot. Dispersion of vehicular emission in street canyons, guangzhou city, south china (prc). *Atmospheric Environment. Part B. Urban Atmosphere*, 27(3):283–291, 1993.

[5] Ruwim Berkowicz, Finn Palmgren, Ole Hertel, and Elisabetta Vignati. Using measurements of air pollution in streets for evaluation of urban air qualitymeterological analysis and model calculations. *Science of the total environment*, 189:259–265, 1996.

[6] Shaodong Xie, Yuanhang Zhang, Li Qi, and Xiaoyan Tang. Spatial distribution of traffic-related pollutant concentrations in street canyons. *Atmospheric Environment*, 37(23):3213–3224, 2003.

[7] K Jerry Allwine, MJ Leach, LW Stockham, JS Shinn, RP Hosker, JF Bowers, and JC Pace. Overview of joint urban 2003an atmospheric dispersion study in oklahoma city. In *Preprints, Symp. on Planning, Nowcasting and Forecasting in the Urban Zone, Seattle, WA, Amer. Meteor. Soc., CD-ROM J*, volume 7, 2004.

[8] SJ Arnold, H ApSimon, J Barlow, S Belcher, M Bell, JW Boddy, R Britter, H Cheng, R Clark, RN Colvile, et al. Introduction to the dapple air pollution project. *Science of the Total Environment*, 332(1):139–153, 2004.

[9] Robert N Meroney, Michel Pavageau, Stilianos Rafailidis, and Michael Schatzmann. Study of line source characteristics for 2-d physical modelling of pollutant dispersion in street canyons. *Journal of Wind Engineering and Industrial Aerodynamics*, 62(1):37–56, 1996.

[10] P Kastner-Klein and EJ Plate. Wind-tunnel study of concentration fields in street canyons. *Atmospheric Environment*, 33(24):3973–3979, 1999.

[11] CJ Baker and DM Hargreaves. Wind tunnel evaluation of a vehicle pollution dispersion model. *Journal of Wind Engineering and Industrial Aerodynamics*, 89(2):187–200, 2001.

[12] P Kastner-Klein, E Fedorovich, and MW Rotach. A wind tunnel study of organised and turbulent air motions in urban street canyons. *Journal of Wind Engineering and Industrial Aerodynamics*, 89(9):849–861, 2001.

[13] Petra Kastner-Klein and Mathias W Rotach. Mean flow and turbulence characteristics in an urban roughness sublayer. *Boundary-Layer Meteorology*, 111(1):55–84, 2004.

[14] Xian-Xiang Li, Rex E Britter, Tieh Yong Koh, Leslie K Norford, Chun-Ho Liu, Dara Entekhabi, and Dennis YC Leung. Large-eddy simulation of flow and pollutant transport in urban street canyons with ground heating. *Boundary-layer meteorology*, 137(2):187–204, 2010.

[15] WC Cheng and Chun-Ho Liu. Large-eddy simulation of turbulent transports in urban street canyons in different thermal stabilities. *Journal of Wind Engineering and Industrial Aerodynamics*, 99(4):434–442, 2011.

[16] Seung-Bu Park, Jong-Jin Baik, Siegfried Raasch, and Marcus Oliver Letzel. A large-eddy simulation study of thermal effects on turbulent flow and dispersion in and above a street canyon. *Journal of Applied Meteorology and Climatology*, 51(5):829–841, 2012.

[17] Zijing Tan, Jingliang Dong, Yimin Xiao, and Jiyuan Tu. A numerical study of diurnally varying surface temperature on flow patterns and pollutant dispersion in street canyons. *Atmospheric Environment*, 104:217–227, 2015.

[18] Alberto Martilli. On the derivation of input parameters for urban canopy models from urban morphological datasets. *Boundary-layer meteorology*, 130(2):301–306, 2009.

[19] N Nazarian and J Kleissl. Realistic solar heating in urban areas: Air exchange and street-canyon ventilation. *Building and Environment*, 2015.

[20] Jean-François Sini, Sandrine Anquetin, and Patrice G Mestayer. Pollutant dispersion and thermal effects in urban street canyons. *Atmospheric Environment*, 30(15):2659–2677, 1996.

[21] Seung-Bu Park, Jong-Jin Baik, and Young-Hee Ryu. A large-eddy simulation

study of bottom-heating effects on scalar dispersion in and above a cubical building array. *Journal of Applied Meteorology and Climatology*, 52(8):1738–1752, 2013.

[22] Jae-Jin Kim and Jong-Jin Baik. A numerical study of thermal effects on flow and pollutant dispersion in urban street canyons. *Journal of applied meteorology*, 38(9):1249–1261, 1999.

[23] Jae-Jin Kim and Jong-Jin Baik. Urban street-canyon flows with bottom heating. *Atmospheric Environment*, 35(20):3395–3404, 2001.

[24] Xiaomin Xie, Chun-Ho Liu, Dennis YC Leung, and Michael KH Leung. Characteristics of air exchange in a street canyon with ground heating. *Atmospheric Environment*, 40(33):6396–6409, 2006.

[25] Xian-Xiang Li, Rex E Britter, Leslie K Norford, Tieh-Yong Koh, and Dara Entekhabi. Flow and pollutant transport in urban street canyons of different aspect ratios with ground heating: large-eddy simulation. *Boundary-layer meteorology*, 142(2):289–304, 2012.

[26] Negin Nazarian and Jan Kleissl. Cfd simulation of an idealized urban environment: Thermal effects of geometrical characteristics and surface materials. *Urban Climate*, 12:141–159, 2015.

[27] Neda Yaghoobian and Jan Kleissl. An improved three-dimensional simulation of the diurnally varying street-canyon flow. *Boundary-Layer Meteorology*, 153(2):251–276, 2014.

[28] JL Santiago, ES Krayenhoff, and A Martilli. Flow simulations for simplified urban configurations with microscale distributions of surface thermal forcing. *Urban Climate*, 9:115–133, 2014.

[29] Siegfried Raasch and Michael Schröter. Palm–a large-eddy simulation model performing on massively parallel computers. *Meteorologische Zeitschrift*, 10(5):363–372, 2001.

[30] Marcus Oliver Letzel, Martina Krane, and Siegfried Raasch. High resolution urban large-eddy simulation studies from street canyon to neighbourhood scale. *Atmospheric Environment*, 42(38):8770–8784, 2008.

[31] Neda Yaghoobian and Jan Kleissl. Effect of reflective pavements on building energy use. *Urban Climate*, 2:25–42, 2012.

[32] A Kovar-Panskus, L Moulinneuf, E Savory, A Abdelqari, J-F Sini, J-M Rosant, A Robins, and N Toy. A wind tunnel investigation of the influence of solar-induced

wall-heating on the flow regime within a simulated urban street canyon. *Water, Air and Soil Pollution: Focus*, 2(5-6):555–571, 2002.

[33] E Scott Krayenhoff and James A Voogt. A microscale three-dimensional urban energy balance model for studying surface temperatures. *Boundary-Layer Meteorology*, 123(3):433–461, 2007.

[34] David Fleming Brown. An improved methodology for characterizing atmospheric boundary layer turbulence and dispersion. 1997.

[35] CO Pedersen, RJ Liesen, RK Strand, DE Fisher, L Dong, and PG Ellis. A toolkit for building load calculations; exterior heat balance. *American Society of Heating, Refrigerating and Air Conditioning Engineers (ASHRAE), Building Systems Laboratory*, 2001.

[36] Daniel Hillel. *Introduction to soil physics*, volume 364. Academic press New York, 1982.

[37] Steve A Piacsek and Gareth P Williams. Conservation properties of convection difference schemes. *Journal of Computational Physics*, 6(3):392–405, 1970.

[38] James W Deardorff. Stratocumulus-capped mixed layers derived from a three-dimensional model. *Boundary-Layer Meteorology*, 18(4):495–527, 1980.

[39] Neda Yaghoobian, Jan Kleissl, and E. Scott Krayenhoff. An improved three-dimensional simulation of the diurnally varying street-canyon flow. *Boundary-Layer Meteorology*, 153(2):251–276, 2014.

[40] Omduth Coceal, Adrian Dobre, and T Glyn Thomas. Unsteady dynamics and organized structures from dns over an idealized building canopy. *International Journal of Climatology*, 27(14):1943–1953, 2007.

[41] MR Raupach and RH Shaw. Averaging procedures for flow within vegetation canopies. *Boundary-Layer Meteorology*, 22(1):79–90, 1982.

[42] Negin Nazarian and Jan Kleissl. Realistic surface heating in urban areas: Air exchange and street-canyon ventilation. *Building and Environment*, 2015.

[43] Xiaoming Cai. Effects of differential wall heating in street canyons on dispersion and ventilation characteristics of a passive scalar. *Atmospheric Environment*, 51:268–277, 2012.

[44] Andreas Christen, Eva van Gorsel, and Roland Vogt. Coherent structures in urban roughness sublayer turbulence. *International journal of Climatology*, 27(14):1955–1968, 2007.

[45] MR Raupach and A St Thom. Turbulence in and above plant canopies. *Annual Review of Fluid Mechanics*, 13(1):97–129, 1981.

[46] Jean Claus, Omduth Coceal, T Glyn Thomas, S Branford, Stephen E Belcher, and Ian P Castro. Wind-direction effects on urban-type flows. *Boundary-layer meteorology*, 142(2):265–287, 2012.

Chapter 6

Concluding Remarks

In order to mitigate the concerns regarding the climate in urban environment, various methods are currently used as to reduce the pollutant emission, thermal stresses, and energy consumption. In parallel, there needs to be more analysis that deepen our understanding on urban microclimate, as well as informing us on the effect of design on adapting to the climate. Accordingly, the presented study constitutes an example of comprehensive methodology that considers the impact of surface heating on pedestrian wind flow, thermal environment, air quality, and building energy consumption in urban environments.

First, the importance of considering complex realistic conditions on 3-dimensional thermal and momentum fields is demonstrated through numerical modeling of urban environments. Additionally, a potentially universal characterization method is introduced for the realistic heating distribution that breaks down the total thermal forcing in urban environment into directional forcing in horizontal and vertical directions. Lastly, validity of this parametrization is confirmed by a similarity analysis, and the correlation of wind flow, thermal field, and pollutant concentration with this

characterization method is evaluated.

This understanding can further inform urban designers on the impact of their design on air quality, human health and comfort. For instance, the characterization method introduced in this work is modified by surface material and radiative properties, as well as wind speed and direction. Therefore, using this method, it would be possible to make reliable prediction of air quality and thermal comfort without explicitly resolving the flow around buildings.

Followings are some suggestions as extensions of this research to provide additional insight into the physics and effects of urban microclimate:

- Creating guideline maps that qualitatively evaluate the impact of building and street surface materials, radiative properties, and weather conditions on thermal comfort and air quality.

- Evaluate the complexity of turbulence, or of the urban geometry, that needs to be included in numerical analysis, depending on the parameter and scale of interest.

Appendices

APPENDIX A - Turbulence Modeling: Large Eddy Simulation

In LES the larger three dimensional unsteady turbulent motions are directly represented, whereas the effect of small scales of motion is modeled [1]. By applying a filtering operation, velocity is decomposed into the sum of a resolved (filtered) and a residual components i.e, $u = \hat{u} + u'$ where $\hat{()}$ is a filtered quantity. The nonlinear term $\widehat{u_i u_j}$ appears in the non-dimensional incompressible form of Navier-Stokes equations and needs to be modeled. It is common to rewrite this term with the subgrid-scale stress (τ_{ij}) and split the additional stresses into an anisotropic part and add the isotropic part to the pressure. The resulting LES equations are

$$\frac{\partial \hat{u}_i}{\partial x_i} = 0 \ , \tag{.1}$$

$$\frac{\partial}{\partial t}(\hat{u}_i) + \frac{\partial}{\partial x_i}(\hat{u}_i \hat{u}_j) = -\frac{1}{\rho}\frac{\partial P^*}{\partial x_i} - \frac{\partial \tau_{ij}}{\partial x_j} + \frac{\partial}{\partial x_j}[\nu(\frac{\partial \hat{u}_i}{\partial x_j} + \frac{\partial \hat{u}_j}{\partial x_i})] \ . \tag{.2}$$

Filtering the energy equation, one obtains

$$\frac{\partial \rho \hat{h_s}}{\partial t} + \frac{\partial \rho \hat{u_i} \hat{h_s}}{\partial x_i} - \frac{\partial \hat{p}}{\partial t} - \hat{u_j}\frac{\partial \hat{p}}{\partial x_i} - \frac{\partial}{\partial x_i}(\lambda \frac{\partial \hat{T}}{\partial x_i}) = -\frac{\partial}{\partial x_j}\left[\underbrace{\rho\left(\widehat{u_i h_s} - \hat{u_i}\hat{h_s}\right)}_{\text{subgrid enthalpy flux}}\right], \tag{.3}$$

where h_s and λ are the sensible enthalpy and thermal conductivity, respectively. The subgrid enthalpy flux term in the equation above is approximated using the gradient hypothesis:

$$\rho\left(\widehat{u_i h_s} - \hat{u_i}\hat{h_s}\right) = -\frac{\mu_{\text{SGS}} C_p}{\text{Pr}_{\text{SGS}}}\frac{\partial \hat{T}}{\partial \hat{x_j}}\,, \tag{.4}$$

where μ_{SGS} is a subgrid scale viscosity, and Pr_{SGS} is the subgrid scale Prandtl number equal to 0.85. More details of the Subgrid Scale models implementation in ANSYS FLUENT and their validations can be found in [2].

Algebraic Wall-Modeled LES Model (WMLES)

The energy containing scales in the turbulent spectrum are small near the wall and require an excessively high resolution and a small time step for wall-resolving LES models. The Reynolds number scaling limitations of LES can be overcome using the Algebraic Wall-Modeled LES (WMLES) approach [3]. In WMLES, RANS is applied for wall-distances $0 < d_w < 0.5h_{\max}$, where d_w is the distance to the wall and $h_{\max}$ is the maximum local grid spacing. With the increase in wall distance an empirical blending function provides rapid switching of the model from RANS to LES for $0.5h_{\max} < d_w < h_{\max}$.

The Algebraic WMLES formulation proposed by Shur et.al. [3] combines a mixing

length model with a modified Smagorinsky model [4] and with the wall damping function of [5]. The eddy viscosity is calculated with the use of a hybrid length scale:

$$v_t = \min\left[(kd_w)^2, (C_s\Delta)^2\right] |\hat{S}| \left[1 - exp\left[-\left(\frac{y^+}{25}\right)^3\right]\right] \tag{.5}$$

where $|\hat{S}|$ is the magnitude of the strain rate tensor, $k = 0.41$ is the van Karman constant, $C_s = 0.2$ is the Smagorinsky constant, and y^+ is the normal to the wall inner scaling. The WMLES model is based on a modified grid scale to account for the grid anisotropies in wall-modeled flows:

$$\Delta = \min(\max(C_w d_w; C_w h_{\max}; h_{wn}), h_{\max}) \ . \tag{.6}$$

Here $h_{\max}$ is the maximum edge length of the cell, h_{wn} is the wall-normal grid spacing, and $C_w = 0.15$ is a constant.

APPENDIX B - Turbulence Modeling: Detached Eddy Simulation

This section describes the two Delayed Detached Eddy Simulation (DDES) models that are compared with experimental results and LES model in section 4.3. DES was originally proposed by Spalart et al. [6] to address high Reynolds number flows over complex wall-bounded configurations using affordable computational resources. In the DES approach, the unsteady RANS models are employed in the boundary layer, while the subgrid scale formulation of LES is applied in the regions where the resolution is fine enough for LES. The LES region covers the turbulent region where large unsteady eddies play a dominant role. In the near-wall region, the

respective RANS models are recovered.

Spalart-Allmaras based DDES model

The standard Spalart-Allmaras model uses the distance to the closest wall as the definition for the length scale d, which plays a major role in determining the level of turbulent production or destruction [7]. The DES model, as proposed by Shur et al. [8] replaces d everywhere with a new length scale $\tilde{d}$, defined as

$$\tilde{d} = \min(d, C_{DES}\Delta_{\max}) \ , \tag{.7}$$

where the grid spacing $\Delta_{\max}$ is the largest grid spacing in the x, y, or z directions. The empirical constant C_{des} has a value of 0.65. Accordingly, where the grid is not fine enough to sustain resolved turbulence, the LES mode is activated inside the boundary layer. Delayed detached-eddy simulation (DDES) by Spalart et al [9] is further introduced to preserve the RANS mode throughout the boundary layer and $\tilde{d}$ is re-defined according to:

$$\tilde{d} = d - f_d \mathrm{min}(0, \mathrm{d} - \mathrm{C_{des}}\Delta_{\max}) \ ,$$

where f_d is given by:

$$f_d = 1 - tanh((8r_d)^3)$$

and

$$r_d = \frac{\nu_t + \nu}{\sqrt{U_{i,j}U_{i,j}}k^2 d}; \;\; k = 0.41.$$

Realizable $k-\epsilon$ based DDES model

The Realizable $k-\epsilon$ based DES model is similar to Realizable $k-\epsilon$ RANS model by Shih et al [10] with the exception of the dissipation term in the k equation. In the DES model, the realizable $k-\epsilon$ RANS dissipation term is modified such that

$$Y_k = \frac{\rho k^{\frac{3}{2}}}{l_{des}} \ ,$$

where

$$l_{des} = \min(l_{rke}, l_{les})$$
$$l_{rke} = \frac{k^{\frac{3}{2}}}{\epsilon}$$
$$l_{les} = C_{des}\Delta_{\max} \ ,$$

where C_{des} is a calibration constant used in the DES model and has a value of 0.61. Similarly to the Spalart-Allmaras model, the delayed concept can be applied as well to the Realizable DES model to preserve the RANS mode throughout the boundary layer. The DES length l_{des} is redefined such that

$$l_{des} = l_{rke} - f_d \max(0, l_{rke} - C_{des}\Delta_{\max}) \ .$$

APPENDIX C - Standard Wall Function

The standard wall functions provided in ANSYS FLUENT [11] are based on the work of Launder and Spaldin [12]. The law-of-the-wall for mean velocity modified for roughness has the form

$$U^* = \frac{1}{k} ln(Ey^*) - \Delta B,$$

where

$$U^* = \frac{U_P C_\mu^{1/4} k_P^{1/2}}{\tau_w/\rho}$$

is the dimensionless velocity,

$$y^* = \frac{\rho C_\mu^{1/4} k_P^{1/2} y_P}{\mu}$$

is dimensionless distance from the wall,

$$\Delta B = \frac{1}{k} ln f_r$$

and k is the Von Karman constant (0.4187), E is an empirical constant (9.793), U_P is the mean velocity of the fluid at the near-wall node P, k_P is the turbulence kinetic energy at the near-wall node P, y_P is the distance from point P to the wall, μ is the dynamic viscosity of the fluid and, f_r is the roughness function.

The roughness function quantifies the shift of the intercept due to roughness effects and depends on the type and size of the roughness. In ANSYS FLUENT, the roughness is classified into the three regimes, and the formulas proposed by [13] based on Nikuradse's data are adopted to compute ΔB for each regime. For a sand-grain roughness and similar types of uniform roughness elements, however, ΔB has been

found to be well-correlated with the nondimensional roughness height, $K_s^+ = \rho K_s u^*/\mu$, where K_s is the physical roughness height and $u^* = C_\mu^{1/4} k_P^{1/2}$.

The Reynolds analogy between momentum and energy transport gives a similar logarithmic law for mean temperature

$$T^* \equiv \frac{(T_w - T_P)\rho c_p C_\mu^{1/4} k_P^{1/2}}{\dot{q}} = \begin{cases} \mathrm{Pr} y^* + \frac{1}{2}\rho \mathrm{Pr} \frac{C_\mu^{1/4} k_P^{1/2}}{\dot{q}} U_P^2 & (y^* < y_T^*) \\ \mathrm{Pr}_t \left[\frac{1}{\kappa} \ln(E y^*) + P \right] + & \\ \frac{1}{2}\rho \frac{C_\mu^{1/4} k_P^{1/2}}{\dot{q}} \left\{ \mathrm{Pr}_t U_P^2 + (\mathrm{Pr} - \mathrm{Pr}_t) U_c^2 \right\} & (y^* > y_T^*) \end{cases},$$

where P is computed as [14]

$$P = 9.24 \left[(\frac{Pr}{Pr_t})^{3/4} - 1 \right] [1 + 0.28 e^{-0.007 Pr/Pr_t}]$$

and $\dot{q}$ is wall heat flux, T_P is the temperature at the first near-wall node P, T_w is the temperature at the wall, Pr is the molecular Prandtl number ($\mu c_p/k_f$), Pr_t is the turbulent Prandtl number at the wall (=0.85), A is the Van Driest constant (= 26) and, U_c is the mean velocity magnitude at $y^* = y_T^*$. The non-dimensional thermal sublayer thickness, y_T^*, is the wall distance where the linear law and the logarithmic law intersect, given the molecular Prandtl number of the fluid.

The function for P for rough walls is modified as follows:

$$P_{rough} = 3.15 Pr^{0.695} (\frac{1}{E'} - \frac{1}{E})^{0.359} + (\frac{E'}{E})^{0.6} P$$

where E' is the wall function constant modified for the rough walls, defined by $E' = E/f_r$.

The procedure of applying the law-of-the-wall for temperature is as follows. Once the physical properties of the fluid being modeled are specified, its molecular Prandtl number is computed. Then, given the molecular Prandtl number, the thermal sublayer thickness, y_T^*, is computed from the intersection of the linear and logarithmic profiles, and stored. During the iteration, depending on the y^* value at the near-wall cell, either the linear or the logarithmic profile is applied to compute the wall temperature T_w or heat flux $\dot{q}$ (depending on the type of the thermal boundary conditions).

During the iteration, depending on the y^* value at the near-wall cell, either the linear or the logarithmic profile is applied to compute the wall temperature T_w or heat flux $\dot{q}$ (depending on the type of the thermal boundary conditions).

APPENDIX D - Solar Load Model

ANSYS FLUENT calculates direct normal irradiation based on the approach presented in the 2001 ASHRAE Handbook [15]

$$E_{dn} = \frac{A}{e^{\frac{B}{sin(\beta)}}},$$

where A is apparent solar irradiation at air mass m=0 and B is the atmospheric extinction coefficient, and β is the solar altitude. Diffuse solar irradiation on a surface is expressed as:

$$E_d = CE_{dn}\frac{(1 + cos\epsilon)}{2},$$

where C is a constant whose values are given in Table 7 from Chapter 30 of the 2001 ASHRAE Handbook of Fundamentals [15] as a function of aerosol optical depth and precipitable water in each month (0.134 for the month of June). Y is the ratio of sky diffuse radiation on a vertical surface to that on a horizontal surface (calculated as a function of incident angle) and, ϵ is the tilt angle of the surface (in degrees) from the horizontal plane. The equation for ground reflected solar irradiation on a surface is

$$E_r = E_{dn}(C + sin(\beta)\rho_g \frac{(1 - cos\epsilon)}{2}),$$

where ρ_g is the ground albedo (0.18 for asphalt and 0.35 for concrete). The total diffuse irradiation on a given surface will be the sum of E_d and E_r. However, the diffuse irradiation is only applied to the unshaded areas in FLUENT. Thus, in order to correct for this error, we account for internally scattered and diffusive loading from the reflected component of direct solar irradiation. As mentioned in section 3.2, the total reflected solar irradiation is distributed among all surfaces weighted by area.

Bibliography

[1] Stephen B Pope. *Turbulent flows*. Cambridge University Press, 2000.

[2] Ansys Fluent. 12.0 theory guide. *Ansys Inc*, 5, 2009.

[3] Mikhail L Shur, Philippe R Spalart, Mikhail Kh Strelets, and Andrey K Travin. A hybrid RANS-LES approach with delayed-des and wall-modelled LES capabilities. *International Journal of Heat and Fluid Flow*, 29(6):1638–1649, 2008.

[4] Joseph Smagorinsky. General circulation experiments with the primitive equations: I. the basic experiment*. *Monthly Weather Review*, 91(3):99–164, 1963.

[5] Ugo Piomelli, Joel H Freziger, and Parviz Moin. Model consistency in large eddy simulation of turbulent channel flows. *Physics of Fluids*, 31(7):1884, 1988.

[6] PR Spalart, WH Jou, M Strelets, and SR Allmaras. Comments on the feasibility of LES for wings, and on a hybrid RANS/LES approach. *Advances in DNS/LES*, 1:4–8, 1997.

[7] Phillipe R Spalart and Steven R Allmaras. A one-equation turbulence model for aerodynamic flows. 1992.

[8] M Shur, PR Spalart, M Strelets, and A Travin. Detached-eddy simulation of an airfoil at high angle of attack. *Engineering Turbulence Modelling and Experiments*, 4:669–678, 1999.

[9] Philippe R Spalart, S Deck, ML Shur, KD Squires, M Kh Strelets, and A Travin. A new version of detached-eddy simulation, resistant to ambiguous grid densities. *Theoretical and Computational Fluid Dynamics*, 20(3):181–195, 2006.

[10] Tsan-Hsing Shih, William W Liou, Aamir Shabbir, Zhigang Yang, and Jiang Zhu. A new k-*epsilon* eddy viscosity model for high reynolds number turbulent flows. *Computers and Fluids*, 24(3):227–238, 1995.

[11] ANSYS Fluent. 12.0 theory guide. *Ansys Inc*, 5, 2009.

[12] Brian Edward Launder and DB Spalding. The numerical computation of turbulent

flows. *Computer methods in applied mechanics and engineering*, 3(2):269–289, 1974.

[13] Tuncer Cebeci and Peter Bradshaw. Momentum transfer in boundary layers. *Washington, DC, Hemisphere Publishing Corp.; New York, McGraw-Hill Book Co., 1977. 407 p.*, 1, 1977.

[14] Chandra Laksham Vaidyaratna Jayatilleke. *The influence of Prandtl number and surface roughness on the resistance of the laminar sub-layer to momentum and heat transfer*. PhD thesis, University of London, 1966.

[15] ASHRAE Handbook. Fundamentals. *American Society of Heating, Refrigerating and Air Conditioning Engineers, Atlanta*, 111, 2001.